DEVELOPING AND IMPLEMENTING A L-OPENSPIM PLATFORM USING IN-AIR OPTICS AND MEASUREMENT OF TISSUE TEMPERATURE CHANGES.

Gideon Oluniran

Student ID: 17239021

Submitted for the degree of a Research Masters

Supervised by: Dr. Niall Colgan and Prof. Peter Dockery

School of Physics

College of Science and Engineering

University of Galway

June, 2023

Table of Contents

Declaration of ownership

I, Gideon Oluniran, hereby declare this thesis is entirely my own work, and that it has not been previously submitted in whole or part for a degree. Except where referenced or acknowledged, the work presented is solely my own.

Abstract

Relative to other microscopy techniques, light sheet fluorescence microscopy is widely accepted due to its ability to provide optical sectioning, higher speed, larger field of view, lesser photobleaching, and physiological support for timelapse imaging. However, biologists interested in harnessing these benefits may not have access to commercial systems possibly due to limited funding. In cases where they do, the rapid development in research will ultimately render such platforms obsolete. Resulting in the need to consistently purchase new microscopes or upgrade modules off the shelf. At best, biologists will be forced to limit investigations to microscope capabilities. Do-it-yourself (DIY) versions exist and when combined with air objectives give greater flexibility. Biologists are therefore encouraged to learn the art of building their own microscope, starting off with platforms built off air optics, while gaining the skill required to consistently make changes when the need arises.

openSPIM DIY versions arguably have the most detailed and published build instructions, but they are more tailored towards in-vivo imaging and samples that fit within the field of view. I further expand on this by documenting stepwise instructions and building a L-openSPIM platform using air objectives for in-vivo and in-vitro imaging. More practical insights into finer light sheet alignment, choice of image acquisition software, and efficient data acquisition and saving tips are documented. I show the ability of our SPIM platform to produce quality 3D images of a millimetre sized *Varroa destructor*, and to distinctly reveal cells of the optically transparent head of a *Hydractinia symbiolongicarpus*. Details needed to extend the microscope capacity to centimetre sized samples at a high isotropic raw image resolution are stated. This work primarily aims to aid biologists with limited technical experience, and I further describe a protocol for investigating thresholds on light sheet microscopes that limit laser induced heating effects and ensure tissue bio-fidelity. I show that

10 mW, 20 mW, 30 mW, 40 mW, 50 mW, and 60 mW of laser power corresponding to intensity values of 1182 mW/mm^2, 2363 mW/mm^2, 3545 mW/mm^2, 4726 mW/mm^2, 5908 mW/mm^2, and 7090 mW/mm2 should not be applied for more than 26 s, 10 s, 5 s, 4 s, 4 s, and 3 s to 1 mm^2 of mammal tissue, respectively, to limit temperature rise to ~ $\leq 1^0$C.

Acknowledgement

My time as a student has been a very interesting and eventful one. I met a good number of extraordinary people who were very helpful in completing this work. Foremost, I would like to thank my supervisor Niall Colgan who whilst providing professional guidance showed much concern about my well-being and was always willing to help in every way he could. The door of his office was always open to me, and I do appreciate his patience and belief in me and my work.

My special appreciation to Emmanuel Reynaud and Luis Gutierrez Heredia for being go-to persons, and for giving me the opportunity to tap into their wealth of experience in openSPIM design and sample preparation.

I thank my colleagues who were at some point in the Advanced Biomedical Imaging Lab, James Blackwell, and Marcin Krasny. Your advice and direct contribution always helped me to forge ahead whenever I got stuck.

I appreciate Frank Uri and Miguel Salinas-Saavedra for providing samples for this work.
I would like to thank our technicians in the school of physics, particularly Stuart Harris, Derek Coburn, and Oliver Ryan who helped in forging items needed for my work and gave very useful advice where needed. I am also very grateful to my Graduate research Committee (GRC) members Dr. Alexander Goncharov, Dr. Nicholas Devaney, and Dr. Matthew Redman whose constructive criticism helped to fine-tune my work and gave it a better presentation. Finally, I thank Peter Dockery, the entire members of the Center for Research in Medical Devices (CURAM), and the College of Science and Engineering in the University of Galway for providing funding for this work.

List of Figures

List of Tables

Glossary of Terms

NA	-	Numerical Aperture
3D	-	Three Dimension
LM	-	Localisation (Single-Molecule) Microscopy (LM)
SIM	-	Structured Illumination Microscopy (SIM)
STED	-	Stimulated Emission Depletion Microscopy (STED)
gated CW STED	-	Time gated continuous wave STED
PALM	-	Photo-Activated Localization Microscopy
STORM	-	Stochastic Optical Localization Microscopy
dSTORM	-	direct STORM
fPALM	-	Fluorescence PALM
LSFM	-	Light Sheet Fluorescence Microscopy (LSFM)
OPFOS	-	Orthogonal Plane Fluorescence Optical Sectioning
SPIM	-	Selective Plane Illumination Microscopy
AFM	-	Atomic Force Microscopy
HILO	-	Highly Inclined and Laminated Optical sheet
OCPI	-	Objective-Coupled Planar Illumination Microscopy
miniSPIM	-	Miniaturised SPIM
TIRF	-	Total Internally Reflected Fluorescence
OPM	-	Oblique Plane Microscopy
GRIN	-	Gradient Index Lens
SPIM-FCS	-	Fluorescence Correlation Spectroscopy SPIM (SPIM-FCS)
IML-SPIM	-	Individual Molecule Localisation SPIM
DSLM	-	Digitally Scanned Light Sheet Microscopy

SI	-	Structured Illumination
SNR	-	Signal to Noise Ratio
IsoView	-	Isotropic Multiview
SIMView	-	Simultaneous Multiview
diSPIM	-	dual view SPIM
DIY-SPIM	-	do it yourself SPIM
OpenSPIN	-	Open Selective Plane Illumination Nanoscopy
SLM	-	Spatial Light Modulator
FWHM	-	Full Width Half Maximum
R.I	-	Refractive Index
RIM	-	Refractive Index Matching
RIMs	-	Refractive Index Matching Solution
R.L	-	Richardson Lucy
PSF	-	Point Spread Function
GPU	-	Graphics Processing Unit
BFP	-	Back Focal Plane
ICP	-	Iterative Closest Point
PPM	-	Parts Per Million

CHAPTER 1 Introduction

For over four centuries, microscopy has been used to study biological processes and structures that are not visible to the human eye. Optical microscopy in particular involves illuminating a sample with light within the visible range and making image observations based on established contrast mechanisms such as dark field microscopy (light scattering from the sample), bright field microscopy (light absorption in the sample), phase contrast microscopy (interference of light path lengths of varying magnitudes in the sample), differential interference contrast microscopy (interference of light path lengths of varying gradients in the sample), or fluorescence (emission of light of greater wavelength from excited fluorophores of interest in the sample). Scientists in the life sciences require understanding of sub-cellular to whole organism processes and structures, while preserving sample integrity as much as possible. To this end, protein molecules within tissues of interest are often labelled to create fluorophores that can be imaged for such studies.

Visualising biological processes using fluorophores require microscopes, each bundling a unique imaging technique, having its own merits and demerits. A more recent and widely accepted platform is the light sheet fluorescence microscope with a wide range of existing commercial and DIY platforms. Commercial platforms do provide ease of use but cannot be easily re-engineered to always keep up with the never-ending research needs. Basic DIY versions are cost-effective and can still produce quality images that are comparable to commercial platforms. Upgraded (advanced) DIY versions that outperform commercial platforms exist, though could be more expensive. Nonetheless, the benefits are huge. As such, it is often advised that scientists should learn how to build DIY platforms, starting with basic designs that can always be optimised. There are published instructions on building a DIY, but they do not describe finer light sheet alignment in different imaging buffers, which is critical for imaging cleared samples. They are also more tailored towards in-vivo imaging of small (< 1 mm) samples. This poses a huge challenge for scientists new to the technique and often may result in channelling limited financial resources to purchase modules that are not optimised for the interest of the researcher. Lack of easy access to persons with technical know-how may also lead to sub-optimal use and the eventual desertion of DIY light sheet fluorescence microscopes due to operational and maintenance challenges.

In my research, I address these challenges. I start of by describing the principle behind excitation and emission of fluorophores. I then proceed to highlight main fluorescent microscopy techniques, following which I do a comprehensive summary of the evolution of light sheet fluorescence microscopy platforms. I further describe illumination, detection, image resolution, and sample mounting frameworks of a light sheet platform with bias to openSPIM DIY model. Finally, I provide more in-depth practical notes on building a basic L-openSPIM DIY platform using air optics. The platform can be applied to a range of sample sizes in-vivo and in-vitro. It also provides a head start for ‘green horned’ scientists looking to gain requisite experience for advancing into more complex platforms. I show the ability of the platform to produce quality images and provide details to extend the microscope capacity to centimetre sized samples at a high isotropic raw image resolution.

I further describe a protocol for examining laser induced heat which is currently being ignored in light sheet microscopy procedures and suggest threshold values for the platform I built. This will ensure tissue bio-fidelity. The protocol can also be applied to other light sheet platforms for similar investigations.

1.0 Fluorescence Microscopy

Fluorescing molecules (fluorophores) are compounds that emit light following excitation. Molecules possess different electronic states depending on the total electron energy and symmetry of the different electron spin states. The electron states comprise of vibrational and rotational energy levels which are associated with bonding orbitals and atomic nuclei. Most molecules at room temperature occupy the lowest vibrational level in the ground state, as they do not have enough energy to exist in higher states. When bombarded with photons of certain wavelength (250nm to 700nm), there is an absorption of photon energies by the vibrational and rotational levels that are closely spaced. Such molecules are elevated to higher (excited) energy states and occupy different vibrational levels in the different excited states.

Following excitation, several processes occur with internal conversion and vibrational relaxation being the most probable i.e., within each excited state, molecules experience collisions, loose vibrational energy, and transit to the lowest vibrational level. Further transitions from the lowest vibrational levels of a higher energy state to the highest vibrational level of a lower energy state could occur if the vibrational levels are of the same energy. Transition to lower levels continue until the lowest vibrational level of the first excited state is reached. From there molecules drop to several vibrational levels of the ground state and emit photons of different energies (or wavelengths), forming a spectrum. As energy is assumed quantised, the quantum efficiency i.e., the ratio of the number of photons emitted by the molecule to that absorbed should be unity, ideally (Lichtman and Conchello, 2005). However, not every absorbed photon leads to an emitted photon (i.e., the excited molecules also dissipate their energies by other forms of non-radiative processes such as heat or internal conversion), the quantum efficiency (quantum yield) is usually lesser than one (1).

The excitation and emission wavelengths for a fluorophore are usually chosen to be the values at which maximum absorption and emission takes place, respectively, with the difference referred to as Stokes' shift. Stoke's shift is a representation of the energy shift from absorbed to emitted photons also caused by the loss of energy during relaxation processes that take place after absorption.

The intensity is a count of the number of photons per unit of time. The emission spectrum of a fluorophore describes the intensity spread of the photons emitted from it over their different wavelengths of emission. The absorption spectrum describes intensities at which exciting photons are absorbed relative to the wavelengths of emission. The excitation spectrum describes the different maximum intensities of emitted photons at different excitation wavelengths. The fraction of excitation photons absorbed (forming the absorption spectrum) is independent of the intensity of the incident beam but on the wavelength of excitation (Lakowicz, 2006).

As the spacing between the vibrational energy levels for the ground and excited states are similar, the same transitions between the states are more probable and thus the emission spectrum mirrors the absorption spectrum (Valeur and Berberan-Santos, 2012). There is usually a maximum number of absorption and emission cycles beyond which fluorophores experience photobleaching i.e., an irreversible alteration (destruction) of their molecular structure such that they no longer fluoresce (emit light). Following transitions from excited singlet state to the excited triplet state, photobleaching occurs when there is an interaction between fluorophores in an excited triplet state that cause an irreversible modification of their molecular bonds (figure 1.0). Phototoxicity on the other hand are usually caused by the accompanying production of free radicals and reactive oxygen that can damage living samples (Lichtman and Conchello, 2005).

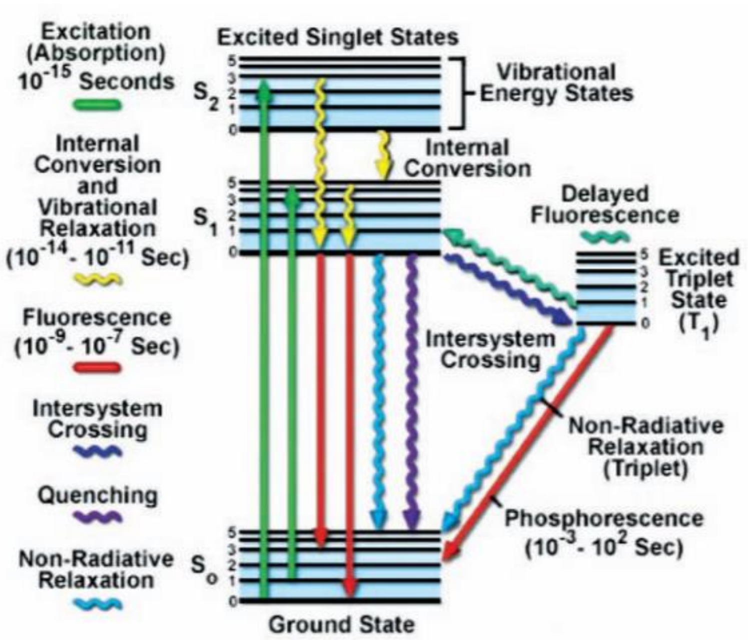

Figure 1.0: Jablonski energy diagram. As shown in Figure 1 (Davidson, 2009). Adapted from Davidson (2009), 'Fluorescence Spectroscopy' Labmedicine, 40(11), p. 1, with permission from Oxford University Press.

Figure 1.0 is a schematic of three events to the fluorescence process, and they occur at different timescales. First, the excitation of a fluorophore molecule at a specific wavelength, followed by the vibrational relaxation of electrons in the excited state to the lowest energy level (S1), and finally the emission of fluorescence photons of longer wavelengths including the molecule returning to ground state (S0). These three occurring at 10E-15, 10E-12, and 10E-9 seconds, respectively. Importantly, the difference in the timing of these events, high specificity, and high resolution provide the basis for biological and genetic studies in microscopy. The thin and thick lines represent the vibrational energy states and the electronic energy levels, respectively. Transitions resulting in absorption or emission are represented with straight arrows, while others with internal conversion and non-radiative relaxation processes are represented with curly arrows.

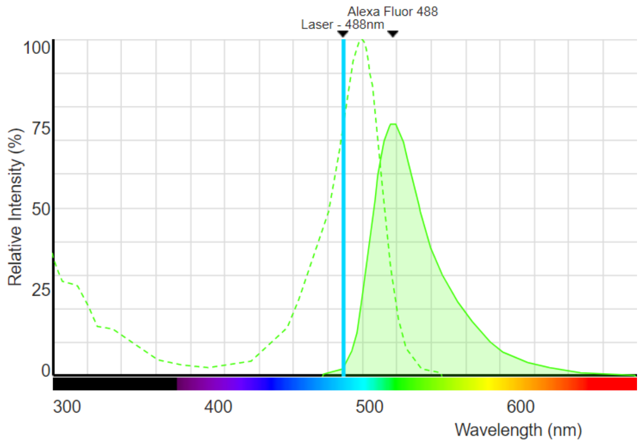

Figure 1.1. Fluorescence SpectraViewer. As shown on the viewer (ThermoFisher Scientific, 2018), In this figure, Alexa Fluor 488 emission spectra (continuous line) and excitation spectra (dotted lines) when excited with a 488 nm laser (vertical line). The excitation and emission wavelength overlap can be resolved with the use of appropriate filters to block off excitation light. Choice of fluorophore and Laser excitation wavelength should be such that the overlap between both spectra in the diagram above is as minimal as possible. i.e., fluorophores with wider stoke shifts are preferred. Used by permission of Thermo Fisher Scientific, the copyright owner.

Using fluorescence imaging systems of specific wavelengths, the temporal and spatial distributive properties of photons emitted from excited fluorophores can be observed. Many fluorescence imaging techniques have been developed, the performance of which is dependent on the efficiency in exciting only fluorophores of interest, cause minimal sample damage, efficiently capture salient sub-cellular processes, and reconstruct a high-resolution 3D image.

1.1 Epifluorescence and Confocal Microscopy

Conventional epifluorescence widefield being one of the earliest methods requires exposing the entire specimen to high intensity light and detecting fluorescence only from regions in focus. Excitation and detection are done through the same objective lens (light path) but split with the aid of a dichroic mirror. However, out-of-focus light from other areas in the specimen could contaminate signals of interest and limit resolution, thus making the technique unsuitable for sharp volumetric (three dimensional- 3D) imaging of thick samples.

Confocal Laser Scanning Microscopy (CLSM) was developed to mitigate this problem. Light emitted from a plane in focus is detected point by point through a pin hole; thereby limiting the detection of unwanted signals. The pin hole is arranged before the detector on a plane conjugate to the plane of focus. Adjusting the diameter of the pin hole helps to focus on different planes of interest in the sample, and a scanning mirror sweeping the excitation light over a plane in focus aids the detection of different points that make up the image in the plane. A good 3D spatial resolution can be obtained (especially laterally) with such a setup. However, the implementation of 'point scanning' limits acquisition speed and thus unsuitable for studying fast sub-cellular events. The technique has low optical penetration depth especially in highly scattering samples and successive excitation of the entire specimen each time a section is acquired causes excessive photobleaching. Axial resolution is also limited (since an objective of limited numerical aperture (NA) is used) and leads to an anisotropic Point Spread Function (PSF) (Greger, Swoger and Stelzer, 2007; Follain *et al.*, 2017). Spinning Disk Confocal Microscopy (SDCM) increased speed by scanning several points simultaneously with different pin holes. Again, there could be interference between signals detected if pin holes are not sufficiently apart and optical depth is still limited to less than 100 µm of thickness (Follain *et al.*, 2017).

Fluorophore excitation could be linear (one (1)-photon) i.e., each single photon carrying sufficient energy excites an electron and causes emission of another single photon of lesser energy (longer wavelength) than the excitation photon. Non-linear excitation (two (2) photon or multiphoton) also exists. For 2-photon, each of the two photons carry about half the energy required to cause 1-photon excitation and almost simultaneously impinge on an electron, causing emission of a single photon with energy slightly less than the sum of the energies of the two exciting photons. 2-photon excitation is usually done using infrared light to allow deeper penetration and less scattering. Further improvements moved beyond confocal microscopes and linear (one photon) excitation. High tissue penetration advantage of infrared rays and the use of low energy non-linear (two photon) excitation techniques have been exploited (Theer, Hasan and Denk, 2003; Helmchen and Denk, 2005a; Kobat, Horton and Xu, 2011). Greater penetration depths compared to confocal microscopy were recorded but still introduces adverse photobleaching and lesser speed, spatial resolution, and optical depth.

1.2 Super Resolution Microscopy

Light is usually diffracted as it propagates through barriers such as slits and lenses. The resolution of a fluorescence microscope is dependent on the NA of its detection lens and the wavelength of emitted fluorescence which is usually in the range of visible light. Consequently, resolution that can be achieved, is limited (equation 1.0). Super Resolution Microscopy or Nanoscopy was developed to resolve image details beyond the diffraction limit. Compared to other imaging techniques, it can spatially resolve to the order of a few ten nanometres (about 20nm) which is more suited to the size of cellular elements like proteins.

$$d = \frac{\lambda}{2n\ sin\theta} = \frac{\lambda}{2NA} \quad 1.0$$

λ = Vacuum wavelength of emission

Ɵ = Maximum subtended angle between the light ray and the optical axis of the lens

n = Refractive index of the media through which light rays travel into the lens

NA = Numerical Aperture of the lens

1.2.0 Structured Illumination Microscopy (SIM)

Structured Illumination microscopy is by far the simplest super resolution technique and is based on conventional wide field microscopy. Resolving power is up to 110 nm and 250 nm for lateral and axial resolutions respectively and is particularly suited for imaging structures with such sizes. It involves placing a diffraction grating in the illumination path and then rotating the grating to predefined orientations while acquiring an image of the sample at each angle. At each orientation, a 'frequency mixing' occurs. I.e., the grating produces a periodic pattern which interferes with the structure of the sample to create an interference (Moiré) pattern or fringes. The Moiré patterns contains sub-diffracted high frequency spatial details which can be computationally reconstructed into a single super-resolved image (Schermelleh *et al.*, 2008). Temporal resolution of SIM can be limited as 9 - 15 patterns must be acquired. Potentially, this possess more photodamage. Non-linear properties of fluorescent proteins can be exploited to limit photo exposure (Rego *et al.*, 2012). Isotropic resolution can be further improved to about 50nm with multifocal illumination pattern (York *et al.*, 2012), or three coherent beam illumination patterns (Gustafsson *et al.*, 2008), by engineering the diffraction grating.

One major challenge in SIM is its susceptibility to artefacts from photobleaching and poor refractive index matching of the sample to the immersion media. These can make algorithmic reconstruction difficult (Schaefer, Schuster and Schaffer, 2004).

1.2.1 Stimulated Emission Depletion Microscopy (STED)

Stimulated Emission Depletion (STED) microscopy is a technique with better lateral resolution than SIM and the final image is less prone to artefacts from mathematical reconstruction. It works based on the scanning principle of the confocal microscope with one objective and two pulsed lasers. Basically, the area of specimen in focus is illuminated by both lasers in a synchronised train of pulses. The pulse from one laser excites the sample and is quickly followed by a stimulating depletion pulse that has been shifted to the red-light spectrum (forming a pair of perpendicularly polarised beams – doughnut shaped STED pulse). The STED pulse sent through the sample ensures that all excited molecules not within its 'center' are depleted before they emit fluorescence light (i.e., returned to ground state, emit at depletion wavelength, and are intrinsically filtered from detection). Thus, only fluorescence light from within the 'center' are detected confocally (Klar *et al.*, 2000; Willig *et al.*, 2007). This is repeated until the entire sample is imaged, and thus, an inherent limitation in temporal resolution could lose information on fast nuclear processes.

Time gated continuous wave STED (gated CW STED) may be less phototoxic (since low power lasers are used), have been shown to be suitable for live imaging of small transparent samples, and improve acquisition speed to about 100 frames per second (Willig *et al.*, 2007; Westphal *et al.*, 2008; Vicidomini *et al.*, 2011; Schneider *et al.*, 2015). However, for relatively larger samples, spatial resolution could be lower. Literature suggests combining STED with techniques known for high optical penetration depth capabilities such as two-photon excitation (Denk, Strickler and Webb, 1990; Helmchen and Denk, 2005b). This introduces more photobleaching, though it can have a greater imaging depth of up to 1mm. The major limitation of STED is the in-homogeneity of tissues which causes a dis-alignment between the excitation and STED pulses.

1.2.2 Localisation (Single-Molecule) Microscopy (LM)

Other super resolution microscopy techniques and their variants such as Photo-Activated Localization Microscopy (PALM) (Betzig *et al.*, 2006; Hess, Girirajan and Mason, 2006b), Stochastic Optical Localization Microscopy (STORM), direct STORM (dSTORM) (Heilemann *et al.*, 2005, 2008; Rust, Bates and Zhuang, 2006), and Fluorescence PALM (fPALM) (Hess, Girirajan and Mason, 2006a) are hinged on similar single-molecule localisation principle as they can resolve fluorophores to single molecule level. By exciting a small fraction of all fluorophores in a single timepoint, if the fluorophore of interest emits enough photons in the excited fraction and is sufficiently distinct from the background signal, a single fluorophore can be localised. The spatial position of the localised fluorophore can be accurately estimated by fitting its PSF in a statistic several orders smaller than the PSF itself to obtain a sub-diffraction resolution. To acquire for all regions of interest in the sample, the process is repeated for multiple timepoints (which could be of the order of thousands) separated temporally. Thus, resolutions of 20 nm to 10 nm can be achieved (Betzig *et al.*, 2006; Hess, Girirajan and Mason, 2006a). The different protocols for localising fluorophores are what distinguishes different LM techniques. PALM involves photo manipulation of fluorescent protein, STORM; a resonant energy transfer from one organic dye to the other, and dSTORM; photo-switching an organic dye between its fluorescing and non-fluorescing states. Generally, in LM techniques, the need to acquire several timepoints lowers temporal resolution and could increases photodamage.

1.3 Light Sheet Fluorescence Microscopy (LSFM)

Widefield, confocal, and super resolution microscopy in the basic sense involve exposing the entire specimen to an excitation light which in turn leads to sample degradation over time. Depending on the technique used there may also be blurs from regions out of focus. Temporal resolution may be limited due to point scanning or the inability to detect emitted fluorescence simultaneously. Scattering of excitation beams in SIM and STED can lead to the production of aberrated images. Light Sheet Fluorescence Microscopy (LSFM) largely overcome these limitations through optical sectioning.

Generally, optical sectioning in fluorescence microscopy is achieved in three ways. One method is by the deconvolution of the raw 3D data acquired. In each acquired slice, information from ‘data in focus’ are extracted and those out of focus are suppressed before reconstructing the 3D image. The process can however be computationally intensive, does not allow for real time observation of acquired images, and less than ideal assumptions are often made on the properties of the sample and microscope. Optical sectioning is also achieved on the detection as in the laser scanning confocal microscope. Point scanning eliminate out-of-focus light and the adjustable pin hole determines the thickness of the plane being imaged. The downside to this is the corruption of detected signals in highly scattering tissues, in addition to the known limitations of confocal microscopy. A third approach to optical sectioning is to re-engineer the illumination beam. Non-linear multiphoton illumination uses a tightly focused infrared beam to excite only the volume within the laser focus. Though penetration depth is high, the use of pulsed lasers is damaging to samples especially for in-vivo studies. On the other hand, LSFM provide intrinsic optical sectioning by using a light sheet to illuminate a thin axial volume such that only fluorophores within the optical section are excited and simultaneously detected. As the illumination axis is arranged orthogonal to the detection and only the plane of interest is excited in LSFM, scattering is mitigated in-situ and a high signal to noise ratio is achieved. In comparison to existing fluorescence imaging techniques, LSFM has the best speed, axial resolution, optical penetration depth, and least photobleaching effect (Huisken and Didier Y R Stainier, 2009).

Siedentopf and Zsigmondy, (1902) were the first to adopt the use of a light sheet in a microscope. Using a light sheet made of sunlight, they could focus on a few gold particles in an ensemble and could visualise single particles. In application to fluorescence microscopy, Voie, Burns and Spelman, (1993) reported the first use of a light sheet to image biological samples. The setup called Orthogonal Plane Fluorescence Optical Sectioning (OPFOS) involved sample staining, the use of illumination optics, a laser for excitation, a camera and air objectives for fluorescence detection, a sample chamber, and a module to move the sample to acquire image stacks. They could image the inner architecture of a 'cleared' cochlea of a guinea pig with lateral and axial resolutions of 10 µm and 26 µm respectively. Indeed, this setup formed the prototype for modern light sheet systems used in biological imaging, including a modified version with higher resolution (HR-OPFOS) (Buytaert and Dirckx, 2007).

Beyond OPFOS, several other implementations of fluorescence light sheet microscopy for biological imaging have been largely driven by the quest to overcome certain limitations. One obvious challenge is sample mounting. Another is the size and opacity of biological samples more so when imaging deep into tissue. Resolution can be sub-optimal due to light scattering, sample motion, or the motion of the region of interest within the sample (such as eyes, heart etc.). That not neglecting the need to image beyond the diffraction limit (Rayleigh criterion).

There is also the need to meet physiological needs and capture transient biological dynamics for in-vivo studies.

On sample mounting, commercially available high numerical aperture (NA) objectives that support high resolution can be challenging to fit into the traditional orthogonal setup of LSFM. This is due to their limited working distance and cumbersome design. Additionally, standard biological sample mounting methods such as the use of coverslips, glass slide, and petri dishes are not feasible. Consequently, there have been modifications. Reflected Light-Sheet Microscopy (RLSM) involves the use of two high NA objectives placed almost diametrically opposite each other. One of these objectives projects a slender light sheet, which is then reflected off an AFM cantilever and directed towards the imaging plane of the second (detection) objective, situated near the sample's surface (Gebhardt *et al.*, 2013). In Light-Sheet Bayesian Microscopy (LSBM), a prism is positioned following the illumination objective to deviate the light sheet horizontally onto the sample, aligning it precisely with the imaging plane of the detection system (Hu *et al.*, 2013).

V-shaped objective configurations are notably well-suited for standard sample mounting procedures (Hu *et al.*, 2013). In Inverted Selective Plane Illumination Microscopy (iSPIM) or its dual-view counterpart, the sample is suitable for single-cell imaging or any specimens that necessitate mounting on a conventional glass coverslip (Wu *et al.*, 2011, 2013). In dual-view SPIM (diSPIM), two similar objectives are arranged in a V-shaped configuration above the sample. This arrangement positions the orthogonal excitation and detection arms at a 45° angle to the horizontal, enabling imaging from both above and below the intact sample. Excitation and imaging alternate between these two objectives, resulting in isotropic resolution with equal lateral and axial resolution. A similar approach is employed in tripleview microscopy (Wu *et al.*, 2016). Open-Top Light-Sheet (OTLS) microscopy resembles iSPIM but has an inverted orientation. However, a limitation of this setup is the aberrations introduced due to the 45° orientation of the cover glass in relation to the illumination and detection path (Glaser *et al.*, 2017, 2019; Chen *et al.*, 2019). This issue has been addressed by utilizing a water prism to correct these aberrations (McGorty *et al.*, 2015).

Single objective options were also developed. Objective-type Total Internally Reflected Fluorescence Microscopy, often referred to as prismless TIRFM, involves a setup where the incident laser beam is precisely focused on the back focal plane of the objective lens. It is then directed to propagate along the edge of the objective, causing total internal reflection to occur. This results in the creation of an evanescent field located just above the glass surface upon which the sample is mounted. This configuration is particularly well-suited for visualizing single molecules (Tokunaga *et al.*, 1997). The TIRF illumination technique exclusively targets the surface region of a sample, and when combined with super resolution technique can be used to study single molecules located on the cell surface. Highly Inclined and Laminated Optical sheet (HILO) improved on the imaging depth and signal to noise ratio of single molecule TIRF by using a thin TIRF objective-inclined beam at an angle below that of total refraction to illuminate a confined volume of samples that are mounted on cover slips (Tokunaga, Imamoto and Sakata-Sogawa, 2008). In eliminating the limitations of 'defocusing' in HILO; caused by the non-parallel alignment of the image plane to the plane of excitation, Oblique Plane Microscopy (OPM) introduced extra lenses and objectives to tilt the image plane (Kumar et al., 2011). An alternative approach to addressing the challenges associated with oblique plane imaging is to reorient the light sheet into a horizontal plane that is perpendicular to the detection arm. In the case of single-objective cantilever selective plane illumination microscopy (socSPIM), this is achieved by rotating the light sheet 90° using an

AFM tip (Ponjavic *et al.*, 2018). Alternatively, a micromirror can be employed for this purpose (Galland *et al.*, 2015; Zagato *et al.*, 2017). Another technique, known as Single Vertically Illuminated Plane in a PRISM method, solves this issue by rotating the image plane using a mirror instead (Beicker *et al.*, 2018).

Objective Coupled Planar Illumination (OCPI) microscopy entails the rigid integration of light sheet generation optics with a high numerical aperture (NA) detection objective lens (Holekamp, Turaga and Holy, 2008). This integration allows for the simultaneous movement of both the lens and optics along the axis of the objective, enabling the acquisition of volumetric images to study cellular function within living neural tissue, even in the presence of scattering. OCPI is particularly suited for imaging fast neuronal activity of about 20 Hz at 200 image planes per second without the need for sample movement that can limit acquisition speed. miniSPIM uses a single mode optical fibre, a Gradient Index Lens (GRIN) and a right-angle microprism to produce a thin light sheet in a miniaturised system. The setup could resolve to 3.2 µm and image approximately 125 µm deep into a mouse brain in-vivo (Engelbrecht, Voigt and Helmchen, 2010).

Another single objective platform is the Swept Confocally Aligned Planar Excitation (SCAPE) microscopy. In an innovative technique that integrates a scanning galvanometer mirror with oblique plane illumination, this setup allows for the lateral sweeping of the excitation sheet across the sample while simultaneously keeping the camera's focus on the moving plane. SCAPE microscopy offers the capability to achieve exceptionally high-speed light-sheet volumetric imaging using a single, stationary objective lens, all without the need for any movement of the sample (Bouchard *et al.*, 2015).

Single-view imaging in Light Sheet Fluorescence Microscopy (LSFM) is limited when it comes to visualizing entire large multicellular organisms. This limitation arises from factors like light absorption, scattering, and the deterioration of image quality as one goes deeper into the sample. Additionally, the absorption-related shadowing effect, often resulting in stripe artifacts, is a common issue in this context. To address these challenges, a widely adopted solution is to employ a multiview acquisition approach. In this method, the sample is systematically rotated, and 3D image volumes are acquired from multiple viewing angles. This technique proves especially valuable for imaging dense and sizable specimens, as it helps mitigate the aforementioned issues and provides a more comprehensive view of organism structure and details.

Famous platforms implementing this design include Selective Plane illumination Microscopy (SPIM) (Huisken *et al.*, 2004), Ultramicroscope (Dodt *et al.*, 2007), multidirectional SPIM (mSPIM) (Huisken and Stainier, 2007).

SPIM is useful for the in-toto imaging of large (50 µm to orders of millimetres) biological samples. It includes a sample chamber that supports physiological conditions necessary for long term in-vivo imaging of developing embryos. A static light sheet is formed from a cylindrical lens with its waist aligned to the focal plane of an immersion detection objective. The setup has been shown to image of the evasive inner heart structure of a Medaka Arnie fish developing embryo, and a 17hr development of Drosophila embryo, and can have an isotropic resolution of up to 6 µm at a tissue depth of 500 µm. Importantly, SPIM elevated the LSFM technique to the forefront of scientific attention. Here, multiview acquisition is done by acquiring a complete 3D stack for a view before repeating for a different view (since it has only one illumination arm).

The Ultramicroscope is an attempted upgrade to SPIM to reduce the number of views to be acquired while supressing stripe artefacts. It utilises dual static light sheets in opposing directions which are formed from two cylindrical lenses and are simultaneously powered. However, the scattering of each beam in simultaneous illumination of a sample by two counterpropagating beams results in widening of an overlapped light-sheet in comparison to the width of the light-sheet in single side illumination.

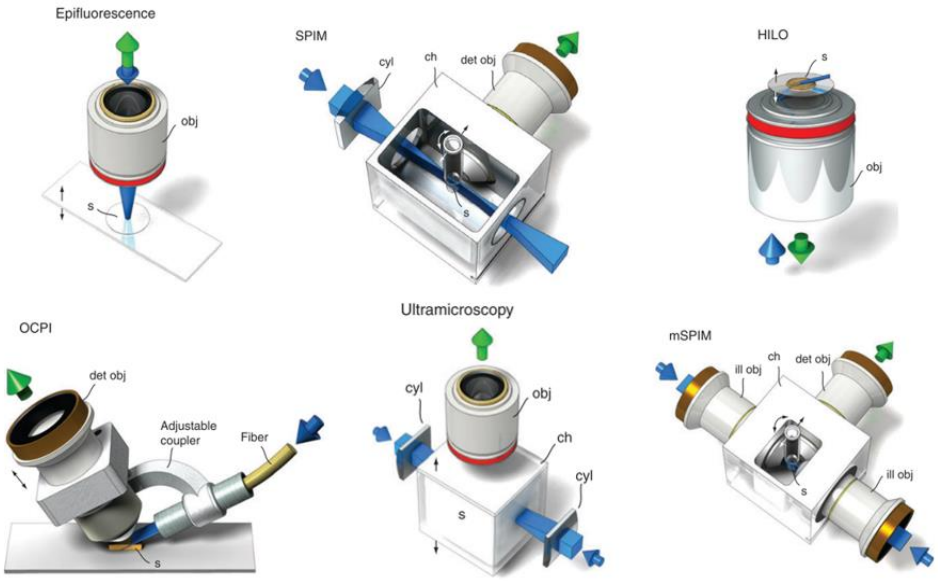

Figure 1.2: Epifluorescence setup and different early implementations of light sheet microscopy. As shown in Figure 4 (Huisken and Didier Y.R. Stainier, 2009), Blue and green arrows show the illumination and detection directions, respectively. Adapted with permission from Huisken and Didier Y.R. Stainier (2009), 'Selective plane illumination microscopy techniques in developmental biology' Development, 136(12), p. 1969. doi: 10.1242/dev.022426. 'This image is not published under the terms of the CC-BY-NC-ND (http://creativecommons.org/licenses/by-nc-nd/3.0/) license of this thesis. For permission to reuse, please see the original article.'

mSPIM bundled dual static light sheets formed from two illumination objectives and are powered consecutively (rather than simultaneously) used for excitation while pivoting the light sheets vertically along the focal plane of the detection to aid deeper imaging and minimise the effect of scattering obstacles in the illumination path. Nonetheless, the image quality of planes that are closer to the detection objective are still better than the deeper planes.

Multiview imaging, while effective for certain applications, does come with some drawbacks. One of the significant limitations is its low temporal resolution, which can be detrimental when trying to visualize and understand transient biological processes in real-time, especially in vivo settings. Additionally, the mechanical rotation of the specimen during multiview acquisition may introduce vibrations, potentially affecting image quality and stability. Moreover, using multiple views often necessitates an increased illumination dose, which can lead to greater photodamage to the biological sample. This is a critical concern, especially when imaging live or delicate specimens. Another challenge associated with multiview imaging is the computational expense of data reconstruction. Collecting data from multiple angles can result in very large datasets, often reaching terabytes in size. The subsequent processing and reconstruction of these datasets can be computationally intensive and time-consuming.

An efficient solution to address some of the limitations associated with multiview imaging is to acquire multiple image stacks from different viewing angles simultaneously and then reconstruct a comprehensive 3D image by merging these stacks. The Simultaneous Multi-View (SiMView) light-sheet fluorescence microscopy technique involves the implementation of sequentially-alternating scanned light-sheet excitation using two opposing scanned light-sheet illumination arms (Tomer et al., 2012). Two opposite detection objectives are used to collect the fluorescence light emitted from the specimen. This setup enables the acquisition of four complementary views of each plane within the specimen. These views are obtained through two sequential illuminations and two simultaneous acquisitions for each plane. Another variation of this method is Isotropic Multiview (isoView) LSFM, which follows a similar framework. In isoView LSFM, all four objective lenses are employed for both illumination and detection, resulting in four different views of the specimen (Chhetri et al., 2016). This approach further enhances the imaging quality and enables a comprehensive understanding of the sample's three-dimensional structure and features.

However, it is essential to note that implementing simultaneous multiview imaging can be technically challenging and may require specialized hardware and software solutions. It is also costly and require technical expertise for precise alignment. As such some researchers have focused on re-engineering the light sheet aimed at more efficient illumination instead. Briefly, various light sheets developed beyond using spatially coherent static light sheet are gaussian digitally scanned light sheet (DSLM) that provides more uniform illumination (Keller and Stelzer, 2008), scanned Bessel beams that are self-reconstructing and less scattered in tissue (Fahrbach and Rohrbach, 2010) and Planchon et al. (2011), Airy beam unlike Bessel beams exhibits fewer side lobes due to its asymmetric intensity distribution Vettenburg et al., (2014) and (Yang et al., 2014). As a result, the impact of side lobes on contrast reduction is minimised. These are described on greater details in section 1.3.0. Hybrid platforms combining LSFM and super resolution microscopy were also developed to image beyond the diffraction limit, and also to improve SNR of super resolution techniques (Hu *et al.*, 2014; Gustavsson, Petrov and Moerner, 2018; Gagliano *et al.*, 2021).

While all these platforms prove useful, they are not readily available and are not easy to build for scientists or biologist who are not specialists in bioptics and biomedical imaging. The volume of data generated especially for multiview systems such as diSPIM (Wu *et al.*, 2013), SiMView-SPIM (Tomer *et al.*, 2012), and IsoView LSFM (Chhetri *et al.*, 2016) could also be too massive. Commercial systems which include the Lightsheet Z.1 by Carl Zeiss, LaVision BioTec Ultramicroscope, diSPIM from Applied Scientific Instrumentation, and TCS SP8 DLS from Leica are relatively expensive, cost between $250,000 and $500,000 (Marx, 2016), and may not be easily reengineered to suit imaging needs.

These complexities, lack of easy step by step build details, and relatively high cost are reasons why open models are preferred. Open models include; DIY-SPIM (Lorenzo *et al.*, 2011; Lorenzo, 2012), OpenSPIM (Pitrone *et al.*, 2013a; Girstmair *et al.*, 2016, 2022b), and OpenSPIN (Gualda *et al.*, 2013). These systems can be 'home built' at a relatively lower cost (lesser than $50,000) and constantly reengineered to suit unending research needs. The open model for SPIM - OpenSPIM is preferred as it generates lesser amount of data than other LSFM systems which makes it easier to deal with computational load, and it has a dedicated website that gives detailed build instructions, suggests cheaper alternatives, and enjoys a community of individuals volunteering troubleshooting support. LSFM only became widely adopted in the advent of OpenSPIM. Some other do-it-yourself microscope also exist such as mesoscale SPIM (mesoSPIM) (Voigt *et al.*, 2020), Light Sheet Thetha Microscopy (LSTM) (Bianca Migliori *et al.*, 2018), Cleared-Tissue Axially Swept Light-Sheet Microscopy (ctASLM) (Chakraborty *et al.*, 2019). These are very useful for imaging very large intact sample such as the whole intact central nervous system of a mouse at cellular resolution. Though they are significantly expensive (could be as much as some commercial platforms - up to $249,000), they still have an open design framework and as such can be easily tweaked to suit research needs. However, the mesoSPIM project appears to be the only advanced platform that has a well-documented stepwise build instruction, and the authors advise interested scientist to at least have an experience in building basic platforms before attempting to develop advanced models (Vladimirov, Voigt and Campbell, 2023). I subsequently describe in greater details the framework of light sheet microscopes with bias to those that can be adopted in an OpenSPIM design.

1.3.0 Illumination Framework

Basically, a static light sheet can be formed coherently by focusing a Gaussian beam on a cylindrical lens. Here, a gaussian beam is expanded and projected through a cylindrical lens of suitable NA to generate a plane of light that is as thin as possible and should uniformly cover the entire Field of View – FOV of the detection unit. Lateral resolution of a LSFM system is dominated by the NA of the detection lens. The thickness of the light sheet dominates the axial resolution, which in turn depends on the NA of the illumination optic and the excitation wavelength. In-depth details on image resolution are described in section 1.3.3.

Using a standalone cylindrical lens and slits or apertures to generate a light sheet amplify diffraction, are not suitable for generating overlapping light sheets of different wavelengths, nor imaging in immersion media. Arranging the illumination optics differently, and introducing additional optics (lenses, a corner mirror and a corrected illumination objective) can introduce more uniformity and help to fine-tune the geometry of the light sheet (Figure 1.3 and 1.4) (Greger, Swoger and Stelzer, 2007; Shah, Weber and Huisken, 2017).

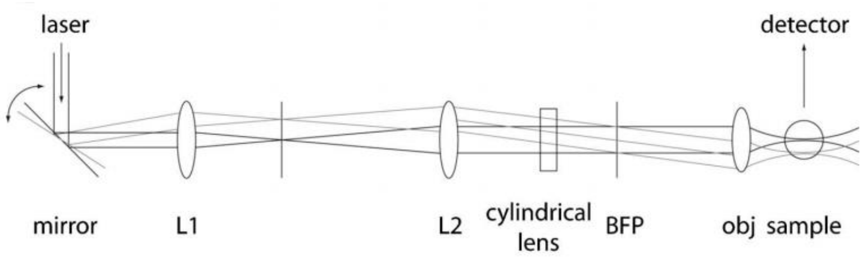

Figure 1.3. Illumination framework of a gaussian light sheet formed from a cylindrical lens (Greger, Swoger and Stelzer 2007, p. 023705-4). The first telescope which forms the light sheet is made of an objective lens and a cylindrical lens with focal planes along the detection axis and the back focal plane (BFP) of the objective, respectively. The second is a relay telescope (beam expander – L1 and L2) which expands the beam diameter to the required size. For Low NA illumination objectives, the beam could be expanded to fully illuminate its BFP. The expanded beam is projected through the cylindrical lens; placed at 90^0 so that the beam is not refracted in its dimension perpendicular to the plane of the light sheet and imaged to the back focal plane of the objective lens. This limits diffraction in the light sheet as the illumination objective is designed without the need for slits to adapt its NA. Conjugated planes are formed by the adjustable mirror and the BFP of the objective lens. By tilting the mirror about the centre of the plane, the light sheet can be moved solely in the direction of the detection axis such that it is properly aligned (superimposed) with the focal plane of the detection lens.

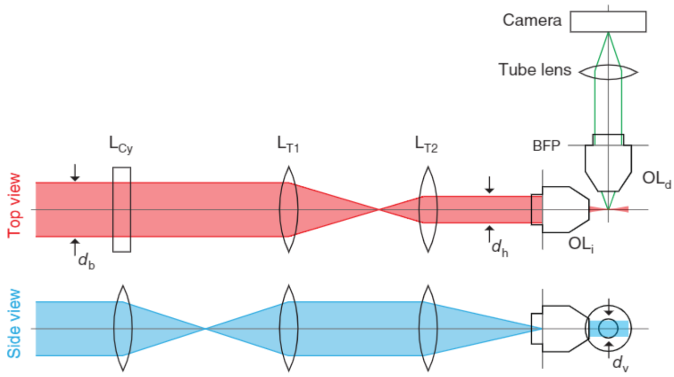

Figure 1.4: Top and side views of the illumination arm arranged differently (Shah, Weber and Huisken, 2017, p 247). L_{Cy} – Cylindrical lens, L_{T1} - Telescope lens 1, L_{T2} - Telescope lens 2, OL_i, - Illumination objective lens, OL_d – Detection objective lens. d_v – lens diameter of the detection view, d_h – height of the light sheet. The illumination arm can be further arranged differently. The laser beam can be expanded by a telescope (beam expander) and collimated onto the cylindrical lens that forms the light sheet. As the light sheet needs to be vertical at the sample, it should converge horizontally at the BFP of the illumination objective lens. This can be difficult to achieve as the BFP can be within the barrel of the objective, making it challenging to align the light sheet to it. Adopting the inter-reversible principle of light, another two-lens telescope can be used to image the BFP to a plane mirror instead, and then aligning the light sheet to it on the mirror. The beam exiting L_{Cy} is made to impinge on and reflect from the plane mirror at 45^0 (imaginarily moving L_{Cy} to the position of the light path before it is incident on the mirror in figure 3a). This is the principle adopted by the openSPIM design, where the back focal plane of the objective forms conjugates planes with the plane mirror. Thus, the corner mirror can be used to tweak the height of the light sheet over the FOV and aligning it to the focal plane of the detection.

The intensity distribution of a gaussian beam can be described with a gaussian function I (z,x) (equation 1.1) with width ω(x) that is dependent on position X, the direction of beam propagation. Z is the radial distance from the centre axis of the beam i.e., the lateral position (Yariv and Albert, 2003).

$$I(z,x) = \frac{|E(z,x)|}{2\eta} = I_\circ \left(\frac{\omega_\circ}{\omega(x)} \right)^2 \exp\left(\frac{-2z^2}{\omega(x)^2} \right) \qquad 1.1$$

E = Electric field, η = wave impedance of the medium in which the beam is propagating, $\omega_\circ$ = beam waist.

I briefly describe the theoretics to consider when illuminating with a gaussian beam, as detailed in Shah, Weber and Huisken, (2017).

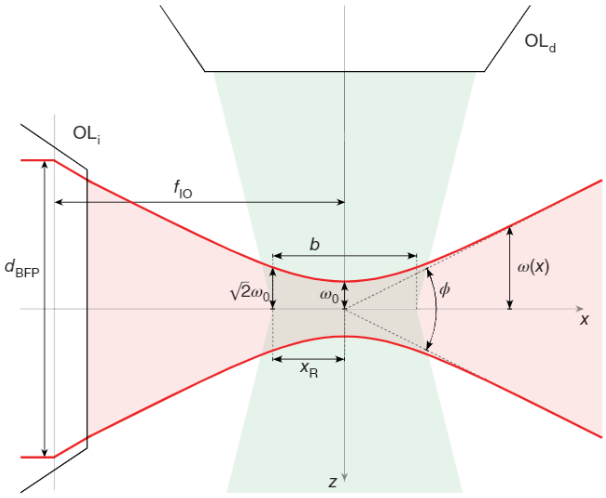

Figure 1.5: Static gaussian light sheet superimposed on the field of view of the detection (Shah, Weber and Huisken, 2017, p 249). Ideally, I want the light sheet thickness to be thinner than the depth of field of the detection unit, and the mid-plane of its waist aligned to the focal plane of the detection. $\omega_\circ$ is the beam waist. Rayleigh range (X_R) is the distance for which the beam waist expands to $\sqrt{2}\ \omega_\circ$, or for which the beam intensity drops to half of its value at $\omega_\circ$. f_{IO} and d_{BFP} are the focal length and diameter of the back focal plane of the illumination objective, respectively. OLi, - Illumination objective lens, OL_d – Detection objective lens, ϕ is the total angular spread of the beam, b – field of view along beam propagation which is equivalent to 2 X_R.

Figure 1.5 shows a Gaussian beam brought to focus in a medium with refractive index n, by the illumination lens with numerical aperture (NA):

$$NA = n\sin\left(\frac{\phi}{2}\right) = n\sin\left[\arctan\frac{d_{BFP}/2}{f_{IO}}\right] \qquad 1.2$$

d_{BFP} = diameter of the back focal plane of the illumination lens, f_{IO} = focal length of the illumination objective.

$$\left(\frac{\phi}{2}\right) = \left[\frac{d_{BFP}/2}{f_{IO}}\right] \qquad 1.3$$

The total angular spread or opening angle for the beam (in radians) ϕ , and the beam waist ω_o are defined as:

$$\phi = \frac{2\lambda}{\pi n \omega_o} \qquad 1.4$$

$$\omega_o = \sqrt{\frac{X_R \lambda}{\pi n}} \qquad 1.5$$

X_R and λ are the Rayleigh length and wavelength of the beam, respectively. The Rayleigh length is the distance for which the beam waist expands to $\sqrt{2}\,\omega_o$, or for which the beam intensity drops to half of its value at ω_o .

From 1.3, 1.4, and 1.5, the diameter of the BFP (d_{BFP}) of the illumination objective can be expressed as:

$$d_{BFP} = 2 f_{IO} \sqrt{\frac{\lambda}{\pi n X_R}} \qquad 1.6$$

The size of the FOV in the direction of beam propagation (FOV_x) should be twice the Rayleigh length X_R (i.e., $2X_R = FOV_x$). Thus, if this is known, I can infer the Rayleigh length and calculate the d_{BFP} which in essence is a measure of how wide (in diameter) the original laser beam should be expanded to ensure the full NA of the illumination objective is used in generating the light sheet at the sample.

From the top view of figure 1.4, 1.6 can be expressed as:

$$d_{BFP} = d_b \frac{f_{T2}}{f_{T1}} = d_b M_T \qquad 1.7$$

M_T defines the required magnification for the telescope made of lenses L_{T1} and L_{T2} with focal lengths f_{T1} and f_{T2}, respectively, to adapt the height of the light sheet and image the BFP of the objective lens to a plane mirror positioned between the cylindrical lens and L_{T1}. d_b is the diameter of the beam incident on the cylindrical lens.

Also, the height of the light sheet generated at the sample d_h is simply a scaling of d_b by the beam cropping factor α_y and the magnifying factor (focal length ratios) of the optic pairs lens 1 (L_{T1}) - cylindrical lens (L_{Cy}), and lens 2 (L_{T2}) - illumination objective (OL_i) i.e.

$$d_h = \alpha_y d_b \frac{f_{T1}}{f_{Cy}} \frac{f_{IO}}{f_{T2}} = \alpha_y d_b \frac{1}{M_T} \frac{f_{IO}}{f_{Cy}} \qquad 1.8$$

f_{Cy} refers to the focal length of the cylindrical lens. α_y is incorporated as slits are used to crop the beam only vertically, to nil off the tails of the gaussian profile. Doing this horizontally widens the light sheet.

As gaussian beams fan out i.e., diffract with increasing distance, a necessary trade-off between the thickness of the light sheet and its uniformity across the field of view of the detection setup becomes imperative to allow for a more even illumination of the sample. The general idea is to use a thinner light sheet for a smaller field of view. A thicker light sheet is used for a larger field of view and can be obtained using the same illumination objective by limiting how much the laser beam is expanded, which in essence underfills the NA of the illumination objective. Also, in defining the light sheet dimensions, a thickness of 5 to 10 microns is suggested for samples of about 1 – 5 mm size, and approximately 1 micron thickness for smaller samples of 20 – 100 micron (Engelbrecht and Stelzer, 2006).

Opposed to a static light sheet is the use of a scanned gaussian beam; Digitally Scanned Light Sheet Microscope (DSLM) (Keller and Stelzer, 2008). The plane of light is otherwise generated by rapidly scanning a micrometre thin gaussian beam ‘up and down’ (vertically), and then through the specimen. An f-thetha and tube lens placed in the illumination path after a scanning mirror forms the thin profile of the beam and tilting of the scanning mirror causes the vertical displacement.

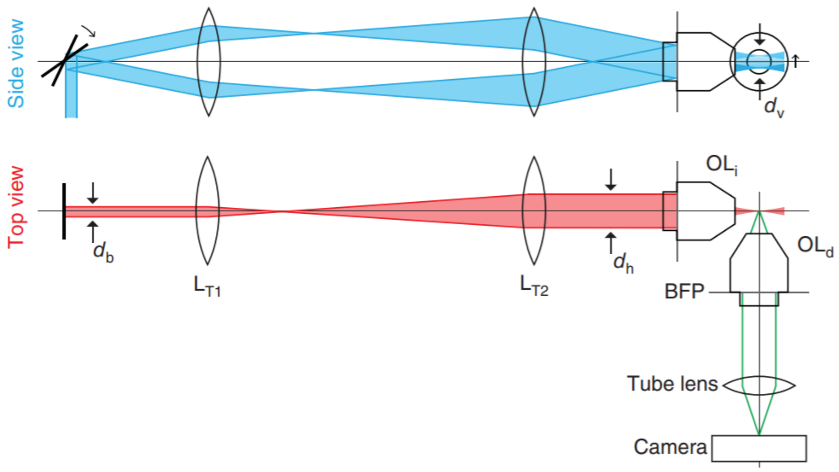

Figure 1.6: DSLM gaussian scanned beam (Keller and Stelzer, 2008 p 1065; Shah, Weber and Huisken, 2017 p 247). L_{T1} is a f-theta lens while L_{T2} is a tube lens. Scanning the beam d_b incident on the plane mirror at an amplitude defines the height of the light sheet d_h. L_{T1} - Telescope lens 1, L_{T2} - Telescope lens 2, OL_i, - Illumination objective lens, OL_d – Detection objective lens. d_v – lens diameter of the detection view, d_h – height of the light sheet

The amplitude of scanning and the beam diameter d_b determines the height of the light sheet in this case. The main merit of DSLM is that two-photon excitation may occur when using the infrared wavelength. In such a case, the light sheet profile is thinner and penetrates dense tissue deeper as they are less affected by scattering (Keller *et al.*, 2011; Huisken, 2012). A downside to scanned gaussian beam however is that one line is illuminated for a short part of the exposure time, requiring local intensity of the beam to be much higher. The sample could be exposed to light intensity approximately 300 times than the use of static light sheets to acquire the same object volume within the same timeframe and this can be tissue damaging in one-photon excitations (Keller *et al.*, 2008; Huisken, 2012). Temporal resolution may also be limited by the speed of the scanning mirror in addition to that possibly imposed by the camera speed, and images acquired may be more susceptible to artefacts caused by sample motion (Scherz *et al.*, 2008). Scanned gaussian beams also suffer from uneven thickness (Weber and Huisken, 2011).

An improvement to scanned gaussian beams is the use of scanned Bessel beams (Fahrbach and Rohrbach, 2010). Bessel beams can be formed by focusing a gaussian beam through an axicon lens or using axisymmetric diffraction gratings. They are also formed from annular apertures placed in the far field to project an annular illumination pattern at the rear pupil of an illumination objective. In contrast to gaussian approximation of light, after being focussed to a spot, they do not diffract (do not spread out) for a limited distance and are self-reconstructing (regains form after obstructions). Thus, they are less affected by scattering, achieve greater optical depth, and the transverse intensity profile changes very little over a small distance. Fahrbach and Rohrbach (2010) described a scanned Bessel beam in a LSFM setup using a circular aperture to eliminate diffraction orders, and a Spatial Light Modulator (SLM) placed within the focal length of a lens for holographic 3D beam shaping and positioning. Here, Bessel beams in homogeneous media can have about 0.6 µm thickness (FWHM) than gaussian (1.4 µm). However, in scattering media, though it still has a greater optical depth of 200 µm (100 µm for gaussian), it has poorer contrast than gaussian. This is because in practice, the circular aperture does not eliminate the zero-diffraction order. If the SLM is positioned such that the less diffracted beam lies centrally on the optical axis (which is practically difficult), the zero order can also be eliminated. This limitation creates ‘side lobes’ (rings) around the beam formed and generates background fluorescence. Visibly, this appears as additional background in the degraded image.

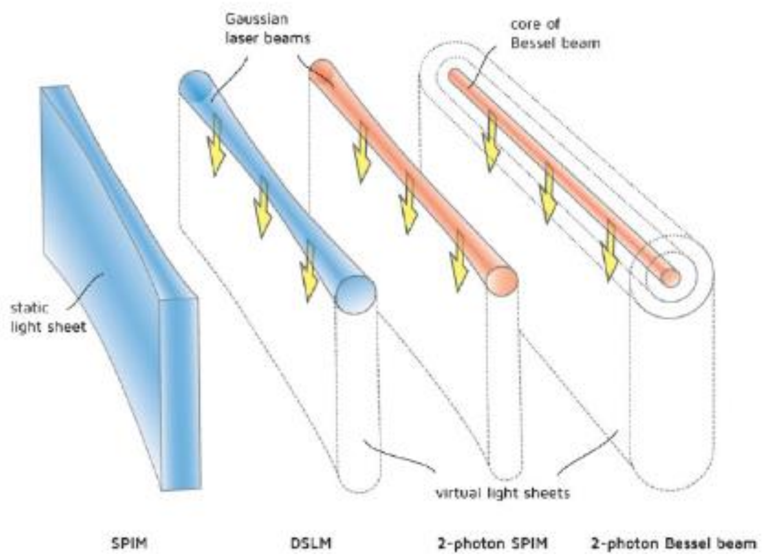

Figure 1.7: Different light sheet generation strategies. As shown in Figure 3 (Huisken, 2012). Adapted with permission from Huisken, J. (2012) 'Slicing embryos gently with laser light sheets', Bioessays, 34(5, SI), pp. 408.

Energy of a Bessel beam is mostly contained in the rings surrounding the central lobe and could be 3 to 5 times that of conventional beams (low NA lenses give lower energy). This makes the beam less desired for in-vivo imaging as it causes greater photobleaching than gaussian beams. The ring system is also critical to its long optical penetration depth capabilities. For an orthogonal detection, the presence of the 'side lobes' reduces optical sectioning advantages and contrast of a LSFM system.

Some limitations of Bessel beam excitation were addressed by Planchon *et al.* (2011). A thicker annulus (circular aperture) could help suppress the rings but will reduce the beam length. Using 2-photon excitation and pulsed lasers, they developed linear and thinner light sheets (less than 0.5 µm). In the setup, same 0.8NA objective lenses were used for illumination and detection and for isotropic resolution. In contrast to Fahrbach and Rohrbach (2010), the sample was kept static, and the use of an apodisation mask (filter) filters off the 'side lobes' efficiently with 2-photon. Particularly, to achieve over 50 % of the energy impinged on the filter is transmitted to the sample (50 – 250 mW), 2-photon with pulsed lasers are required. In-vivo imaging (single image per plane) of mitotic chromosomes and intracellular vesicles could be achieved at axial (and isotropic) resolution of 0.3 µm and speeds up to 200 planes per second (or 5-30 mS per plane). Bessel beams produce thinner light sheets and longer axial extents (by inference better axial resolution) than gaussian sheets both at high and low NA illumination objectives (Gao et al., 2014). However, the use of pulsed lasers and adverse bleaching effect make it unsuitable for live imaging over a long period of time. Takanezawa, Saitou and Imamura, (2021) suggests an improvement on the axial extent of Bessel beams, phototoxicity effects using a lens-axicon triplet. However, it remains to see if the reported reduced phototoxicity effect is similar or greater than that observed when using a static gaussian continuous wave laser beam.

The use of scanned Airy beams is another method for light sheet generation introduced by Vettenburg et al., (2014), and can be incorporated into an openSPIM design (Yang et al., 2014). Merits include extended depth profile, improved FOV up to 4-fold and 10-fold for Bessel and gaussian beams respectively. It is also self-reconstructing like Bessel beams but yields higher contrast. A downside to airy beams is the circular beam profile and the presence of several peak intensities. Deconvolution suggested to resolve this (rather than using non-linear excitation) assumes the position of the side lobes and thus results maybe sub-optimal. Girkin and Carvalho, (2018) suggests the true advantage of airy beams can be best harnessed when combined with adaptive optics to efficiently image deep into tissues. There is an open-source toolbox available for beam shaping using a spatial light modulator (SLM) that can be utilized within the OpenSPIM platform (Aakhte, Akhlaghi and Müller, 2018). This toolbox is capable of generating various patterns for these diverse range of illumination beams i.e., static and scanning Gaussian beams, Bessel beams, lattice beams, and Airy beams. Exploring this toolbox could be highly interesting and beneficial for researchers and users of OpenSPIM, as it offers versatile options for tailoring illumination patterns to specific experimental requirements and objectives.

Scanned beams are preferred for applications requiring high laser power, while the static version may be more suited for high speed imaging (Shah, Weber and Huisken, 2017). Mathematical expressions that define the geometry of the DSLM beam are like that of a light sheet generated from a cylindrical lens. As DSLM, Bessel, and Airy beams are beyond our scope of interest at the moment, I do not give further description on these in this text.

1.3.1 Detection Framework

The detection framework of a light sheet system is in principle that of a widefield microscope but with out-of-focus light eliminated. Fluorescence emitted from the excited plane of the sample is collected by an objective lens and imaged onto a camera detector element. More convenient is an infinity corrected microscope i.e., uses an infinity corrected detection objective (which focuses at infinity) with a tube lens. The advantage of this is that it allows the use of other optics such as fluorescence filters and dichroic mirrors in the detection path, as well as photo-manipulation of the collected fluorescence. The lateral resolution of the microscope is dominated by the NA of the detection and wavelength of emission. The ability of the setup to simultaneously detect fluorescence on the entire plane of excitation within the FOV provides an excellent temporal resolution, which is only limited by the speed of the camera and that of the sample or light sheet scanning.

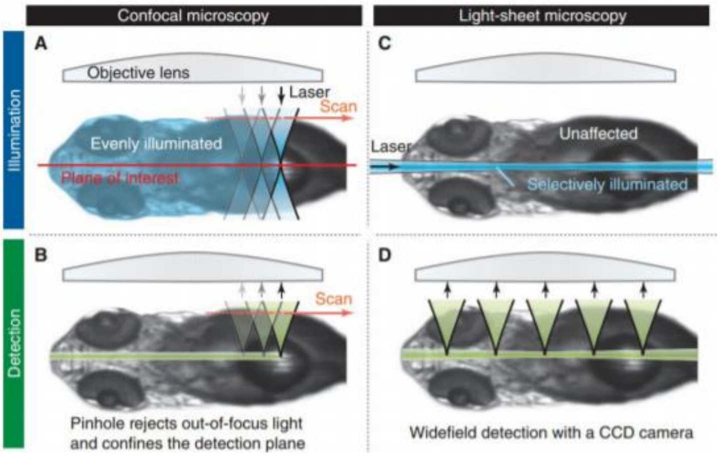

Figure 1.8. Imaging framework showing the merits of light sheet microscopy as compared to confocal microscopy. As shown in Figure 2 (Huisken and Stainier, 2009), (A, B) In confocal microscopy, illumination is done by scanning a laser beam through the sample which excites both the plane of interest and regions out of focus. Detection is done simultaneously by the point scanning of a pin hole (focused on the plane of interest) that eliminates light that is out of focus. (C, D) Light sheet microscopy, only fluorophores within the plane of interest are excited with the light sheet and simultaneously detected, thus making the technique extremely fast. The light sheet and the focal plane of the detection both overlap along the plane of interest. Adapted with permission from Huisken, J. and Stainier, Didier Y.R. (2009) ‘Selective plane illumination microscopy techniques in developmental biology’, Development, 136(12), p. 1967. doi: 10.1242/dev.022426. ‘This image is not published under the terms of the CC-BY-NC-ND (http://creativecommons.org/licenses/by-nc-nd/3.0/) license of this thesis. For permission to reuse, please see the original article.

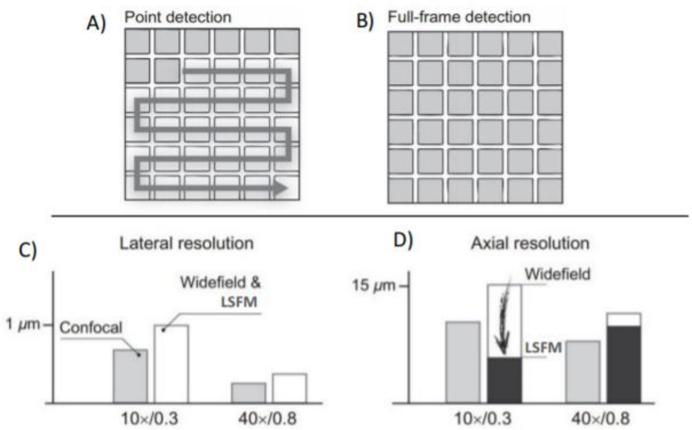

Figure 1.9: Comparing the detection unit of light sheet and confocal microscopy. As shown in Figure 11.2 (Weber, Mickoleit and Huisken, 2014). (A, B) point scanning detection in confocal microscopy is done using pin holes until the plane of interest is completely imaged, thus slowing imaging speed. On the other hand, light sheet microscopy is faster as it simultaneously detects all fluorescence from the plane of interest. (C, D) based on these framework, confocal microscopy has a better lateral resolution. However, light sheet microscopy can have a better axial resolution when an objective lens of suitable NA for illumination. Adapted with permission from Weber, M., Mickoleit, M. and Huisken, J. (2014) ‘Chapter 11 - Light sheet microscopy’, in J.C. Waters and T. Wittman (eds) Quantitative Imaging in Cell Biology. Academic Press (Methods in Cell Biology), pp. 197. Available at: https://doi.org/https://doi.org/10.1016/B978-0-12-420138-5.00011-2. This image is not published under the terms of the CC-BY-NC-ND (http://creativecommons.org/licenses/by-nc-nd/3.0/) license of this thesis. For permission to reuse, please see the original article.'

Charge Coupled Device (CCD) and mostly Scientific Complementary Metal Oxide Semiconductor (sCMOS) cameras are commonly deployed, depending on the imaging capabilities the microscope was designed for. Electron Multiplication CCD (EMCCD) are fitted with silicon chips; an array of light sensitive detector elements (photodiodes) and related electronics, that capture fluorescence photons emitted from the sample and release photoelectrons (photoelectric effect) in a probabilistic distribution. During the exposure period of the camera to collect image fluorescence (exposure time), photoelectrons accumulate (charge packet) and are held on each photodiode to a maximum amount, depending on the full well capacity (FWC) of the photodiode. The charge packets are then pixelated I.e., each photodiode can be set to form a pixel in a digital image, and the charge packets converted to an appropriate range of gray pixel values by an amplifier and an analog-to-digital converter, depending on the voltage values the charge packets carry. Clearly cameras with a larger number of detector arrays and smaller pixel sizes are to be desired (Lambert and Waters, 2014).

1.3.2 Sample Mounting

Several sample mounting techniques exist depending on the sample size and shape, the orientation of the light sheet and the detection, i.e., either a vertical or horizontal setup. Vertical systems such as the ultramicroscope have the focal plane of the detection aligned to the horizontal, vice-versa for horizontal systems. Translational and rotational stages are used to move the sample into position during imaging. An advantage to horizontal systems is the ease of sample mounting (usually from the top of the imaging space/chamber) and movement, without distortion.

Certain media might be required during imaging to support physiological conditions (during in-vivo studies) or Refractive Index (R.I) matching i.e., the refractive index of the media that will exist between the sample and the illumination and detection lens. An ideal case would have all media having their refractive indices matched to that of the sample to allow for good image quality and reduced aberrations. However, there is usually a bit of compromise depending on a couple of factors which will be discussed in detail later in this text. It is often a good practice to align the long axis of the sample to the horizontal when imaging on vertical systems, and to the vertical when imaging on horizontal systems. This allows to image larger samples and reduces the volume of secondary photon excitations in the optical path between the front lens and focal plane of the detection.

Samples can be embedded in a solid cylindrical gel usually made of 1 – 1.5 % low melt agarose (**gel embedding**) protruding from a capillary tube or syringe onto the path of the light sheet. This is useful to immobilise the sample and provide reproducible movement into defined coordinate space. Gel embedding is more suitable for specimens that do not change in size and shape (Reynaud *et al.*, 2008; Kaufmann *et al.*, 2012). Developmental studies and cases that require high temporal resolution to capture salient biological processes may require **tube embedding**. This helps to keep the sample as static as much as possible to avoid blurs during imaging, without impeding the physical space required for biological development. In such cases, Fluorinated Ethylene Propylene (FEP) tubes are suggested largely because they have a R.I (1.34) close to that of water or PBS (~1.33) which supports physiological conditions for in-vivo studies. FEPs are cleaned with EtOH, Sodium Hydroxide – NaOH, water, and ultrasonication before use. Samples are then pulled into the FEP tube with an agarose gel of concentration rigid enough to hold it in place within the tube and imaged in water as-is. More convenient for sample growth during imaging is to suck it into the FEP tube with a lower concentrated agarose gel (~ 0.1 %) and plug the base of the tube with about 1 - 3 % concentration agarose (Kaufmann *et al.*, 2012).

Fluorescent beads are often evenly dispersed in the block of agarose which are useful for post-acquisition processing.

Some larger samples such as whole mouse brain, or whole organisms that cannot easily be embedded may need to be imaged without sectioning. Such can be glued to a platform or suspended from a hook.

Content has been removed due to copyright restrictions. Please see pages 6 and 7 here:

https://hcbi.fas.harvard.edu/files/lightsheetz1_sample-preparation_zeiss.pdf

Figure 1.10: Sample mounting methods (Flood *et al.*, 2013. p7). Samples can be in different sizes (small - 10 µm, medium - 100 µm, large - order of mm, very large - order of cm) and are mounted on a light sheet platform based on size, shape, and the hardware setup of the microscope. They can be (A) gel embedded, (B) attached to a hook or clip (C) tube embedded. Side view shows the orientation of the light sheet relative to the detection objective, and the position of the mounted sample.

Other mounts such as clamps and clips can also be designed, and 3D printed with materials compatible with the imaging solvent and the sample they are intended for. In other cases samples can be trapped within a cuvette, or made to sit at the bottom of an imaging chamber or larger cuvette and the light sheet scanned through them or the entire chamber with the sample moved through the light sheet (Chakraborty *et al.*, 2019; Voigt *et al.*, 2020).

1.3.3 Image Resolution and Image Quality

1.3.3.1 Lateral and Axial Resolution

The Numerical Aperture (NA) of a lens is of primary importance in achieving excellent resolution on an imaging platform. It is defined as a measure of how much light it can capture from point sources on a fixed distant object to resolve image details, and is dependent on the diameter of the entrance pupil of the lens and its focal length.

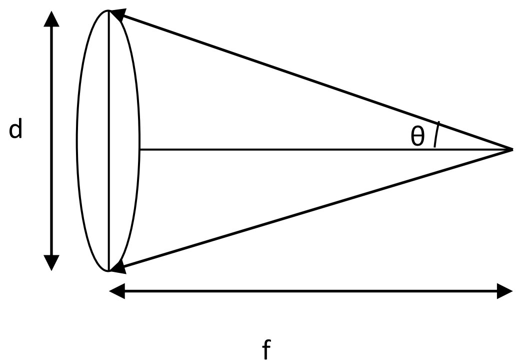

Figure 1.11: The numerical aperture of a lens depends on its diameter d, focal length f, the imaging media, and the angle of the cone of focused light through the lens.

$$NA = n \sin\theta \qquad 1.9$$

$$\frac{f}{d} = \frac{n}{2(NA)} \qquad 1.10$$

θ is the half angle of the cone of light exiting or entering the lens pupil (front of the lens). f is the focal length, d is the aperture diameter, and n is the refractive index of the imaging media (n=1 for air).

The resolution of an imaging system refers to the minimum resolvable distance between two-point sources of light from an object. Though not dependent on the system magnification, for a light sheet microscope, it is primarily determined by the numerical aperture (NA) of the illumination and detection len(s) or objective(s).

Rayleigh criterion is useful in estimating the resolution of an optical system. It states that two closely packed diffraction patterns (Airy disks) generated by point sources, or a small circular aperture can be distinctly observed if they are farther apart than the distance at which the first minimum of one disk coincides with the principal maximum of the other. If both sources have the same wavelength, both disks will have the same diameter and the resolution of the system can be taken as half the diameter, which is the radius of a disk from its peak intensity to the first ring of minimum intensity (Garini, Vermolen and Young, 2005).

Content (top image) has been removed due to copyright restrictions. Please see the top image here:

https://webmail.life.nthu.edu.tw/~g874215/confocall/NA.htm

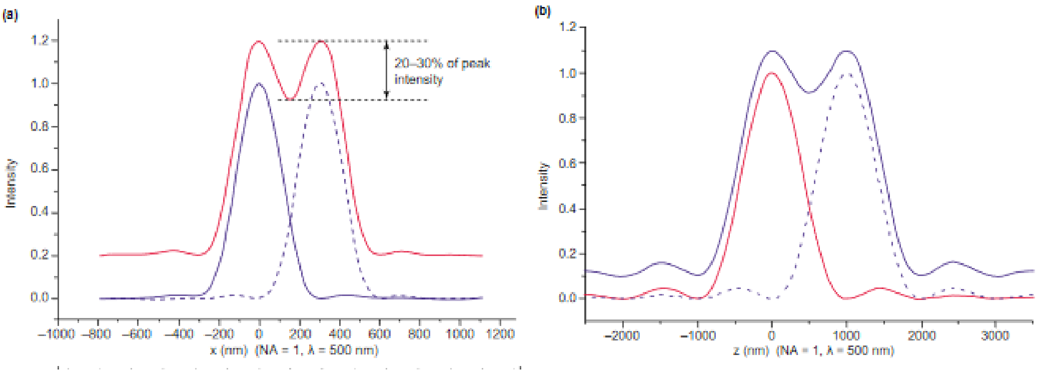

Figure 1.12: Rayleigh Criterion for a conventional microscope. As shown in (National Tsing Hua University, no date; Garini, Vermolen and Young, 2005), **Top image:** (a) An airy disc consisting of a diffraction pattern which includes a principal maximum intensity and other higher order maximums corresponding to decreasing brightness. (b) Diffraction pattern for two-point sources that are closely packed. The distance between their principal maxima exceeds their radii, thus they are resolvable. On the other hand, the distance between the principal maxima in (c) is lesser than their radii and makes the two-point sources unresolvable. **Bottom left** - (a) Lateral resolution - the distance between the two-point sources should be that between the peaks of the solid and dashed blue lines for them to be distinguishable, and the total intensity plot of both sources (red line – physically shifted upward) should have a minimum that is between 20 – 30 % of the peak total intensity value. **Bottom right** – (b) Axial resolution, which is usually worse than the lateral view. Bottom images adapted from Garini, Y., Vermolen, B.J. and Young, I.T. (2005) ‘From micro to nano: recent advances in high-resolution microscopy’, Current Opinion in Biotechnology, 16(1), pp. 4, with permission from Elsevier.

The lateral resolution (equation 1.11) and axial resolution (equation 1.12) of a conventional microscope defined by the Rayleigh criterion states:

$$r_{lateral} = \frac{0.61\lambda}{NA} \quad 1.11$$

$$r_{axial} = \frac{2\lambda}{(NA)^2} \qquad 1.12$$

The lateral resolution of a LSFM system is dominated by the NA of the detection objective as there is a simultaneous detection of all fluorophores within the excited plane. The axial resolution is dominated by the thickness of the light sheet. For easy comparison of theoretical and experimental values, it is more useful to represent the resolution of a system (Rayleigh criterion) as the FWHM. Gao *et al.*, (2014) gives a reasonable approximation of lateral (1.13) and axial resolutions (1.14) of a light sheet microscope.

$$r_{lateral} = \frac{\lambda_{em}}{2NA_{\det}} \qquad 1.13$$

$$r_{axial} = \left(\frac{2NA_{exc}}{\lambda_{exc}} + \frac{n(1-\cos\theta_{\det}}{\lambda_{em}} \right)^{-1} \qquad 1.14$$

$$\text{Light sheet thickness} = \frac{\lambda_{exc}}{2NA_{exc}} \qquad 1.15$$

NA_{exc} and NA_{det} are numerical apertures of illumination and detection objectives. n and Ɵ are the refractive index of the imaging buffer and the half-angle of light collection, respectively. λ_{em} and λ_{exc} are the emission and excitation wavelengths, respectively.

NA of detection objectives chosen should be large enough to resolve to the required sample detail. This is considered relative to the optical arrangement on the illumination axis and the field of view. An ideal setup on a light sheet microscope is to ensure the light sheet thickness is uniform across the field of view of the detection. High NA illumination objectives lenses should give a thinner light sheet and thus better system axial resolution. However, they have a shorter axial extent for which the light sheet is uniform and are more suited for relatively small and optically transparent samples. On the other hand, low NA objectives give thicker light sheets and the axial length with uniformity is longer. Huisken *et al.* (2004) demonstrates using a thicker sheet can improve image contrast for large samples, and Keller *et al.* (2011) suggests using a Gaussian light sheet thickness between 2 µm and 10 µm, 4 µm for best compromise. It is useful to note that since high NAs are preferred for better lateral resolution, combining with an optimally low NA illumination may still be better for all sample sizes as post-acquisition image processing can improve image details.

In light sheet microscopy, a way to increase the collection of emitted fluorescence photons is to use immersion objectives separated from the sample only by media of suitable refractive index. This technically widens the range of angle for light detection, resulting in improved resolution and image quality.

1.3.3.2 Sample Clearing and Refractive Index (R.I) Matching

Whole sample imaging without 'sectioning' is desired in light microscopy as it aids better study of biological mechanisms without introducing 'external disturbance'. One challenge with this is that samples could be opaque and light scattering. To overcome this, a solution well adopted in microscopy beyond histological sectioning is 'clearing' the sample. In simple terms, light absorption and scattering occurs due to the different refractive indices of components such as lipids, proteins, and water within tissues. Tissue clearing helps to homogenise their R.I thereby making samples optically transparent to allow imaging of whole intact samples (such as whole mouse brains). In any research, the clearing method adopted is based on the interest of the study, and the availability of the microscope composition required to resolve down to the desired image details. Table 1 in Parra-Damas and Saura, (2020) gives a summary on different clearing methods, their merits and demerits, in addition to detailed notes.

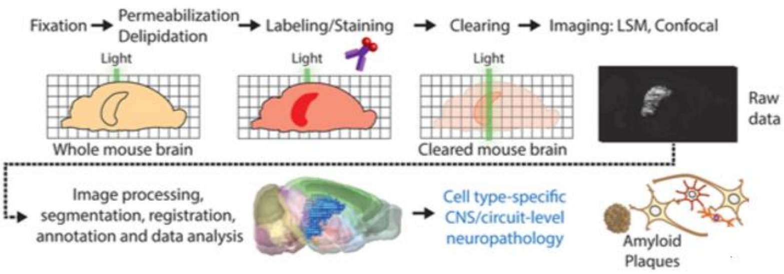

Figure 1.13: General steps involved in clearing intact samples, imaging, and analysing. As shown in Figure 1 (Parra-Damas and Saura, 2020). Adapted with permission from Parra-Damas, A. and Saura, C.A. (2020) 'Tissue Clearing and Expansion Methods for Imaging Brain Pathology in Neurodegeneration: From Circuits to Synapses and Beyond', Frontiers in Neuroscience, 14 (October), p. 3., under the terms of the Creative Commons Attribution License (CC BY).

In any study, the refractive indices (R.I) of the sample, objectives lenses, and the medium in which imaging takes place should ideally be matched (i.e., be the same). In practice, this is clearly never the case as reasonable R.I approximations are usually made. In most cases, the norm is to embed the sample in a gel solution (usually agarose gel with 1 – 3 % concentration) or a tube (such as FEP tube) with R.I similar to that of the other imaging environment (I.e., similar to that of the cleared sample and the imaging buffer - such as water), and use objective lenses corrected for such. This ensures the detection of more fluorescence light (by widening the range of angles of the objective lens for light detection) which otherwise would have been lost, and limits spherical aberrations. Samples not embedded but suspended freely in the imaging space still need R.I matching.

In-vitro imaging of cleared samples could be more challenging as immersion objectives customised for certain clearing solvents are readily not available and could be very expensive

(~ 10, 000 – 50,000 Euros per piece). Some imaging solvents used as buffers also do not come cheap. Therefore, in building or buying a light sheet microscope, considering that a microscope is useful to the degree at which it can conveniently image live and cleared samples of a wide range of sizes, there is usually a trade-off between the type of objectives, clearing method, imaging buffer, and sample mounting technique used. Usually, the use of air objectives for illumination, immersion or air objectives for detection, and an imaging buffer matched to the refractive index of the sample can support imaging a wide range of samples without too much overhead cost.

1.3.3.3 Image Sampling - Camera Efficiency, Pixel Size, Field of View (FOV)

Image sampling refers to the collection of a subset of spatial and temporal information from an object which eventually contributes to the final representation of the image. For a 3D dataset, several 2D planes are acquired in the Z-direction at step sizes that are sufficient to capture the desired features of interest. Several factors are to be considered for optimal image sampling.

1.3.3.4 Camera Efficiency

The image quality of a microscope also depends on the efficiency of its camera in capturing photons and converting them to digital images. These can usually be reported as the quantum efficiency and noise in the device specification sheet provided by the manufacturer. The quantum efficiency refers to the average percentage of photons converted to photoelectrons on impact with the silicon chip (Pawley, 2006). The higher the value, the better, and this well depends on the wavelength of the photons and to a lesser extent temperature. The camera noise can be described as the variations or uncertainty in pixel intensity values i.e., a corruption of the image signals (photoelectrons) by unwanted signals (electrons) from different sources. Consequently, a quantity usually used to describe the quality of an image is the ratio of the image signal to noise present (Signal to noise ratio – SNR). There are four known dominant noise sources.

Fixed pattern noise is spatially consistent between images i.e., 'fixed' and arises from the between-pixel variabilities that stem from the differences in the efficiency of each photodiode in capturing the photoelectrons (Janesick, 2007). As a photodiode in sCMOS cameras is designed to have its own signal to pixel intensities readout amplifier, fixed noise is more noticeable in sCMOS cameras. Flatfield correction is a common method for resolving fixed noise.

Read noise occurs because of the uncertainty in the reading of the charge packets by the amplifier of the camera and increases with the read-out speed. Often this noise can be measured by collecting a dark image (with no light photon sources impinging on the detector) which will have a distribution of pixel values about a mean gray value that represents a zero photon (camera offset). The standard deviation of the distribution is designated the read noise. Relative effect of read noise can also be reduced by increasing the number of collected photons (such as increasing the power of the sample illumination, using relatively large NA objectives and image buffering), and not necessarily increasing the exposure time (Rasnik *et al.*, 2007; Waters, 2009).

Poisson noise is due to the random number of photons arriving at the photodiodes within a given time interval and follows a Poisson distribution. The relative impact of Poisson noise can be limited by increasing the exposure time of the camera during acquisitions to collect more photons (Sheppard *et al.*, 2006). Also in light sheet microscopy, image reconstruction algorithms robust to Poisson noise may also exist (Preibisch *et al.*, 2014).

Thermal noise also referred to dark noise occurs due to electrons released from the increase in temperature of the silicon chip, and for this reason cameras are often advised to be kept cool (Lambert and Waters, 2014).

Cameras with a higher bit depth are preferred as they provide a higher dynamic range sufficient for intensity sampling.

1.3.3.5 Pixel Size, Field of View, and System Magnification

The size of the smallest element of a picture that conveniently samples an object and combine to comprise the final image is referred to as the sampling pixel size, while the smallest element size physically available on the detector array of the camera sensor is the camera pixel size. Image magnification refers to how much the size of an object can be scaled up or down by the imaging system. The Field of View (FOV) is the area of the sample that can be imaged based on the components that comprise the microscope, and determined by the magnification of the detection (which is the system magnification) and the camera pixel size. If there are no optics in the path between the detection objective and the camera, the system magnification for a light sheet microscope using an objective that focuses the image rays directly onto the detection is that of the detection objective. Images from the circular FOV of the detection objective are relayed onto the square shaped sensor of the camera. It is therefore important to optimally fit the FOV into the size of the sensor to capture the full image dimensions as much as possible.

Mathematically;

$$\text{FOV} = \frac{\text{Size of the Camera Sensors}}{\text{Objective Magnification}} = \frac{\text{Size of the Camera Sensor}}{\text{System Magnification}} \qquad 1.16$$

$$\text{Size of the Camera sensor} = \text{number of pixels X camera pixel size} \qquad 1.17$$

However, it is more useful to use infinity corrected objectives for detection (which focuses the image rays at infinity). This allows for image manipulation by the introduction of more optics (such as fluorescence filters, dichroic mirrors, and magnification modules) in the space between the objective and the camera. In such cases, the image rays are refocused onto a camera with the aid of a tube lens of known focal length. These additional optics may alter the system magnification.

If the extra magnification is introduced only by the tube lens, then the system magnification of an infinity corrected microscope becomes:

$$\frac{\text{Focal length of the tube lens}}{\text{The nominal focal length of the tube lens the objective is designed to work with}} \qquad 1.18$$

If an optic introduces extra magnification (M) beyond that of the tube lens, then the magnification of the infinity corrected microscope will be 1.18 multiplied by (M) i.e., for all additional optics modules in the detection that alter the system magnification, I keep multiplying by the magnification of the module to get the resultant system magnification.

Focal lengths for tube lens are usually known to have standard values. For Olympus - 180mm, Zeiss - 165mm, Nikon, Thorlabs, and Leica - 200mm. These are particularly useful in calculating the focal lengths of their corresponding objectives, which is the ratio of these standard values to the specified magnification of the objective.

The sampling pixel size must have the capacity to properly sample the FOV of the planes being imaged and should not be lesser than the resolution of the detection objective. For a good signal to noise ratio (SNR), the quantum efficiency of the detector should also be highest at the range of emission wavelengths of fluorophores of interest to capture a good number of fluorescence photons relative to the background noise.

The temporal resolution of a light sheet microscope is a function of the speed of acquisition, which is often dependent on the camera frame rate, the speed of scanning a light sheet through the sample or vice versa. Having multiple detection views is also critical to image resolution (especially when studying fast nuclear morphology). The amplitude of scanning mirrors and the speed of translation stages may be limited, and as such miss out on fast transient biological processes during acquisition.

1.3.3.6 Point Spread Function (PSF)

The theoretical definition of the resolution of a microscope assumes imaging an ideal sample without light scattering and no aberrations from the microscope optics. In practice this is often not the case. The point spread function (PSF) helps to describe resolution and is best measured experimentally (for example imaging fluorescent beads) as each lens is different in performance.

The PSF describes the energy distribution in the image of a point source through space and is a quantity dependent on the imaging system. Ideally, the PSF is the diffraction pattern (Airy disc) of the image of a point source when there is no aberration (which is usually not the case). The symmetry of the distribution of a point source laterally and axially is an indicative of the quality of the imaging objective lens. Images produced from the microscope are a summation of all overlapping PSFs of point sources, described mathematically as;

$$I_{image} = I_{object} \otimes PSF \qquad 1.19$$

i.e., the image I_{Image} is a projection of the object I_{Object} blurred by convolving it with the PSF of the imaging system.

The PSF of a light sheet microscope is anisotropic (elongated), the extent to which depends on the NA of the illumination and detection. As the axial resolution is much poorer than the lateral due to light sheet thickness optimality, a goal in imaging is to ensure they are as similar as much as possible (Isotropy) (Waters, 2009; Goodwin, 2014). This can be achieved by choosing the right combination of objectives, acquiring different views of the same sample and then improving the poor axial resolution with the superior lateral when fusing them. More is described on this in the section on image processing.

1.3.3.7 Image Acquisition and Processing

Acquiring multiple views of a sample and fusing them can compensate for image degradation in the illumination direction as well as the anisotropy in the PSF. This involves acquiring several planes to form a stack, and then rotating the sample to acquire consecutive views of different stacks. If at least one of the corresponding views for each plane has an optical penetration up to half the thickness of the sample, they can be fused computationally to give a single high isotropic resolution stack. (Huisken *et al.*, 2004; Greger, Swoger and Stelzer, 2007; Verveer *et al.*, 2007). Further more, multi-tile multiview imaging helps to acquire the full dimensions of large sample that do not fit into the FOV of the microscope. Here, each optically sectioned plane is first tiled into a grid, after which the different coordinates of the grid are imaged. This is done for each slice in a stack and then the whole process is repeated to record stacks for different views.

Image quality depends on reconstruction algorithms. Following acquisition, the views are first registered into the same space. The registration step could be Bead, Intensity, or Segmentation based. Intensity based algorithms require no embedding of beads and are sample independent. However, they are slow, hardly cope with developing samples, and results are difficult to verify automatically (Swoger, Huisken and Stelzer, 2003; Huisken *et al.*, 2004; Verveer *et al.*, 2007). Feature segmentation algorithms are also fast, require no embedding, and can be verified automatically. Coping with developing samples is however difficult and it requires staining (Keller *et al.*, 2008, 2010; S Preibisch *et al.*, 2008). Bead based algorithm though requires embedding fluorescent beads in a rigid medium, it is fast, sample independent, and suitable for developing samples and results can be verified automatically (Preibisch *et al.*, 2010). For these reasons it is widely adopted than the other two registration methods in light sheet microscopy. The beads segmented in each view are compared to establish correspondences between views using a rotationally invariant local global descriptor, and results in a transformation model that is used for the 3D registration. If a time-lapse data is acquired, a further inter-timepoint registration is done in a similar way.

Following image registration, the data set is fused into a single isotropic 3D volume. There are several methods to do this suggested in literature, ranging from comparing corresponding voxels in the frequency domain and keeping the highest magnitude pixel in the final output i.e., spectral average weighting (Swoger, Huisken and Stelzer, 2003; Huisken *et al.*, 2004), to several multiview deconvolution techniques (Verveer *et al.*, 2007; Tomer *et al.*, 2012; Wu *et al.*, 2013; Preibisch *et al.*, 2014; Chhetri *et al.*, 2015). Two algorithms for fusion that are widely adopted in the SPIM community are the content-based multiview fusion (Stephan Preibisch *et al.*, 2008), and the Efficient Bayesian-based multiview deconvolution (Preibisch *et al.*, 2014), particularly for its robustness in dealing with large datasets.

In content-based multiview fusion, parameters of the transformation model used in the registration step are employed. Rather than averaging corresponding pixel values in different views that lead to a degradation of the signal in regions with high SNR in certain views, non-linear blending and content-based weighting are done i.e., a local content evaluation is done on the overlapping sections of the different views such that those with higher SNR are made to contribute more to the fused image. A downside to this method is that the output is not suitable for quantitative analysis as it alters the data of the raw images. Laterally, the final output when compared to the raw single views is degraded in quality. Multiview deconvolution eliminates this limitation in fusion.

Deconvolution is a mathematical process that helps to deblur or restore the image of an object to a good approximation, given the PSF of the imaging system. Richardson Lucy deconvolution algorithms are preferred because they perform better in terms of fusion quality and convergence speed. Importantly, the 3D Efficient Bayesian-based algorithm jointly deconvolves the different views (simultaneous deconvolution and fusion) by employing the use of conditional probabilities in-between views. For a detected photon from a fluorophore in an observed view, the PSF is expressed as a probability distribution used in assigning probabilities to every pixel location (in its underlying/deconvolved image) for defining the chance the photon was from a location. Consecutively for different views, probabilities are assigned to pixel locations in their corresponding underlying image on detecting a photon from the same fluorophore. The idea is to establish what underlying distribution (i.e., the deconvolved image) best explains all observed distributions (views) based on their given conditional probabilities (PSFs).

Richardson Lucy iterations consists only of convolutions and pixelwise arithmetic operations, and in addition to the Bayesian-Based deconvolution approach is shown to outperform most algorithms that individually deconvolve each view prior to fusion i.e., significantly reduces the number of iterations needed to achieve the desired image quality and the time required for each iteration (Preibisch *et al.*, 2014).

Multiview deconvolution or fusion is computationally expensive. It is therefore important to invest in high end processing hardware with CUDA capable GPUs, or to parallelise computing on a cluster. Real time deconvolution may be less demanding on hardware and faster, but it is at the expense of image quality (Schmid and Huisken, 2015). Deconvolution at high sample depths may also be sub-optimal due to degradation of the signal, and some studies have suggested combining it with Optical tomography (Filtered back-projection) (Mayer *et al.*, 2014; Lin *et al.*, 2015). Optical tomography though works with fluorescent and non-fluorescent contrast (Mayer *et al.*, 2014; Bassi, Schmid and Huisken, 2015), it still does not produce quality images at cellular and subcellular level. During fusion, in compensating for axial resolution, the inherent reduction in lateral resolution is more pronounced if an insufficient number of views are acquired. On the other hand, an increase in views acquired introduces more bleaching effect especially where there is only one detection and illumination axis. Sequential multiview imaging (sample motion through the light sheet) with one illumination and detection setup could also lose information on transient developmental processes occurring during the time shift between acquisitions of complimentary views. As in any imaging setup, there is a potential trade-off between spatial and temporal resolution in such multiview systems. As such, systems with dual illumination and detection arms are suggested to strike a balance on achieving good speed and image quality, while limiting photobleaching effect.

The interactive visualisation of 3D terabyte sized datasets, speed and quality of alignment becomes more complex to deal with when reconstructing multitile multiview datasets. The BigStitcher software was specifically developed for this and acts as a choice tool box. In addition to providing options of existing algorithms such as; the conversion of large datasets to a multiresolution compressed and blocked (HDF5) format which can be viewed interactively with the BigDataViewer (Hörl *et al.*, 2018); bead-based registration; and the efficient bayesian-based multiview deconvolution, it further implements the stitching of tiles by using algorithms that calculate shifts between image pairs (pairwise shift calculation). Such can be done individually for each angle (which may involve more than one channel) and timepoint before multiview registration (gradient descent - interest point and intensity based method, and phase corellation method) or after multiview registration (gradient descent - intensity based method, and phase corellation method).

CHAPTER 2 Materials and Methods

2.0 Building a cost-effective L-openSPIM for millimetre sized tissues using in-air optics: What you should know.

Commercial light sheet microscopes are significantly expensive ($250,000 - $500,000) (Marx, 2016), and are not easily re-engineered to meet research needs. Potentially there always will be a knowledge gap between optical physicists and biologists (Lemon and McDole, 2020). As such there have been several attempts to describe open-source do-it-yourself (DIY) light sheet microscopes (Girkin and Carvalho, 2018; Stelzer *et al.*, 2021). Arguably, Pitrone *et al.* (2013), Girstmair *et al.* (2016), and Girstmair *et al.* (2022) provide the simplest practical details (relatively) on building a cost effective light sheet microscope; the L-OpenSPIM, T-OpenSPIM, and X-OpenSPIM platforms respectively. The L - OpenSPIM being the least expensive as it is of the least configuration (less than €50,000). Though these prove useful, Pitrone *et al.* (2013) description of the L-OpenSPIM does not capture details required for a finer light sheet alignment in different imaging buffers, which is critical for imaging cleared samples. Instructions in Girstmair *et al.* (2016) and Girstmair *et al.* (2022) are for builders with some prior experience of developing a L-OpenSPIM or access to personnel with the required practical experience. Also, the published instructions are more tailored towards in-vivo imaging than for large (> 1 mm) or cleared samples. A ground-breaking open-source initiative for producing high resolution raw images of large intact cleared samples is the mesoscale SPIM (mesoSPIM) (Voigt *et al.*, 2020). It is however very expensive (~$170,000 - $250,000), and the authors advise potential builders of the platform that prior experience of DIY light sheet microscope is required. Scientists (especially biologists) new to light sheet technology are usually interested in imaging samples of different sizes in-vivo or in-vitro (naturally or solvent cleared samples) at different times depending on the current research focus. A lack of technical know-how always makes it challenging to know what type of light sheet microscope is best suited to the current research needs and can be easily upgraded for future purposes. In addition, funding is usually limited. It is therefore advised that interested scientists should learn how to build a light sheet microscope, starting off with a basic platform (preferably the L-openSPIM) to gain practical experience needed to advance into more complex designs. This ultimately reduces the need to keep buying off-the shelf platforms and ensures DIY microscopes are not abandoned due to operational and maintenance challenges.

Here, I detail key considerations in choosing and assembling the L-OpenSPIM parts described in Pitrone *et al.* (2013), using in-air optics and modifications needed to image up to millimetre sized samples in-vivo and in-vitro, while still keeping cost relatively low. More practical insights such as finer light sheet alignment, choice of image acquisition software, and efficient data saving formats are documented. I show the ability of our SPIM platform to produce quality 3D images of a millimetre sized V*arroa destructor* (~2 mm), and to distinctly resolve to cells in the highly motile optically transparent head of a *Hydractinia symbiolongicarpus* (100 – 200 µm wide, 200 – 400 µm height). I also highlight possibilities to upgrade the system and details to improve the performance of the microscope.

2.1 Design

It is necessary to design a Selective Plane Illumination Microscopy (SPIM) platform around samples and their features of interest. Are the samples planned small (~10 µm), medium sized (~100 µm), large (order of mm), or very large (order of cm)? What sample details do I plan to resolve down to (spatial resolution)? and how fast (temporal resolution)? The cost of required parts is also a key factor. Are the parts suggested on Pitrone *et al.*, (2013b) adequate? or are cheaper alternatives sufficient in achieving the needed resolution? Can the parts be easily purchased off the shelf or need to be forged in a workshop? In any case it is important to adopt a design that is user friendly and can deliver the desired quality results.

A good idea is to start off with an established design that fits within available financial budget. This helps to get familiar with system calibration, usage, and capabilities. Learning outcomes and results can then largely inform future upgrades. It is important to note that deviating from the basic design on Pitrone *et al.*, (2013b) may mean more cost, time for purchasing (or forging) parts, time for assembly, and testing. Owens, (2017) suggests useful information on issues to consider when designing a do-it-yourself (DIY) microscope. In my case, I started off with a platform that can image up to millimetre-sized samples and resolution enough to visualise neurites. There are several established L-OpenSPIM microscopes which have been used for biological studies published in literature. One which informed our basic start-up is the design described in Stefaniuk *et al.*, (2016), based off the L-OpenSPIM design and has been shown to image an intact rat brain at neurite resolution, though much improvement is desired. Table 2.0 shows a list of parts I adopted from the basic L-OpenSPIM design on Pitrone *et al.*, (2013b) Other extensions or alternatives I purchased or made in our workshop are also grouped within Table 2.0 and I will discuss why I made these changes.

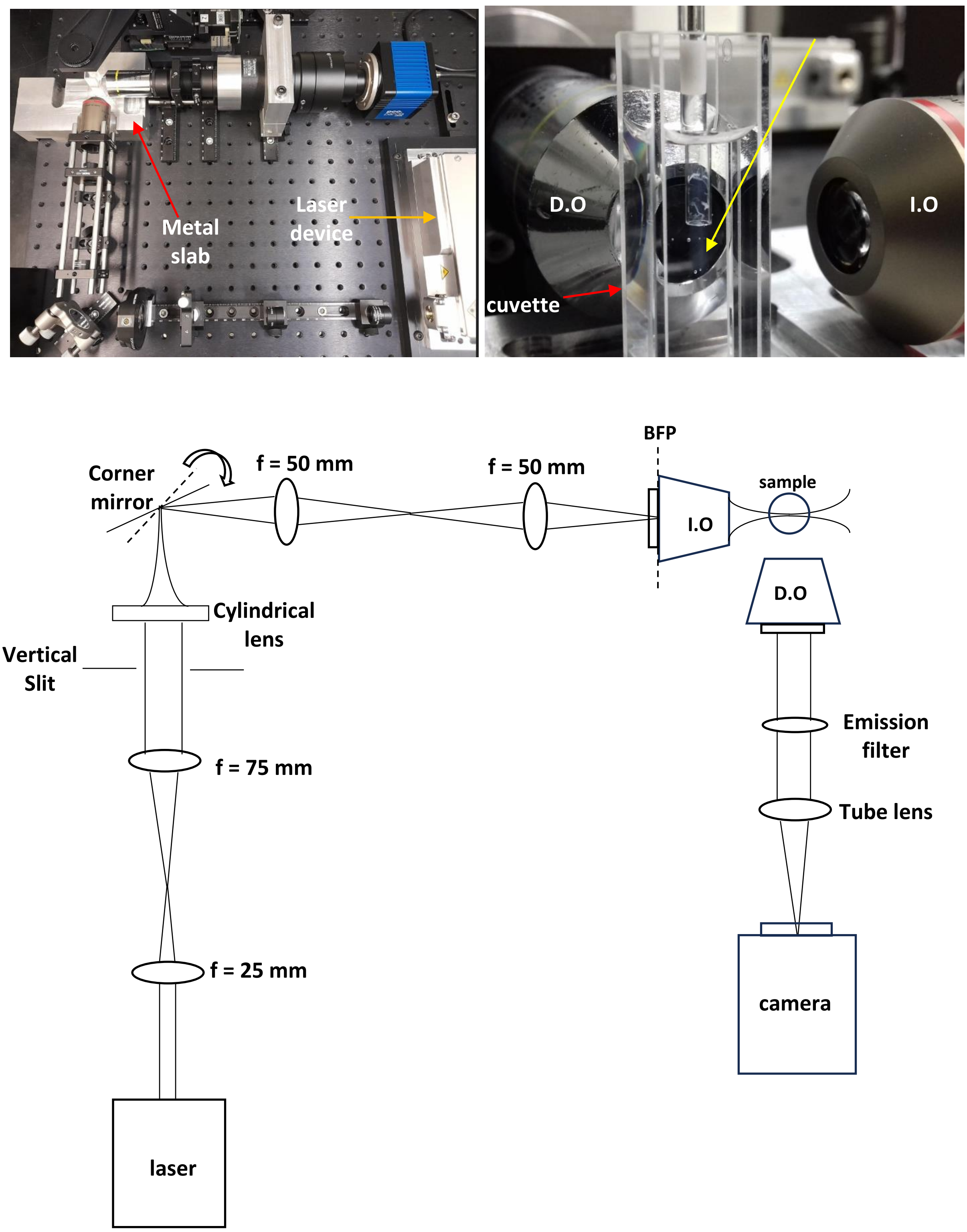

Figure 2.0: L-OpenSPIM at the University of Galway, Ireland. Top left shows the top view of the setup. Top right image shows the illumination objective (I.O), detection objective (D.O), agarose suspended in the water buffer by a capillary tube. Image at the bottom is an optical diagram of the setup at the top left. Laser beam is expanded by the beam expander 1 (f = 25 mm, f = 75 mm) and projected to a cylindrical lens through a vertical slit. The cylindrical lens forms the light sheet on the corner mirror. A relay telescope (f = 50 mm) then images the light sheet unto the back focal plane (BFP) of the illumination objective (I.O) and the light sheet is formed at the front lens of the I.O. Emitted fluorescence collected by detection objective (D.O) is passed through an appropriate filter and then the tube lens focuses the beam on the sCMOS camera.

2.2 Extensions – Illumination Axis

2.2.0 Illumination Objective

As earlier discussed, relatively thicker light sheets are preferred for large samples as they are more uniform for a larger field of view (FOV). 4μm thickness is suggested to be best compromise (Keller *et al.*, 2011). The 10x - 0.3NA dipping objective used on the L-OpenSPIM described on Pitrone *et al.*, (2013b) when combined with our 488 nm laser line will give a light sheet thickness of ~ 0.8 μm (which is much narrower than 4 μm). This might improve for longer wavelengths, but even at 1000 nm excitation (which is rarely used in microscopy) the thickness of the light sheet will still be ~1.7 μm. More so, the objective has a working distance of just 3.5 mm which will not give enough space to conveniently scan large intact samples (which can be centimetres in length) through the light sheet. I also planned to image different samples in different imaging buffer. Immersion objectives and dipping caps with exact specifications needed might not be commercially available and those that are could be very expensive ($15,000 to $35,000 per piece). Thus, I needed a different illumination objective with a longer working distance and a numerical aperture low enough to generate a relatively thicker light sheet with the 488 nm line. An alternative is to combine an air objective with the appropriate imaging cuvette that can house any imaging buffer. At the time of building our SPIM, an air objective that meet our demand and is readily available within our budget is the Nikon CFI - 4x Plan Fluorite with a 17.2 mm working distance and 0.13 numerical aperture. This brings the light sheet thickness to ~1.8 microns and can be quite useful when incorporating laser lines of longer wavelengths. The objective also offers good transmittance (~ 90 %) within the 400 nm to 700 nm illumination range.

2.2.1 Beam Expander - Achromatic doublets

The L-OpenSPIM design on Pitrone *et al.,* (2013b also incorporates two telescopes (beam expanders – B.E). One for expanding and collimating the laser beam to the required diameter that can fully illuminate the back focal plane (BFP) of the illumination objective ($B.E_1$), and the other to image the BFP of the illumination objective to the corner mirror ($B.E_2$) in addition to scaling the height of the light sheet to fit the BFP where needed. Since I used an alternative illumination objective, this influences our choice of lenses (achromatic doublets) that make up both telescopes.

The diameter of our laser beam is 0.7 mm. From equations 1.15, the light sheet thickness for our illumination objective is ~1.8 µm, and thus the beam waist ω_o is 0.9 µm. From equation 1.5, the Rayleigh range can be calculated to give 6.94 µm. Considering that the standard focal length for the tube lens used in marking the magnification of Nikon objectives is 200 mm, for our 4x Nikon objective, its focal length will be 50 mm. Focusing the gaussian beam in water with refractive index 1.33, the diameter of the BFP can be estimated using equation 1.7 to be 12.97 mm, ~13 mm. I can validate this value with the approximate formula for calculating the BFP for an objective i.e., BFP = 2*f*NA for small angles. Focal length (f) = 50 mm, and Numerical Aperture (NA) = 0.45, and thus BFP = 13 mm.

Thus, to fill up the entire BFP of the illumination objective, I should expand the beam by a factor of 19 i.e., the ratio of the BFP diameter to the original beam diameter. Using the full NA gives a light sheet thickness of 1.88 µm approximately, and observing the profile of the light sheet shows it suboptimal uniformity across the 1.48 mm FOV. Most samples planned for imaging on the microscope are $\geq$ 1 mm in size. As earlier discussed, thicker light sheets are preferred for that. Thus, it is useful to get the thickness close to 5 – 10 µm suggested in literature as much as possible. I can do this by limiting how much the beam is expanded while still using the same illumination objective, I experimentally observed a 3x expansion gave optimal light sheet uniformity across the FOV, and technically the light sheet thickness will be more than 1.88 µm. When the NA of an objective is underfilled (beam usually cropped with apertures such as the vertical slit in our setup), the diameter in figure 1.11 becomes that of the aperture. This diameter can be taken as that of the 3x expanded beam (2.1 mm) since the vertical slit is made to only crops off the 'tails' of the gaussian laser light through its vertical opening. The angle θ becomes the inverse tangent of the ratio of the radius of the aperture to the working distance of the illumination objective. From trigonometry and equation 1.9, the new NA for the underfilled objective becomes ~ 0.06, and the light sheet thickness or axial resolution becomes ~ 4.07 µm. Thus, I kept the beam expansion to ~2.1 mm i.e., 3 times its original diameter using a combination of lenses with focal lengths of f_1 = 25 mm, and f_2 = 75 mm. To be specific, I had to change the f_2 lens in the $B.E_1$ of the original L-OpenSPIM design to a 75 mm. Lenses with the same focal lengths ($f_1 = f_2$ = 50 mm) were chosen for $B.E_2$ as the diameter of the beam entering it had been expanded to illuminate the BFP of the illumination objective to the required extent (i.e., the FOV of the detection), and further scaling of the light sheet height was not necessary.

2.2.2 Laser Combiner (LightHub-4)

Allows to include up to six (6) different laser wavelengths on the SPIM platform. It is a software-controlled module with a clean-up filter that can be incorporated into image acquisition protocols to rapidly select laser line(s) and excite different fluorophores simultaneously.

2.2.3 Heat Sink

I designed a heat sink specific for the laser combiner to regulate its temperature and that of its components, and to bring the exiting beam(s) to the required optical height above the breadboard.

2.2.4 30 mm Cage and Accessories

The 30 mm cage is used to mount the illumination objective, the $B.E_2$ optics, and to aid easy horizontal adjustment when defining the geometry of the light sheet and aligning it to the back focal plane of the objective. These include the CP11/M, CP09/M, EP8-P4, TR20/M-P5, and PH20/M-P5 (Thorlabs) (Figure 2.1).

2.2.5 Shearing interferometer (SI050, Thorlabs)

Useful for checking beam collimation at various stages in the assembly of the illumination axis. The shear plate ideally should be matched to the diameter of the expanded beam to observe the desired pattern (Figure 2.4).

2.2 Extensions - Detection Axis

2.3.0 Camera

I opted for the 16-bit sCMOS pco panda 4.2 monochrome camera as it has a compact design (does not take up much physical space) and is cost effective. With a 2048 x 2048 - 6.5 microns pixel size detector (13.3 mm), a quantum efficiency of up to 80 % for our targeted emission range (500 nm – 550 nm, 525 nm - peak), it is comparable in performance to other cameras such as the Hamamatsu ORCA-Flash4.0 LT, and the Andor Zyla 4.2 and 5.5 series. Though other high-end cameras such as the Andor Sona and Neo series are back illuminated and have a quantum efficiency of up to 95 % for a wider emission range and detection field, they are significantly (at least 3 times) more expensive. For a 16 bit camera, a good compromise between cost and desired features is the Andor Zyla 4.2.

2.3.1 Detection objective

An ideal detection objective suitable for different samples on our SPIM is one which is immersion and infinity corrected, has a relatively long working distance ($\geq$ 5 mm) to allow room for convenient large sample scanning, and a magnification and NA high enough to distinctively visualise smallest object details of interest. It is also important to consider the system magnification (i.e., net magnification of the detection objective along with that of optics along the z-axis) to ensure the entire object part in view is captured as much as possible and fitted within the available detector size of the camera.

As is in the case of the illumination, at the time of writing this text, objectives that meet these conditions are not readily available, are usually at most 10x – 12x magnification, and are significantly expensive, even though they do perform better when the right choice is used. On commercial systems, options adopted are to use the expensive (custom made) objectives, or a much cheaper one with a very low magnification (lesser than 4x) coupled with a zoom module which is usually not available to purchase as a separate unit. Even when available, they are sold parts of decommissioned microscopes and are worth tens of thousands of dollars. A cost-effective option for OpenSPIM builders is to use air objectives (as cheap as $500) with reasonable specifications, and image samples within a quartz or optical glass cuvette filled with a suitable imaging buffer (usually PBS or water for in-vivo studies and clearing solvent for in-vitro studies). There certainly are concerns with aberrations introduced into images acquired due to mismatched R.I between the detection objective, air, glass cuvette, imaging media and the sample itself. However, the use of air objectives and a cuvette is still a cost-effective option to build a basic platform that can achieve reasonable results while the builder (scientist) gain detailed knowledge and experience needed to advance into more complex and expensive platforms.

The 20x immersion detection objective suggested on the OpenSPIM website has a good NA - 0.5 and magnification. But it has a small working distance of 3.5 mm, is corrected for water immersion, and is not convenient for imaging through a cuvette nor for different imaging buffers. Here, the use of an air objective proves useful, and it is usually advised to stick to one with a minimal working distance. This ensures emitted fluorescence photons are captured as much as possible. The Nikon CFI Plan Apo Lambda 10x which has a 0.45NA, 4 mm WD, and a transmittance of over 80 % within the 450 nm to 1000 nm range is a good choice. The magnification of this objective can be further stepped down with a magnifier (such as the 0.5x magnifier used on the classic OpenSPIM design) when there is an absolute need to capture more parts of large intact samples in the FOV. On the other hand, to avoid reducing system magnification, samples larger than the FOV can be acquired by tiling each slice within a stack of images for each view (multitile-multiview imaging). This will yield more data and it is advised to keep each tile within a 4-gigabyte size (if using ImageJ for acquisition) to avoid data import problems when reconstructing the 3D image.

2.4 Air Objectives, Imaging Buffers, and Refractive Index (R.I) Matching

On the use of imaging buffers with air objectives, buffer solutions help to improve the refractive index matching of all media within the imaging space (from the front lens of the objectives to the sample), support physiological conditions for in-vivo imaging, and improve fluorescence collection without too much degradation of the image quality. The set-up also gives greater flexibility on the choice of imaging buffers and hardware. However, working distances of objectives are increased by a factor equal to the R.I of the imaging buffer used, and should be corrected for whenever there is a change in the buffer or objective(s). The goal is to ensure the focal plane of the detection is always be aligned to the waist of the light sheet without much labour. A solution is to mount the entire detection and the sample chamber (or imaging cuvette) on a translation stage (or adjustable optics). Additional components used in positioning and aligning the detection axis on our microscope are listed in Table 3.2. Some systems use an electrical tuneable lens (ETL) but will require using a scanned light sheet and still moving the detection into focus. It is important to note that aligning the light sheet waist to the focal plane of the detection is a skill which must be developed.

2.5 Other parts

2.5.0 Breadboard

A larger breadboard (750 mm x 750 mm x 12.7 mm) to accommodate more hardware modules planned for the current research and future optimisation.

2.5.1 Imaging cuvette

I used a 10 mm imaging glass cuvette to house imaging buffers and sample. The cuvette should be made of glass with a R.I matched to the imaging media. Quartz glass is preferred for imaging with PBS, sea water, and some clearing media such as CLARITY. Optical glass more suited for solvents with higher R.I.

2.5.2 Metal slab

Used to easily translate the cuvette along the illumination direction (x-axis), and to bring the imaging space to the required optical height above the breadboard (see Appendix. Figure A.1)

2.5.3 Workstation

I decided to purchase a high-end workstation to speed up post processing of data. Configuration details and performance are stated in the Table A.1 and Table A.2 respectively (Appendix section).

2.5.4 U-TLU/SM1S10 Aluminium Adapter

The U-TLU/SM1S10 Aluminium Adapter is useful for connecting the Olympus U-TLU tube lens to the SM1S10 (see Appendix, figure A. 2).

Parameter	Value
CW Laser	488 nm, 60 mW
Emission	525 nm
Single illumination (dry)	4x, 0.13
Single detection (dry)	10x, 0.45
Tube lens (Olympus)	f = 180 mm
Beam diameter expansion	0.7 to 2.1 mm
System Magnification	9x, 4.5x
Field of View (FOV)	~1.48 mm, 2.96 mm
Pixel resolution	0.72 µm, 1.44 µm
Axial extent (FWHM)	~47 µm
Axial resolution/ LISH thickness (FWHM)	~1.88 µm*
Lateral resolution (FWHM)	~0.58 µm

Table 2.0: Summary of system properties. * The light sheet thickness of 1.88 µm assumes the full NA of the illumination objective is used. Underfilling the objective will increase the light sheet thickness and more beneficial for thicker samples ($\geq$ 1 mm)

2.6 Microscope Control and Data file format

I set up the open-source micro-manager 2.0 gamma software for hardware control and acquisition rather than using the newly published µ-openspim (Girstmair *et al.*, 2022b) plugin in Fiji. A key advantage of the Micro-manager 2.0 gamma over the µ-openspim is the Multi-Dimensional Acquisition (MDA) tile acquisition functionality which is very useful to acquire images that are bigger than the FOV without compromising system magnification. Micro-manager 2.0 gamma can be downloaded from Micro-Manager, (2021) at the time of writing this text. However, a downside to using the MDA is that each tile (or non-tiled stacks) is advised to be kept below the size of 4-gigabytes and each view saved as a ome.tif stack file format. A stack greater than 4-gigabytes is written into different stack files (rather than a single file) and saving the acquired data in single plane TIFF file format could be ‘messy’. Either case pose a challenge when importing the data into the Multiview or BigStitcher reconstruction software in Fiji before resaving in a more robust HDF5 or N5 format.

A way to resolve the 4-gigabyte limit problem is to invest in developing an acquisition software as done by Girstmair *et al.* (2022). Better still, the software should be capable of tile acquisitions and saving acquired data real-time in formats such as HDF5 or N5 that allow writing larger stacks as a single file. The N5 format particularly improves speed by saving data in parallel.

2.7 3D Reconstruction

Post processing of acquired data can be done using the multi-view reconstruction (MVR) plugin in Fiji. This provides the bead-based registration, content based multi-view fusion, and multi-view deconvolution algorithms essential for reconstructing SPIM data. Icha *et al.*, (2016) provides stepwise details (including videos) on this, in addition to the stepwise instructions published on the OpenSPIM website on registering and fusing 3D data (Pitrone *et al.*, 2013k)

A more robust platform for reconstructing tiled data is the BigStitcher plugin on Fiji (Hörl *et al.*, 2018). This houses MVR capabilities, but in addition can handle terabytes sized multitiled multiview timelapse data which need to be stitched before registration and fusion. It further offers various algorithms options to achieving a finer registration. Both MVR and BigStitcher employ the BigDataViewer plugin for visualising data (Pietzsch *et al.*, 2015).

Furthermore, the 3D registration and fusion can be done either on the Central Processing Unit (CPU) or the Graphics Processing Unit (GPU) of a personal computer (PC) with specification that can complete data processing in a reasonable time. A decent configuration is advised on the OpenSPIM webpage (Pitrone *et al.*, 2013d). In contrast to CPU processing, the GPU card requires dynamic link libraries (DLLs) which in most cases must be compiled uniquely as they are built based on the PC's architecture. At the time of writing this text, details on developing the required libraries are hosted on the GitHub web pages (Preibisch, 2015a, 2015b). The expertise of a computer scientist will most likely be needed to eliminate bottle necks in the build process. Nonetheless, the computation speed provided is worth the effort invested.

2.8 Assembly

I built an OpenSPIM based off the L-OpenSPIM design on (Pitrone *et al.*, 2013b) with single illumination and detection arms at 50 mm optical height above a 750 mm x 750 mm x 12.7 mm aluminium M6 Tap breadboard. Thus, I frequently refer to relevant webpages on the OpenSPIM website. An understanding the basics of optics is also recommended and described on the OpenSPIM website (Pitrone *et al.*, 2013l).

Step 1: Coupling parts I adopted from the OpenSPIM design in preparation to mount them on the breadboard. This includes installing the achromatic doublets (AC127-075-A-ML, AC127-025-A-ML) for the beam expander 1 on their lens mounts and the RC1 rail carriers; mounting the two alignment disks (DG05-1500-H1-MD) on RC1 rail carriers; mounting the cylindrical lens (ACY254-050-A) on the index rotation on a RC1 rail carrier; mounting the corner mirror on the Polaris-K1 and then on to a RC1; and mounting the vertical slit (VA100/M) on the RC1. Steps followed are stated on the OpenSPIM website (Pitrone *et al.*, 2013f, 2013c).

It should be noted that the dimensions of the vertical stilt used for the beam bouncing mirrors on the OpenSPIM website is adopted as that of the stilt for the corner mirror in our case.

Step 2: Coupling illumination extensions used on our platform

i. The beam expander 2 optics (AC127-050-A-ML, AC127-050-A-ML, Thorlabs), the illumination objective (N4X-PF, Nikon), two M6 tap washer, and the 30 mm cage system mounts (CP11/M, CP09/M, EP8-P4, TR20/M-P5, CP02B, Thorlabs).

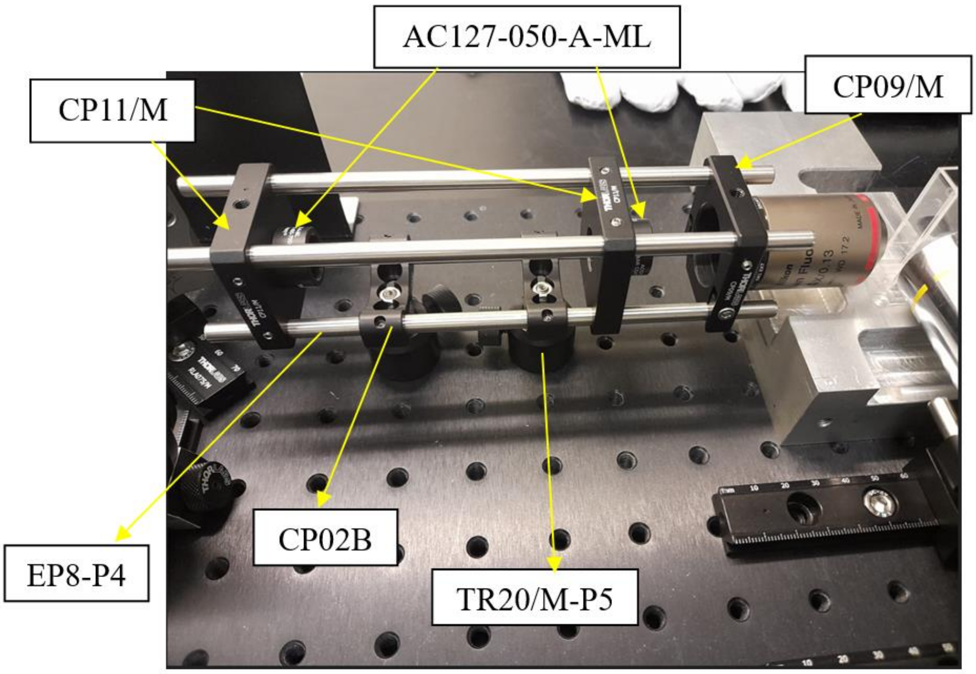

Figure 2.1: Beam Expander 2 achromatic doublets and the illumination objective mounted on the 30 mm cage system from Thorlabs. The SM1A12 (not shown) is used to mount the objective on the CP09/M

ii. Shearing interferometer and a RC1 (SI050, Thorlabs)

The interferometer is mounted on a RC1 rail carrier with the aid of a vertical stilt of dimensions same as that used for the B.E_1 lenses in step 1 (see Figure 2.4).

Step 3: Coupling detection extensions used on our platform

i. The detection objective (MRD00105, Nikon) and emission filter mounts (CP09/M, EP4, CP02B SM1A12, SM1V15, CP09/M, SM1L05, SM1S10, Thorlabs), and the U-TLU/SM1S10 aluminium adapter (See Figure 3.2). The SM1L05 is used to mount the fluorescence emission filter and can be replaced with a filter wheel to accommodate filters of different band pass without the need to dissemble the unit each time a different filter needs to be used. The SM1V15 particularly aids fine adjustment of the position of the detection objective in the z-direction to align the focal plane to the beam waist and is very useful when there is a need to change objectives or imaging buffer. The entire cage system is mounted on two RC1 rails carriers using vertical stilts of 9.7 mm height and M4 tap holes.

ii. Detection axis holder (modified), U-TLU, U-TV1X-2, and Camera:

Coupling the detection axis holder, U-TLU, U-TV1X-2, and the Camera is as stated on OpenSPIM website (Pitrone *et al.*, 2013g), with some modifications (See Figure 3.2). Clearances are made on the bottom part of the detection axis holder to include two RC1 rail carriers that aid adjusting the detection in the illumination direction whenever the need arises, while keeping the optics at the required optical height (50 mm) above the breadboard. M6 tap screws are used to fasten the rail carriers through a M6 screw threading made on the holder.

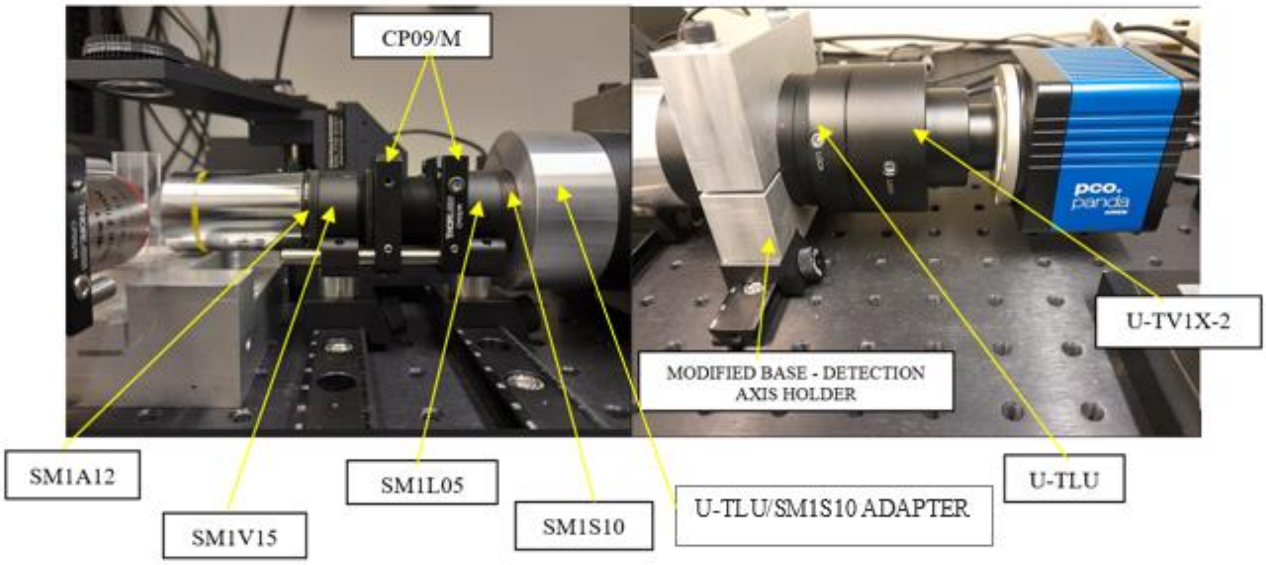

Figure 2.2: Detection optics on the 30 mm cage system and RC1 rail carriers. The SM1S10 is connected to the U-TLU tube lens using the U-TLU/SM1S10 aluminium adapter.

Step 4: Setting up the breadboard on an optical table to limit effects from physical vibrations. **Step 5**: Bolting a RLA300/MM to the breadboard in preparation to mount optical components. **Step 6**: Installing the heat sink and the LightHub laser combiner on the breadboard and securing both with M6 tap screws such that an imaginary vertical plane that equally splits the beam aperture on the LightHub aligns with that through the RLA300/MM mounted in Step 5. **Step 7**: Installation of a RLA75/MM for the corner mirror, two pieces of the RLA300/M for the metal slab and USB 4D-stage, and three pieces of the RLA150/MM to mount the detection axis. **Step 8**: Installation of the corner mirror on the 75mm dovetail optical rail (RLA75/MM); the PH20/M-P5 on the breadboard; the 30mm cage system (already coupled with the beam expander 2 optics and illumination objective) on the PH20/M-P5; the beam expander 1; the vertical slit; and the cylindrical lens optics on the RLA300/MM. **Step 9**: * Installation of the coupled detection axis on the RLA150/MM, the metal slab on the RLA300/MM, and the USD 4D stage. **Step 10**: Installing hardware cables and the micromanager software on the acquisition computer, configuration of software with hardware and testing using the hardware configuration wizard on micromanager. A detailed description of this and how the Multi-Dimensional Acquisition tool can be used for image acquisition are described on the micromanager wiki (Micro-Manager, 2012).

*The detection axis must be positioned such that the front lens of the detection objective is at its working distance away from an imaginary symmetric vertical plane splitting the front lens of the illumination objective. The CP09/M and SM1V15 on the coupled detection can be adjusted to achieve this (fig 3.2). The distance between the back focal plane of the detection objective and the front lens of the olympus U-TLU tube lens (useful for inserting filters, splitters etc) is recommended to be in the range 50 mm – 170 mm. The shorter, the better. Before bolting the metal slab to the breadboard, it should be positioned (with the glass cuvette) by moving it in the illumination direction to ensure the front lens of the detection objective is roughly centred in the middle of the cuvette window closest to it (see fig 3.0).

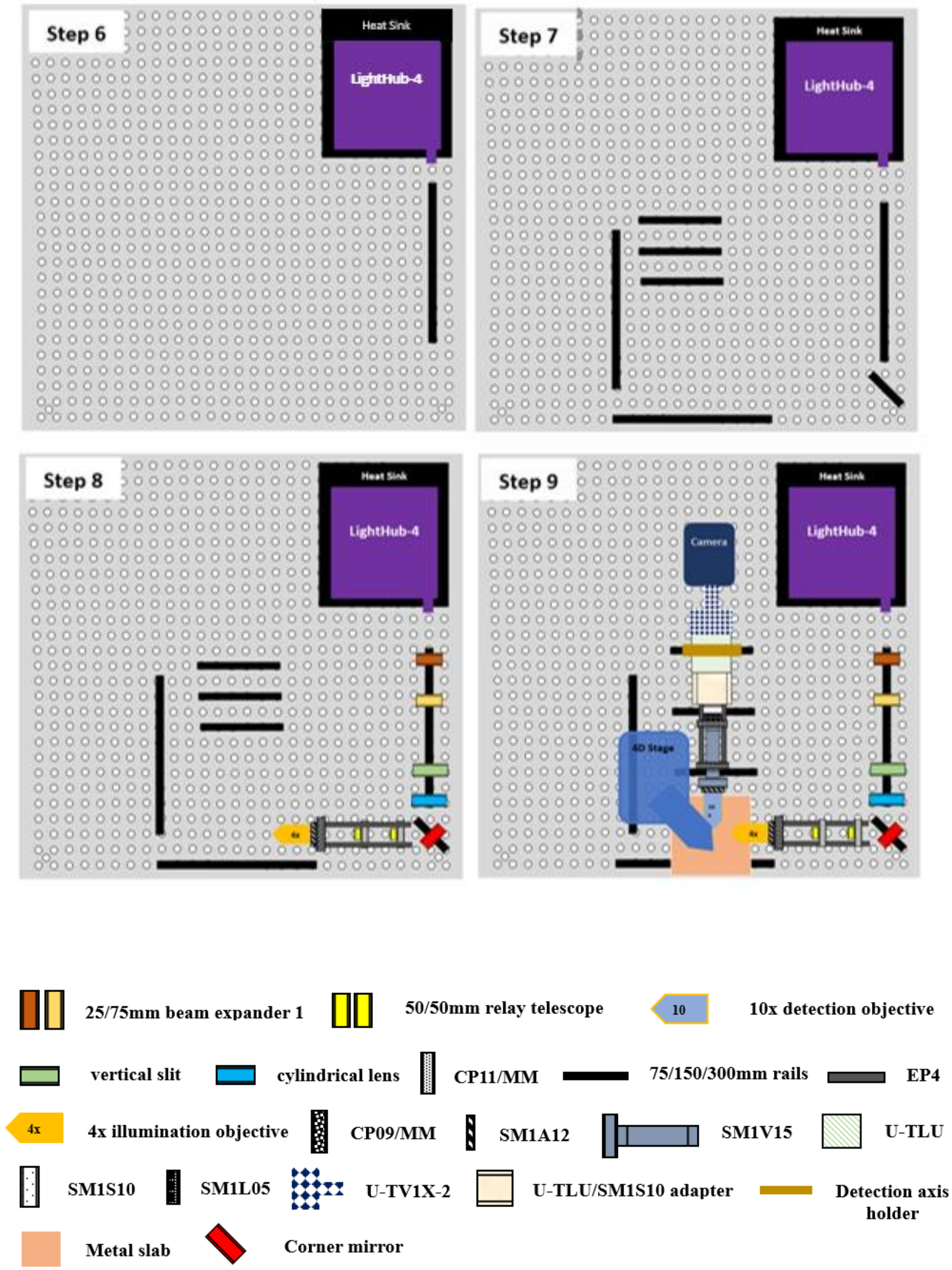

Figure 2.3: Schematic assembly of our SPIM parts following instructions from step 6 to 9.

2.9 Light Sheet Formation and Alignment

Laser safety training and the use of laser safety glasses with a suitable optical density is critical and highly recommended for beam and light sheet alignment. Useful information on beam and light sheet alignment can be found on the OpenSPIM website (Girstmair *et al.*, 2022a). I however provide more practical insight.

2.9.0 Beam Alignment

A rough alignment of the laser beam is done without the refractive optics of the illumination and the emission filter in place. The vertical slit is opened to its full width and using the alignment disks I ensure the beam is at all points parallel to the breadboard and bounces off the centre of the corner mirror. The same process is then repeated with the illumination optics reinstalled.

Step 1: First, the optics of the beam expander 1 are removed from the RLA300/MM and the two alignment disks (DG05-1500-H1-MD) already mounted on RC1s are placed at each end of the RLA300/MM closest to the LightHub and tightened. The LightHub is slightly loosened and using a low laser power, it is adjusted till the beam passes through both apertures on the disks. The LightHub is then tightened to the breadboard again. This step is easier done by keeping the LightHub in a 90^0 position (anticlockwise to its position shown in step 6 - figure 2.3), and an additional mirror is used to deflect the exiting beam 90^0 degrees onto the corner mirror.

Step 2: Replace the achromatic doublets (AC127-050-A-ML) on both CP11/M with the alignment disks (DG05-1500-H1-MD), ensuring the centre of the disks are about 50 mm and

150 mm from the corner mirror. Using the corner mirror, align the beam ensuring it also goes through the aperture on both discs. Remove the disks and re-install the achromatic doublets (AC127-050-A-ML)

Step 3: Re-mount the refractive optics for the beam expander 1, such that the AC127-025-A-ML is placed close to the end of the RLA300/MM (i.e., closer to the LightHub) and its distance from the AC127-075-A-ML is approximately 100 mm (i.e., the sum of their focal lengths). Ensure the beam passes through the middle of both refractive optics. At this point, the beam exiting the AC127-075-A-ML should be collimated. Collimation can be checked using the shearing interferometer mounted in front of the AC127-075-A-ML doublet and adjusting the position of the AC127-075-A-ML if necessary. It is also useful at this point to place an alignment disk at the end of the RLA300/MM (close to the corner mirror) to ensure the beam is still centred around its aperture and parallel to the breadboard.

The use of the corner mirror in positioning the beam is described on the OpenSPIM website (Pitrone *et al.*, 2013m)

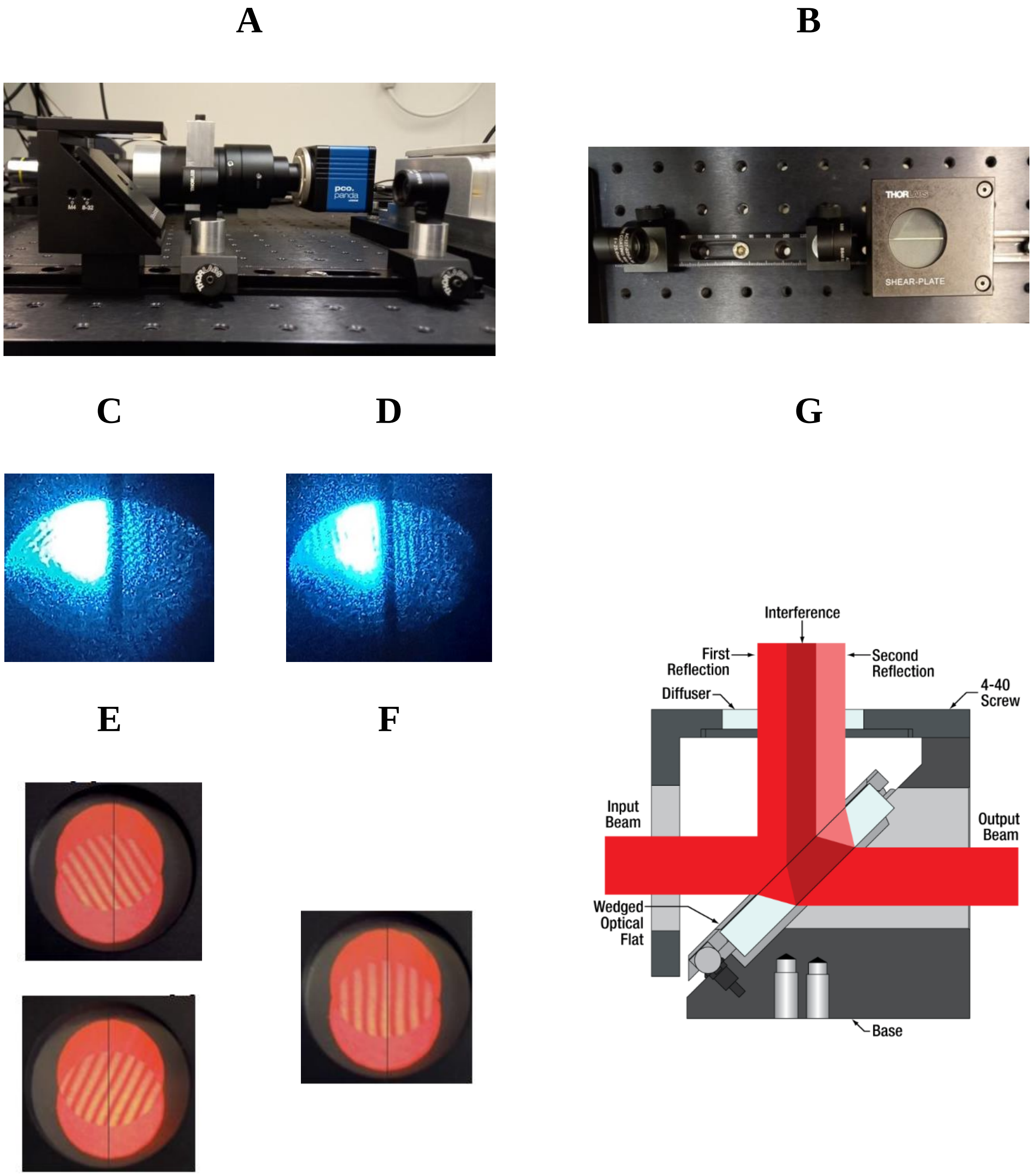

Figure 2.4: Shear plate interferometer mounted on a RC1 rail carrier side view (A) and top view (B). At least 3 mW power is needed when examining collimation. It might be difficult to observe the interference pattern from the top view if the shear plate chosen does not match the diameter of the expanded beam. The shear plate I had is designed for 2.5 - 5.0 mm diameter beams which is not an ideal fit for our expanded beam (2.1 mm). Thus, I do observe a non-collimated (C) and collimated (D) beam pattern which is not as clear as it should be in (E) and (F) respectively. A schematic of the beam path through the interferometer (G). E, F, G are adapted from (Thorlabs, 2022) under the terms of the Creative Commons Attribution License (CC BY).

2.9.1 Light Sheet Formation

Step 1: I follow the steps stated on the OpenSPIM website (Pitrone *et al.*, 2013h). Particularly, I install the cylindrical lens (ACY254-050-A) which has been mounted on the index rotation (RSP1X15/M) on the RLA300/MM with the aid of a RC1 at about 50 mm to the corner mirror. Its distance to the mirror is then adjusted until the thinnest beam line can be seen on the mirror. The vertical slit is placed at 50 mm behind the cylindrical lens (in the illumination direction). The lenses of the beam expander 2 (AC127-050-A-ML) (which is a relay telescope) are placed at 50 mm and 150 mm from the corner mirror (by adjusting the CP11/M and using a ruler), and the lens at the 150 mm mark should be at its focal distance away from the BFP of the illumination objective. I can confirm this by removing both the lens closer to the corner mirror and the cylindrical lens (marking its position on the RLA300/MM dovetail rail), mounting the shear plate interferometer at the front lens of the illumination objective, and slightly adjusting the CP09/M objective mount until the beam exiting the front lens of the objective is collimated. The cylindrical lens and the AC127-050-A-ML doublet are then placed again into the marked positions. The light sheet should now be formed on the side of the front lens of the objective with its waist at the focal length of the objective (without mounting the buffer filled glass cuvette).

2.9.2 Light Sheet Rough Alignment

First, I position the detection axis such that an imaginary symmetric vertical plane that splits the front lens of the detection objective is apart from the front lens of the illumination objective by the magnitude of its working distance (of the illumination objective). Next, I mount the sample cuvette filled with the required imaging buffer in its position on the metal slab. Since air objectives are used in imaging in the buffer, the focal plane for both the illumination and detection are both displaced and need to be accounted for. In our case, the slab can be translated in the illumination direction by a displacement factor which is a function of the refractive index of the buffer and the length portion of the working distance of the illumination objective within the cuvette (when filled with no solvent) (see figure 2.5). The entire detection is adjusted in a similar manner i.e., first in the illumination direction by the same displacement factor, and then the detection objective is technically made to translate in the negative z-direction by the same magnitude. The detection objective and imaging cuvette or sample chamber can be mounted on 3D translation stages to make these adjustments easier.

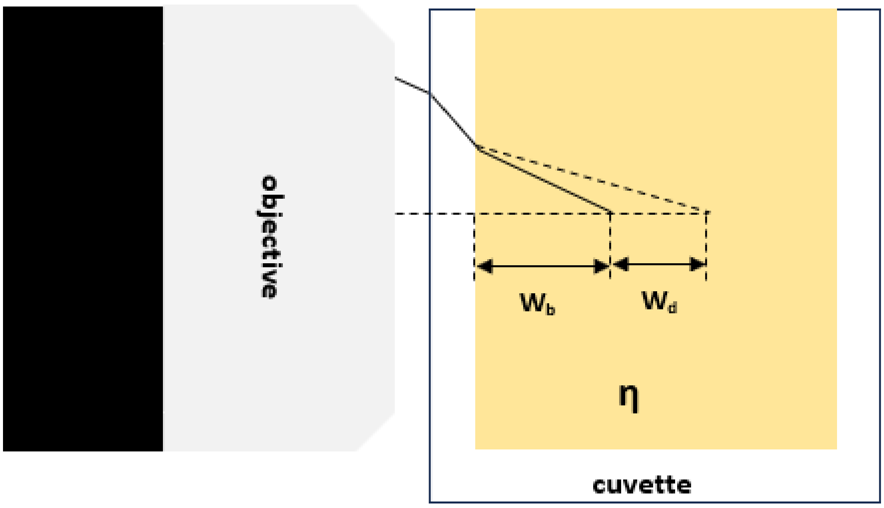

Figure 2.5: Schematic of the shift in the waist of the light sheet and the focal plane of the detection. The portion of the focal length of the objective(s) within the cuvette when empty $\mathbf{W_b}$ is displaced by a factor $\mathbf{W_d}$ when filled with a buffer of refractive index $\boldsymbol{\eta}$. Thus, the focal plane of the detection lens and the waist of the light sheet must be adjusted in the negative Z and illumination direction by the displacement factor $\mathbf{W_d}$, respectively. $\mathbf{W_d} = [\boldsymbol{\eta} \times \mathbf{W_b}] - \mathbf{W_b}$

A reflective optical grid (58-607, Edmund Optics) (which ideally needs to be broken up before use) is mounted on the 4D-stage and brought to the focus of the detection using bright field illumination from a lamp (PSX501, Thorlabs). It is then tilted 45^0 in the light sheet direction and slightly translated in the +Z or -Z direction until all points on an imaginary vertical line along the middle of the grid is in focus. At this point, it is quite useful to initially rotate the light sheet to a horizontal position (with the aid of the index rotation that mounts the cylindrical lens), bring it to the middle of the field of view using the corner mirror, and then rotate the light sheet back to align to the vertical. The OpenSPIM website describes the use of the corner mirror in translating the light sheet (Pitrone *et al.*, 2013m).

The corner mirror is further used to align the position of the waist of the light sheet to the imaginary vertical line on the grid which is in focus. A cheaper alternative to the grid is to use a small piece of plane mirror stained with fingerprints or any matter that will barely absorb the laser light (dirty mirror), the fingerprints being used as the feature to focus on. Sweeping the 45^0 grid or dirty mirror along the illumination direction, I can examine the profile of the light sheet across the field of view. This is done at different width opening of the vertical slit until a sheet of least diffraction is observed in moving between the two ends of the field of view. OpenSPIM web pages that capture useful information and videos on this (Pitrone *et al.*, 2013i, 2013j).

2.9.3 - Finer Light Sheet Alignment

Two common techniques to further fine tune the light sheet alignment to the focal plane of the detection include the use of fluorescent beads evenly dispersed within a column of agarose, and the use of a fluorescent solvent with a refractive index approximately the same as the imaging buffer intended to be used. The former is more useful when water, PBS, or solvents that would not dissolve the agarose column (or destroy the suspended beads) is used as imaging buffer, and the latter is an alternative when beads cannot be used (figure 2.7).

The section on sample preparation in this text describes in detail the bead preparation process for light sheet alignment. However, during alignment, the basic idea is first to bring the centre of the agarose column into focus on the live view of the camera, and then illuminate beads within the agarose plane in focus by adjusting the light sheet position (using the corner mirror) until the sharpest images of the fluorescing beads within the plane is observed (bearing in mind the image will degrade as I image into the agarose along the illumination direction). I further fine-tuned the alignment of our SPIM using this method.

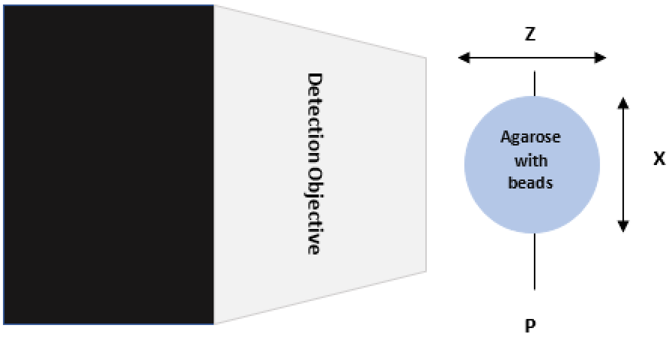

Figure 2.6: Schematic posterior view of a cylindrical shaped agarose protruding from a capillary. Locating the centre of the agarose requires translating it along the X direction, and then the Z direction to work out its diameter along these directions. It is critical to ensure the mid-point of the X plane is achieved before that of the Z. The X and Z coordinates reported on the user interface of the translation stage are useful in calculating these. The focal plane of the detection is then brought to the half position of these diameter lengths, which will technically align it (and ideally the light sheet) to the plane P along the centre of the agarose.

On the other hand, the cuvette or sample chamber can be filled with a fluorescing solution of suitable refractive index, and the light sheet passing through it is clearly visible on the live view of the camera. The light sheet position can then be adjusted until it becomes brightest and uniform across the field of view.

The profile of the light sheet can be re-examined after this step using a plane mirror or an optical grid at 45^0 swept through the field of view as stated earlier. It is important at this point to calibrate the sampling (image) pixel size on micromanager. In general, the sampling pixel size is the ratio of the pixel size of the camera to the magnification of the detection. Ideally, I want the sampling pixel to be at least half the resolution of the detection (lateral resolution), but this can be limited by hardware capabilities such as the pixel size of the camera and the need to stick to available optics needed along the detection (Pitrone *et al.*, 2013e).

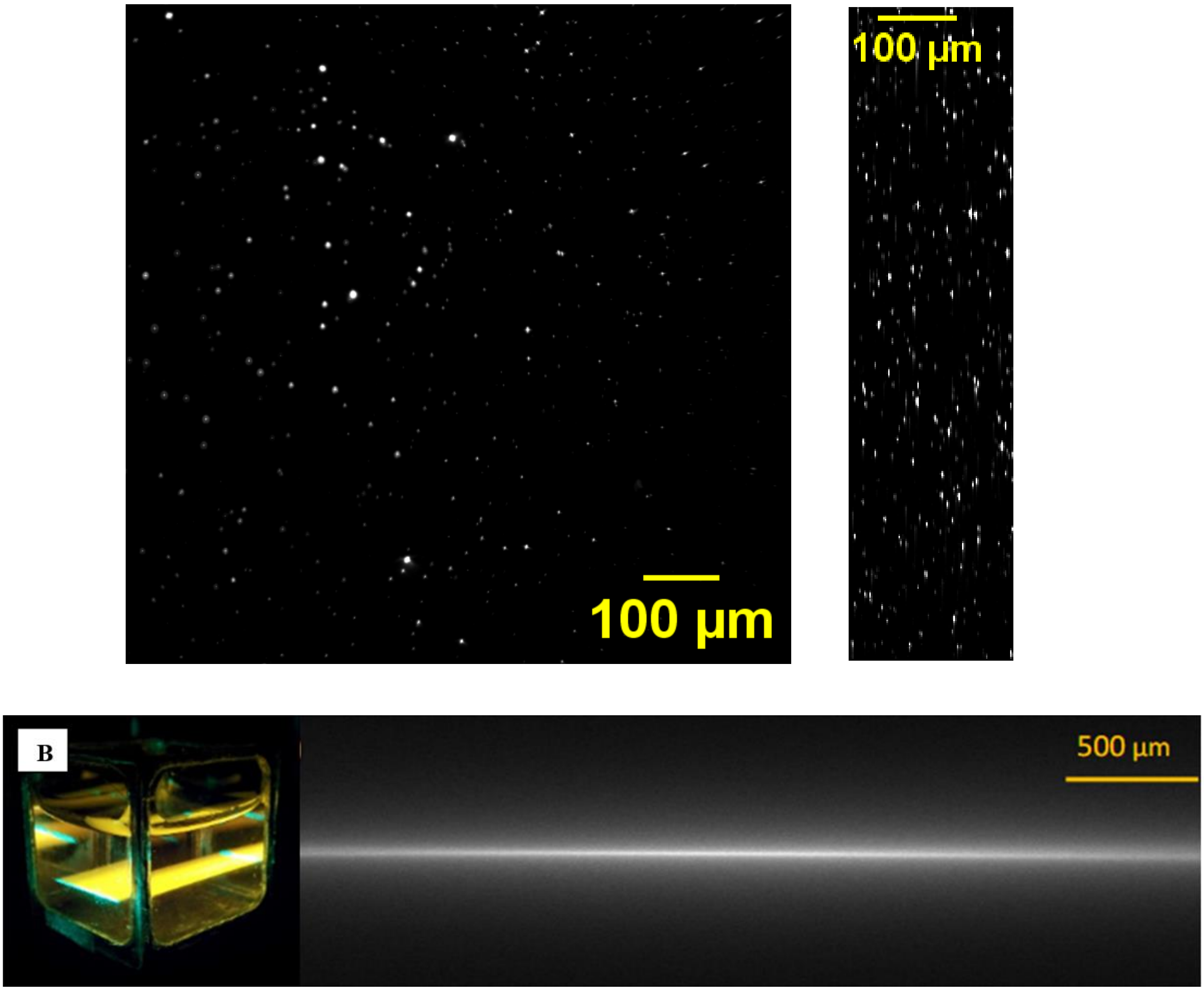

Figure 2.7: Bead images for light sheet alignment (A) (XY – left, YZ - right). Fluorescent solvent (fluorescein solution) (B) used for alignment in BABB. Image B is adapted from Figure 32 in Montalbán, A., Andilla, J., Artigas, D., & Loza-Alvarez, P. (2015). Design, Implementation and Test of a Routine Light Sheet Fluorescence Microscope, p. 34, under up commons license, https://upcommons.upc.edu/bitstream/handle/2117/77129/LSFM_FINAL_Adrià.pdf?sequence=9

2.10 Sample preparation and mounting

2.10.0 Fluorescent Beads

In addition to using fluorescent beads for light sheet alignment, they are also important for characterising the PSF of a light sheet microscope. The beads are prepared to be evenly dispersed within a column of agarose (~ 1 % agar concentration), and its concentration within the agarose should depend on its purpose for use. As a rule of thumb, lower bead concentrations are required for light sheet alignment to aid better contrast (Bishop, Glaser and Liu, 2020). When used as fiducial markers to aid post-acquisition registration of the acquired image stacks, a higher concentration is required than that used for aligning the light sheet. Submicron beads are also preferred for alignment to avoid significant scattering and lens effects.

Step 1: For our 10x detection, 2% low melt agarose gel (Fisher BP165-25) is prepared from a heated mixture of agar and distilled water. **Step 2**: 13 µl of the original bead solution (Estapor F-Y-050 (1 %), 0.520 µm ± 0.037 µm) is put in 14 ml of distilled water. **Step 3**: 1000 µl of the output is further mixed with 3.91 µl (or 31.25 µl when used as a fiducial marker) of the original bead solution i.e., with volumes that gave the best dispersion and concentration required in the final agarose-beads mixture (1000 - 2000 beads per image plane) as observed on a confocal microscope. **Step 4**: 0.25 ml of the 2 % low melt agarose cooled to about 40°C is mixed with an equal volume of the final output of step 3 and vortexed gently within an eppendorf tube. The product of each of the steps described above needs to be well vortexed to ensure even dispersion of the beads. The final mixture is then drawn into an appropriately sized capillary using its plunger (that ensures the agarose can sufficiently cover the field of view of the microscope), along with the sample to be imaged where needed. The capillary is then rotated in a circular direction about its long axis for at least 2 minutes (to keep the beads evenly dispersed while the agarose solidifies). An additional step for alignment in a refractive index matching solution (RIMs) used in sample clearing (in cases where beads can be used) is to suspend a good portion of the agarose-bead protruding from the capillary in the RIMs until the agarose appears ‘optically matched’ to the RIMs (i.e., until the RIMs replace water in the agarose gel, thus reducing the refractive index mismatch).

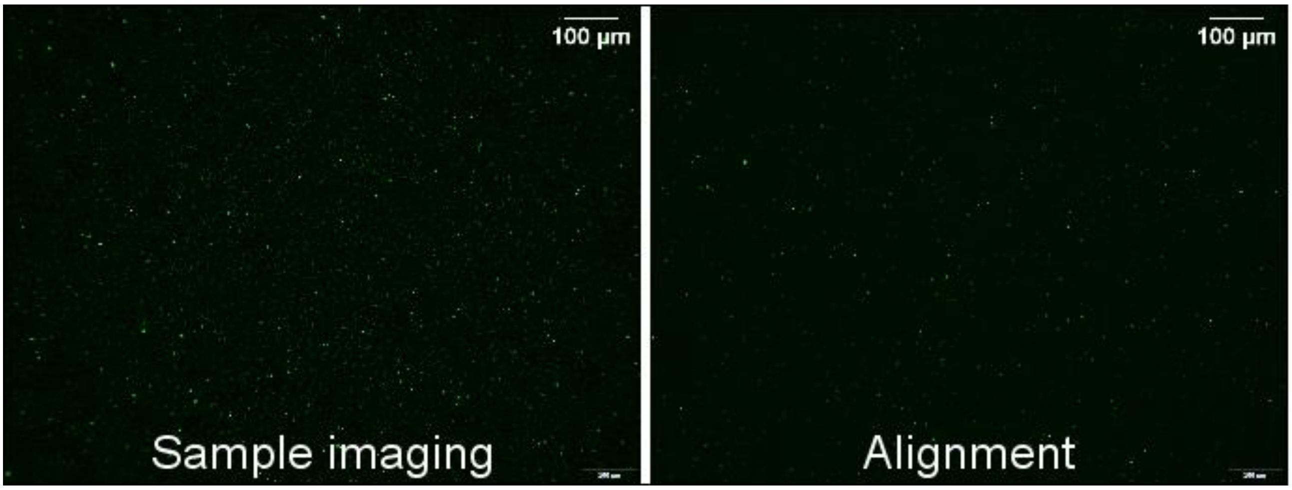

Figure 2.8: Images of beads in agarose for SPIM alignment and sample imaging (scalebar: 200 μm). Put on a glass slide and examined on a confocal microscope (10x magnification, 488 nm excitation) to examine how evenly dispersed the beads are. It is important that this is done to validate the beads-agarose preparation protocol every time there is a change in the imaging setup.

2.10.1 – *Hydractinia symbiolongicarpus*

The head of a *Hydractinia symbiolongicarpus* was excised from its body and immobilised in a 1 % agarose made from sea water (28 ppm – 32 ppm) by mounting on a capillary (Brand 10μl – 701902) with a piston rod (Brand – 701930), and then imaged in sea water with the same salinity as the agarose.

2.10.2 – *Varroa destructor*

A *Varroa destructor* was embedded in 1 % agarose with beads and mounted on a capillary (Brand 100µl - 701910) with a plunger (Brand piston rod - 701936). The sample was imaged in distilled water.

2.10.3 - Image Acquisition parameters

Endogenous Green Fluorescent Protein (GFP) was imaged in all tissues with 488 nm excitation within a 10 mm quartz glass cuvette. Sea water (28 ppm – 32 ppm) was used as buffer for *Hydractinia symbiolongicarpus* and distilled water for *Varroa destructor*. I also imaged fluorescent beads for optical alignment. Sampling was done at 0.72 µm pixel size and a 500 nm long pass filter (Semrock, BLP01-488R-25) was used to suppress unwanted fluorescence signals. Image acquisition was done using the multi-dimensional acquisition (MDA) tool available on micro-manager 2.0 gamma edition. Acquisitions can gain speed from the camera pixel binning (i.e., recording the averaged value of a subset of pixels as a single pixel) when set to 4 X 4 (which groups 16 pixels as one) to produce a 512 x 512 final image but at the cost of spatial resolution. However, since our aim focuses more on the ability of the microscope to spatially resolve features of interest, binning was set to 1 x 1, to create a 2048 x 2048 single sized images. The position-list plugin in the MDA was used to define different 3D coordinates for each Z-stack. Table 2.0 shows a summary of acquisition details with each image stack or tile kept below 4-gigabyte and saved in the ome.tif file format.

S/N	Sample	Laser Power	Camera Exposure	Step Size
1	Fluorescent beads	*24 mW	*300 mS – 400 mS	1.5 μm
2	*Hydractinia symbiolongicarpus*	6 mW – 7 mW	80 mS – 100 mS	1 μm
3	*Varroa destructor*	12 mW	40 mS	6 μm

Table 2.1: Acquisition parameters.

*It is important to note that a longer exposure time and higher laser power may be needed to visualise beads in a RIM solution that are compatible with clearing solvents. This is probably because the intensity of fluorescing beads might have degraded over the period the agarose was optically matched to the RIMs. Values shown are for beads imaged in a RIM solution optimised for imaging in CLARITY clearing media.

2.11 PSF Estimation

Fluorescent beads act as point sources and can be analysed (size and shape) to estimate the point spread function (PSF) of the system. When sufficiently small, they can be used as an index of its resolution performance. Using the appropriate buffer, I imaged a stack of submicron beads (Estapor F-Y-050 (1%), 0.520 μm ± 0.037 μm) prepared as described in 2.10.0.

Figure 2.9 shows PSF images of a bead pictured in sea water (28 ppm – 32 ppm) for *Hydractinia symbiolongicarpus*. The size of the PSF measured experimentally in the X-Y and Y-Z directions are 4.32 μm and 2.88 μm respectively. This value for the lateral resolution significantly differs from the theoretical estimate (0.58 μm). This can be attributed to spherical aberrations from the use of air optics to image through media of different R.Is. i.e., the change in index of refraction that occurs at the chamber (i.e., buffer to glass to air), the objective, or the tube lens. To give a rough idea of how much details the current platform can spatially resolve to, the diameter of neurites (projections from the soma – cell body of neurons) in a mouse spinal cord should range between 0.1 μm and 6 μm (Fiala and Harris, 1999; Saliani *et al.*, 2017). Additional hardware modules and technicalities can be introduced to improve the resolution of the platform and are stated in section 3.8. However, in our case, I aim to stick to assembled parts within our curent available budget and improve the quality of results post-acquisition with reconstruction methods. Information on the PSF can be applied in the deconvolution process to produce images of a higher quality.

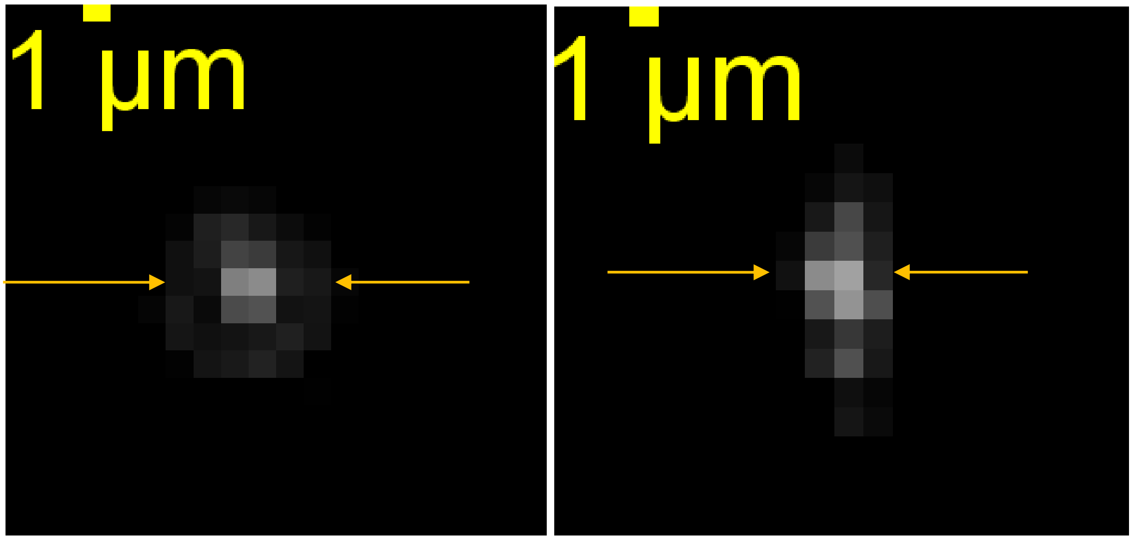

Figure 2.9: PSF images in the XY (left) and YZ (right) planes of a single bead. Spherical aberration is evident as I use uncorrected air objectives for imaging through a cuvette, sea water (28 ppm – 32 ppm), and agarose each having different R.I. Counting one line of pixels in the horizontal direction from left to right (pixels between the arrows) gives 6 pixels and 4 pixels in the XY and YZ planes respectively. Multiplying these number of pixels by the sampling pixel size (0.72 μm) gives the lateral and axial resolution (PSF) extent experimentally as 4.32 μm and 2.88 μm respectively.

2.12 3D Image Reconstruction

Registration algorithms provided for openSPIM models hinge on using beads rather than sample features as fiducial markers. However, not all in-vivo imaging can be done with fluorescent beads. For example, a Hydra sample is highly motile and do not survive for long outside sea water (28 ppm – 32 ppm). Registration and fusion (and/or deconvolution) of several views of such samples will require using sample features and need good PSF extraction for deconvolution. For 3D reconstruction without beads, the help of a computational scientist if often needed to develop in-house algorithms. Ideas can be sort from online microscopy communities such as image.sc forum. However, BigStitcher bundles four registration algorithms; phase correlation, Lucas-Kanade gradient descent, intensity based, interest-point based, which should be tried before considering other options. For this very reason DIY platforms should ultimately seek to adopt a design that produce raw quality isotropic images such as in the mesoSPIM initiative (Voigt *et al.*, 2020).

To demonstrate 3D reconstruction capability using beads, I applied relevant algorithms to 2 views of *Varroa destructor*. Flatfield correction and intensity thresholding was done. The raw data were then imported into BigStitcher using the autoloader loci bio-formats*. Data was then resaved as HDF5 or N5. All data were registered to a fixed view manually, and then the fast descriptor-based rotation-invariant algorithm was used to register detected interest points. Registration success was judged by achieving a high number of true correspondences (RANSAC) between each view and every other stack within the data, in addition to visual inspection. A further Iterative Closest Point (ICP) refinement was done where needed. Several iterations were then performed to fuse and deconvolve (deblur) the registered stacks to produce 3D images. Table A. 2 (appendix) references the amount of time required for the CPU and GPU to reconstruct 2 views of our 3D data.

*For tiled acquisition data, manual loading option might be preferred for importing tiled data as it gives greater flexibility in defining required file parameters and filename patterns. This is usually followed by stitching the tiles i.e., aligning with phase correlation method (two-round global optimization), and then secondarily by an Iterative Closest Point (ICP) refinement of the affine transformation.

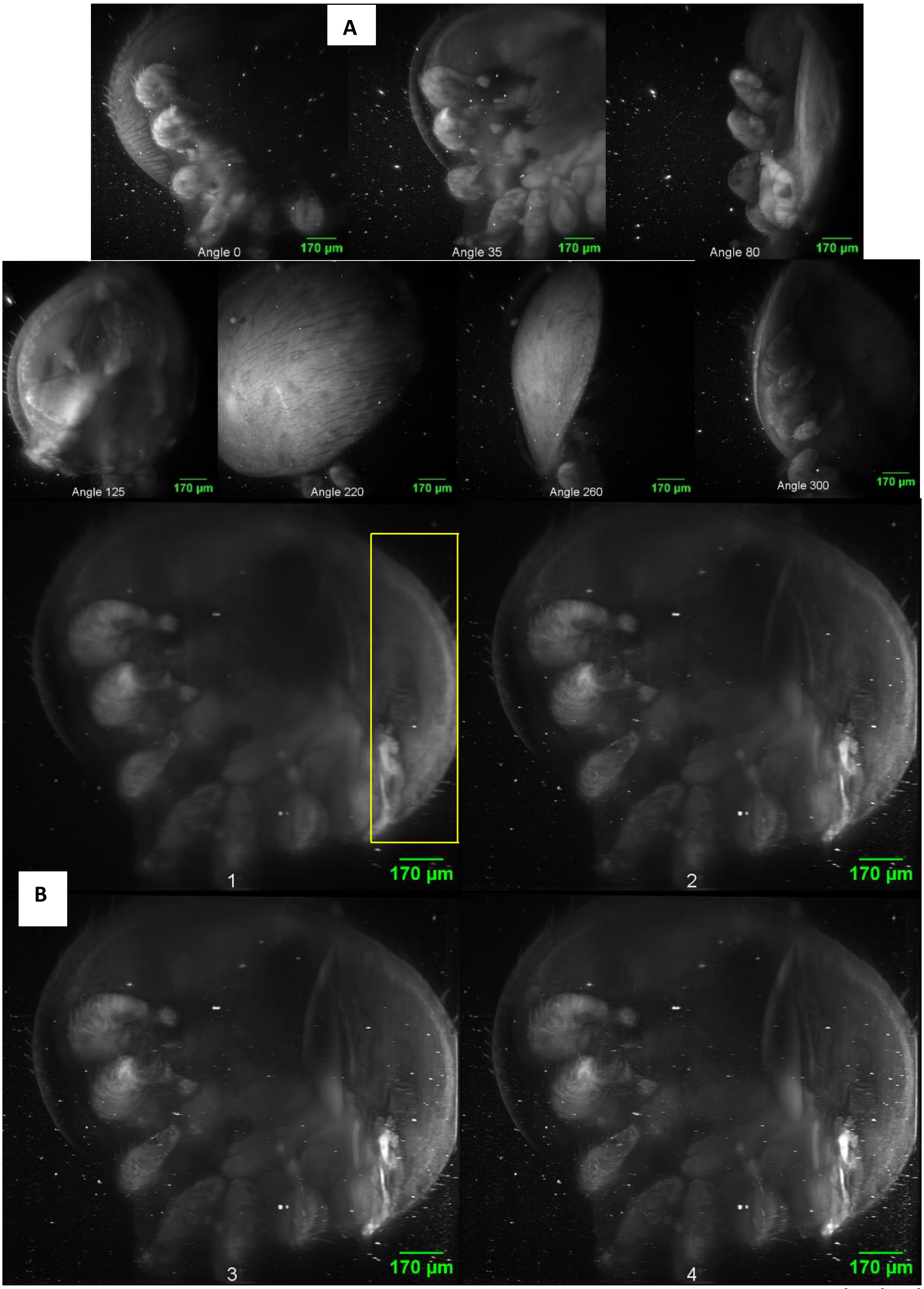

Figure 2.10: Maximum projection of raw fluorescent images of seven views of a *Varroa destructor.* (A - 0^0, 35^0, 80^0, 125^0, 220^0, 260^0, and 300^0). 2 views (35^0 and 80^0) were fused and deconvolved. Deconvolution of the fused view shows increased deblurring of the image with increasing iterations 5, 10, 15, and 20 (i.e., 1, 2, 3, and 4 respectively). Comparing the fused and deconvolved view (B) with the individual view 35^0 shows the fused view captures more image parts (marked with yellow box) not seen in the single view. Same applies when comparing with the 80^0 view. Fusing more than two view coupled with increased deconvolution iterations could possibly yield better results, but at the cost of increased computational resources and time. Future microscope design aim to capture just two views using dual illumination, which should be sufficient for 3D reconstruction.

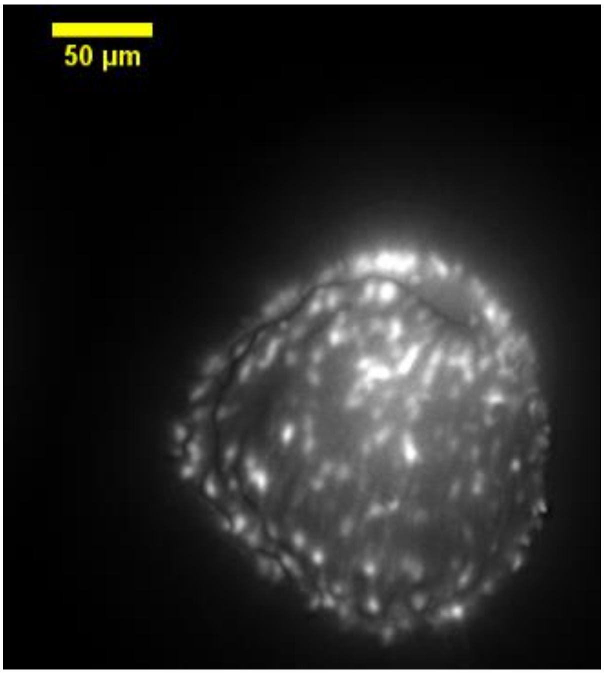

Figure 2.11: Single view maximum intensity projected raw images of a H*ydractinia symbiolongicarpus* head showing cells.

2.13 Discussion and Conclusion

In my research, I have detailed steps in building a L-OpenSPIM using air optics, and I have shown that it can image up to millimetre sized samples and reveal neurites if the sample is sufficiently optically transparent. The diameter of neurites range between 0.1 µm and 6 µm (Fiala and Harris, 1999; Saliani *et al.*, 2017). The platform I have built is very basic. Though theoretical estimates of resolution 0.58 µm (lateral) and 4.07 µm (axial) are different from experimental values 2.88 µm and 4.32 µm respectively, the process involved in assembling the platform and results from the samples imaged are sufficient for inexperienced scientists to gain the required know-how needed to chart the direction for future upgrades. The platform is also a cost-effective way to start learning how to build a DIY platform while giving greater flexibility to engage research interests in-vivo and in-vitro for the appropriate sample size.

A more robust system should image centimetre sized samples at sub-micron isotropic resolution, sufficiently match theoretical estimates, generate a reasonable amount of data, and still keep the platform relatively cost effective. The ability to simultaneously excite and detect different fluorophores within the same sample, and to include user-friendly optics that allow for easy adjustment of the setup whenever necessary is desired.

Adding an extra excitation arm and introducing sequential illumination will largely reduce the known stripe artefact (shadowing), at least halve the number of views required (thus greatly decreasing the amount of data and time for 3D reconstruction) and eliminate widening of the light sheet (caused by powering both arms simultaneously). Including more laser lines aid studies using different fluorophores concurrently within the same sample. An upgrade to a T - openSPIM (additional illumination arm) or X-OpenSPIM (additional illumination and detection arms) version is possible but will be at a cost almost double that of the current L-openSPIM platform I built. For a T or X configuration with a static light sheet, correcting for the position of the waist of both light sheets whenever the imaging buffer changes should be made user friendly. Possible options for our microscope (each of which still requires adjusting the detection) include:

1. To use immersion objectives equipped with refractive index correction collars and caps for different media (e.g., Lavision MI Plan 4x and 12x series). An expensive choice (at least $12,000 - $50,000 apiece), especially considering that each illumination and detection require a piece and there might be a need to contact vendors to manufacture custom made ones. But it greatly simplifies the whole process.

2. If sticking to dual static light sheets, mount the entire optics of the illumination and detection on translation stages. Such can benefit from adaptive optics (Royer *et al.*,

2018).

3. Replacing the illumination arms with axially scanned light sheet optics, which may possibly require the use of electronic tuneable lens (ETL). Axially scanned light sheets may be explored for its quality (more isotropic) raw images combined with improved field of view (Bianca Migliori *et al.*, 2018; Voigt *et al.*, 2020; Dean *et al.*, 2021). Imaging speed for such setups however depends on the speed and amplitude of the scanning optic(s).

In combination with any of these options, the detection axis can also be improved. Detection objectives with a reasonable working distance (~ 5 mm) are preferred as they allow for larger samples within the imaging space. High end cameras with larger detector arrays such as the Andor series can also improve the size of the FOV, and when coupled with dichroic mirrors (a cheaper option to getting more than one camera) can almost simultaneously detect fluorophores of different emission wavelengths. Beyond using expensive immersion objectives, low magnification air objectives (~4x or less) can be combined with a zoom module such as that on the Olympus MVX10 (which gives up to 31x magnification) to reveal more image detail within a field of view up to 20 mm (Voigt *et al.*, 2020). Though the objective is with a reduced NA (lateral resolution), when combined with axially scanned light sheets and a fast camera, high quality isotropic raw images are produced which can be zoomed to focus on features of interest. A downside to this is that such zoom modules are not usually commercially available and mostly taken from parts of decommissioned microscopes. In any case one is put up for sale, it can cost up to $22,000. Macro-objectives can also be explored but would give far less desired result to the use of a zoom lens. The general idea when limited by funding is to equip the platform with at least one detection arm having an objective (air or immersion) with a sufficient NA, a decent camera, and optics that can produce images of regions of interest at the desired resolution and quality (tiling acquisition, possibly for the entire sample). For options 2 and 3 above, mounting the detection on translation stages or piezo instruments help to correct for the displacement of the focal plane in different buffers.

It is more convenient to mount cleared samples by making them sit at the bottom of the imaging chamber or cuvette, especially those that are less rigid after clearing with protocols such as CLARITY. Using a 4D stage that translates the entire imaging space from beneath the sample helps to eliminate the need to constantly 3D print custom holders, avoid tissue damage while mounting, and allows the use of sealed imaging chambers when buffers that are toxic or easily evaporates are used.

Finally, open-source software such as micromanager may not provide the required functionality custom to the research need of individual scientists. For example, the need to ensure stack does not go above the advised 4-gigabyte may require using acquisition step sizes that are relatively large, which in turn limits how much information can be obtained from such procedure. It is therefore important to consider investing in developing an acquisition software in-house with the needed requirements.

Chapter 3 Laser induced Heat in Light Sheet Microscopy: An Assessment on a Blue Light L-OpenSPIM.

3.0 Background

Visible light is often employed in optogenetic (including infrared wavelength) and fluorescence microscopy studies for neural simulation and fluorophore excitation in biological tissues respectively. Tissue heating is evident in these techniques, the degree to which is dependent on biological properties as well as the amount of external energy introduced by light. However, despite the fast-growing pace of the light sheet microscopy technique, the effect of laser induced heat appears to be largely ignored, more so in studies in-vivo. There has been no publication on suggested excitation energy thresholds nor does a phantom for such exist. Although sample imaging chambers are designed to regulate heat, it is still not a direct quantitative approach to ensure tissue integrity is not compromised during examinations. In this chapter, I address this gap by describing a protocol that can be used for investigating tissue heating and laser energy thresholds on the light sheet microscope I built, and that can be applied to other light sheet microscopes.

Optogenetics involves the use of visible light to modulate neural activity (pumps and channels) by accurately targeting cell populations. The aim is to integrate light sensitive techniques into cells for gene therapy. In contrast to light sheet microscopy, associated heating effects in brain tissue have been previously described (Christie *et al.*, 2013; Stujenske, Spellman and Gordon, 2015; Shin *et al.*, 2016; Senova *et al.*, 2017; Dong *et al.*, 2018; Picot *et al.*, 2018; Peixoto *et al.*, 2020; Karadas *et al.*, 2021). Usually, these studies characterise the temporal and spatial distribution of heat under varying illumination conditions; by describing numerical models of light propagation and heat transfer within scattering media or biological tissues, and performing experimental measurements. Notably, experimental measurements are made in-vivo or using phantoms and can be compared with numerical models to make useful inferences. Numerical models have a unique advantage of making good predictions. Though to effectively compare results, a correction for intrinsic errors associated with the experimental setup or device may be needed.

There are several samples reported in literature to have been imaged on a light sheet microscope. These are of different sizes ranging from small (~ 10 µm), medium (~ 100 µm), large (order of mm), to very large (order of cm). Drosophila and Zebrafish are in the range of large samples and are well known to have been imaged for their morphological and temporal processes in a good number of studies. The centimetre-sized central nervous system of a mouse has also been imaged in-vitro and in-vivo (Holekamp, Turaga and Holy, 2008; Engelbrecht, Voigt and Helmchen, 2010; Matthew B. Bouchard *et al.*, 2015; Bianca Migliori *et al.*, 2018; Corsetti, Gunn-Moore and Dholakia, 2019; Ueda *et al.*, 2020). Calcium dynamics are triggered by neuronal activities. Indeed, at the time of writing this text, at least 60 studies in the last twelve years demonstrate calcium imaging in different samples using a light sheet microscope, without recourse to the effect of induced heat. The latest study being (Djenoune *et al.*, 2023). Such sample physiology and embryonic spatio-temporal development are known to be temperature dependent, and the ignored effect of heat can cofound results especially in quantitative studies. Currently, light sheet microscopy studies do not incorporate the effect of laser induced heat.

Normal physiology regulates tissue temperature in-vivo. Stujenske, Spellman and Gordon, (2015) suggests that the effects of convention and metabolism on temperature changes before steady state is negligible by removing terms representing both quantities in a heat transfer numerical simulation, thereby attributing temperature rise in laser heated tissue mostly to conduction. This implies temperature change measurements for a sample before steady state when studied in-vivo should largely correlate with in-vitro data. Amongst the range of samples that have been imaged on a light sheet microscope in-vivo, the mouse arguably has the most complex and effective heat regulation processes. Thus, at different excitation energies I can experimentally examine heating effects on the brain of a mammal in-vitro (which should suggest a worst-case of heating scenario) from which inferences can be made to in-vivo cases. I can also apply a slightly adjusted optogenetic framework of numerical simulation studies that investigate tissue heating to light sheet microscopy. Both the experimental and numerical protocols can be applied to any light sheet platform and suggest minimum thresholds for light sheet imaging procedures to improve experimental accuracy and reproducibility.

Subsequently, I highlight useful information on light propagation and heat transfer on a light sheet microscope with bias to the L-OpenSPIM design. I also implement a previously published numerical simulation of Monte-Carlo light propagation and Pennes bioheat transfer equation, but slightly adjusted to work out temperature changes on the brain of a lamb for different laser energies. Finally, I perform experimental measurements on our L-openSPIM using Gray matter tissue of a lamb and compare both data sets.

3.1 Light propagation in Biological Tissues

Light delivery to biological tissue is partially reflected at the tissue surface and partially transmitted or refracted through the tissue (Peixoto *et al.*, 2020). Within the range 400 nm to 900 nm, transmitted light is mostly scattered (Dé Ric Bevilacqua *et al.*, 1999; Yaroslavsky *et al.*, 2002; Dong *et al.*, 2018), and absorbed linearly and non-linearly within the tissue (Picot *et al.*, 2018). Details of the scattering phenomenon of light are described in literature (Welch and Van Gemert, 2011; Vo-Dinh, 2014). While absorption accounts for heat generation within tissues, it does not significantly affect the intensity of light propagation through tissue depths.

The Kubelka-Munk and Monte Carlo numerical models are two major techniques that have been used to simulate light intensity at different depths within tissue, considering absorption and scattering effects. The former is simpler and approximates experimental results for depths within ~ 1 mm (Aravanis *et al.*, 2007; Stujenske, Spellman and Gordon, 2015; Peixoto *et al.*, 2020). Beyond an exponential fit, Monte Carlo simulations are complex with long simulation times. It is also challenging to incorporate diffraction (and the electromagnetic field for holographic beams) into the Monte Carlo codes (Brandes *et al.*, 2014; Picot *et al.*, 2018). Nonetheless, it is more accurate.

3.1.1 Kubelka-Munk Model

The Kubelka-Munk model assumes constant absorption and reflection over a certain thickness of a homogeneous sample illuminated with light of single wavelength incident on a plane surface (Peixoto *et al.*, 2020). I subsequently describe this model adapted for a light sheet platform with a Gaussian beam propagated in the transverse electromagnetic mode (TEM_{00}).

Consider a molecule (absorber) that absorbs light of a specific wavelength, with a numeric density ρ_a (m^{-3}) within the tissue. The coefficient of absorption μ_a for an absorber is given as equation 3.0, where σ is the cross section of the absorption, and is a function of the direction of propagation of the plane wave with relative to the absorber γ.

$$\mu_a = \rho_a \sigma_a(\gamma) \qquad 3.0$$

The transmittance which measures the connection between the intensity of light outside the tissue and that through the tissue at a thickness or distance Z, considering scattering and absorption is given as

$$T = \frac{b}{a\sinh(bZ\mu_s) + b\cosh(bZ\mu_s)} \qquad 3.1$$

$$a = 1 + \frac{\mu_a}{\mu_s}$$
$$b = \sqrt{a^2 - 1}$$

μ_s = scattering coefficient

Assuming conservation of energy, the decrease in the intensity of light; measured as the geometric loss (g_{loss}) up to the distance Z as it propagates and spreads through the tissue is usually modelled as a canonical shape from the tip of the light source, i.e., from the waist of the light sheet which is incident on the sample. For a 2D model, the divergence angle θ for the canonical shaped loss is

$$\theta = \sin^{-1}\left(\frac{NA_{exc}}{n}\right) \qquad 3.2$$

n = tissue refractive index. The NA_{exc} which largely determines the thickness of the lights sheet is the numerical aperture of the illumination optic that form the light sheet and/or projects it to the sample.

g_{loss} is then given as

$$g_{loss} = \frac{\rho^2}{(Z+\rho)^2} \qquad 3.3$$

$$\rho = r\sqrt{(\frac{n}{NA_{exc}})^2 - 1} \qquad 3.4$$

r is half the thickness of the light sheet. If the light intensity I at the waist of the light sheet is

$$I(Z_i = 0) = \frac{P}{A\eta} \qquad 3.5$$

A= cross sectional area of illuminating light (i.e., a product of the thickness and height of the light sheet), P= power of the light source, η= coupling efficiency between the illumination optics and beam.

then, the light intensity as the light sheet propagates through the tissue, at any thickness Z (distance from the waist of the light sheet), considering scattering, absorption, and geometric loss is thus given as:

$$I(Z_i = Z) = I(Z_i = 0).g_{loss}.T \qquad 3.6$$

3.1.2 Monte-Carlo Model

In contrast to the Kubelka-Munk model, the key feature of the Monte-Carlo model is the simulation of an unidealized propagation of light (Figure 3.0). Here, the problem remains to consider within each voxel or unit tissue volume the probability of absorption, scattering, reflectance and transmittance of light photons, considering local tissue properties. This informs the intensity or fluence rate per voxel.

Neural tissue can be modelled using cylindrical coordinates with absorbing ends, in which each photon packet is initiated to start from a random position on the circular surface and scattered in a direction determined by; a defection-scattering angle θ relative to the radial plane, and an azimuthal-scattering angle φ relative to the plane orthogonal to the circular surface. The value of θ is chosen randomly between 0 and 2π from g; a probability distribution of cosine θ that describe varying degrees of anisotropy governed by a phase function (Henyey-Greenstein phase distribution), equation 3.7 (Wang, Jacques and Zheng, 1995; Stujenske, Spellman and Gordon, 2015).

$$P(\cos\theta) = \frac{1-g^2}{2(1+g^2-2g\cos\theta)^{3/2}} \qquad 3.7$$

g = cos θ, P = phase distribution function

The angle φ chosen from a uniform random distribution defines possible angles that can be subtended in a canonical distribution of light, ideally modelled by a cartesian coordinate system (Wang, Jacques and Zheng, 1995; Peixoto *et al.*, 2020), but can be easily implemented in the Monte-Carlo code using equation 3.8. In principle, 3.8 is similar to 3.2, since Y_n is chosen randomly between 0 and 1; which are the possible solutions to 3.2.

$$\varphi_{n,t} = 2\pi Y_n \qquad 3.8$$

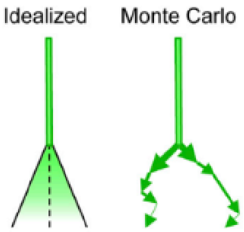

Figure 3.0: Schematic of light propagation through a tissue as implemented in Kubelka Munk (idealised) and Monte Carlo (unidealized) models. As shown in Figure 1 (Stujenske, Spellman and Gordon, 2015). Adapted from Stujenske, J.M., Spellman, T. and Gordon, J.A. (2015) 'Modeling the Spatiotemporal Dynamics of Light and Heat Propagation for InVivo Optogenetics', Cell Reports, 12(3), pp. 526. Available at: https://doi.org/10.1016/j.celrep.2015.06.036, under the Creative Commons license CC-BY-NC-ND (http://creativecommons.org/licenses/by-nc-nd/3.0/)

The sampling of the possible direction of transport of a photon packet based on θ and φ at each discretised step can be done using a spherical coordinate system, which has its z-axis dynamically (repeatedly) aligned to a determined propagation direction. The random distance D moved by the n^{th} photon packet at a time t considering absorption and scattering is given by:

$$D_{n,t} = \frac{-\log X_n}{\mu_a + \mu_s} \qquad 3.9$$

X_n is randomly chosen from a uniform distribution between 0 and 1.

To factor in energy decrease due to absorption, a photon packet can be assigned a weight $W_{n,t+1}$ decreased from the initial $W_{n,t}$ (weight of the n^{th} photon at a time t), until it is extinguished or of very low energy;

$$W_{n,t+1} = W_{n,t}\left(\frac{\mu_s}{\mu_a + \mu_s}\right) \qquad 3.10$$

and the total weights (energy) built up in a voxel in which a photon packet is currently positioned at a time t is $W_{r,z,t}$ given as:

$$W_{r,z,t+1} = W_{r,z,t} + W_{n,t}\frac{\mu_a}{\mu_a + \mu_s} \qquad 3.11$$

r and z are radial and z (orthogonal to the radial plane) coordinates of the cylindrical coordinate system respectively.

The light intensity or fluence rate in each voxel $\phi_{r,z}$, which is a function of the total photon energy flow in the voxel per unit area is therefore

$$\phi_{r,z} = P\frac{W_{r,z}}{\mu_a 2\pi n_p (r-0.5)dr^2 dz} \qquad 3.12$$

n_p = number of photon packets. $n_p > 10^6$ to avoid noise at positions directly below the source of light. dr and dz are the discrete parameters for propagation in the radial and tissue depth directions respectively. P is the power of the light source.

3.2 Heat transfer in Biological Tissues

Heat is generated within biological tissues at the instance of the absorption of light, and the wavelength at which light is incident on an absorber is key to determine if absorption takes place. The heat produced is diffused with a thermal distribution gradient that depends on local tissue morphology, physiological conditions, and incident light parameters while being radiated as fluorescence or used up in other photochemical processes (Arias-Gil *et al.*, 2016).

Several studies model heat transfer differently. Brain tissue can be approximated as a homogeneous medium with thermal diffusivity D and initial temperature T_0 (Peixoto *et al.*, 2020), with equal vascularisation (Stujenske, Spellman and Gordon, 2015). In such a simplified model, the Fourier's heat diffusion equation can describe the temperature T distributions over time t and space r (Picot *et al.*, 2018).

$$\frac{\partial T(\vec{r},t)}{\partial t} = D\nabla^2 T(\vec{r},t) + \frac{\phi(\vec{r},t)\mu_a}{\rho C} \qquad 3.13$$

$\phi(\vec{r},t)$ is as described in 3.12, and $\phi(\vec{r},t)\mu_a$ refers to the heat source from absorption. ρ and C are the density and specific heat of the tissue respectively.

However, beyond tissue morphology, the Pennes bio-heat equation (equation 3.14) is more suited for complex organisms that require robust models which in addition to external heat sources incorporate the effects of metabolic heat and cooling from blood perfusion.

$$\frac{\partial T(\vec{r},t)}{\partial t} = D\nabla^2 T(\vec{r},t) + \frac{\phi(\vec{r},t)\mu_a}{\rho C} + \frac{q_m - q_p}{\rho C} \quad 3.14$$

q_m is the heat source from metabolism, q_p is the cooling term from blood perfusion.

For a 2D study, equation 3.14 becomes

$$\rho C_p \frac{\partial T}{\partial t} = \nabla(k\nabla T) + q_s + q_m - q_p \quad 3.15$$

q_s = heat from light source, k = thermal conductivity

$q_p = \rho_p \omega_p C_p (T - T_p)$, ρ_p = blood density, ω_p = blood flow, C_p = blood specific heat, T_p = local blood temperature, T = local tissue temperature.

Under normal physiological conditions, tissue temperature should be constant (i.e., the heat generated from metabolism should be balanced by blood perfusion, $q_m - q_p$ equals zero), and for small temperature changes ~ 1 K, equations 3.14 and 3.15 are almost linear (Picot *et al.*, 2018; McGlynn *et al.*, 2021). This indicates the temperature rise is largely dependent on (proportional to) the source term q_s (Peixoto *et al.*, 2020), and tissue cooling is mainly by the diffusion of heat away from the irradiated area (Elwassif *et al.*, 2006; Stujenske, Spellman and Gordon, 2015; Picot *et al.*, 2018; Peixoto *et al.*, 2020), though there be increased perfusion capacity (vascular dilation) to counter metabolic and reduce Joule heat (Elwassif *et al.*, 2006; Christie *et al.*, 2013).

A simplified case of 3.14 is to eliminate the net contribution of metabolism and perfusion for which a solution of the resulting equation $T(\vec{r},t)$ can be further expressed as a convolution of a function (Green's function $G(\vec{r},t)$) (equation 3.16) with the heat source function $\phi(\vec{r},t)\mu_a$ over space and time. This solution is further aided by expressing the source as separable variables of space $\Gamma(\vec{r})$ and time $\Pi(t)\mu_a$ which simplifies the description of the light source propagation (equation 3.17) (Picot *et al.*, 2018). The use of the Green's function approach allows investigations with micrometer and millisecond resolution and eliminates time consuming iterative processes that depend on carefully setting the spatio-temporal discretisation steps for accurate numerical solution (as in the Finite Element numerical method).

$$G(\vec{r},t) = \frac{1}{\left(4\pi Dt\right)^{3/2}} e^{-\left(\frac{r^2}{4Dt}\right)} \qquad 3.16$$

Where $r = x^2 + y^2 + z^2$

$$\phi(\vec{r},t)\mu_a = \Gamma(\vec{r})\Pi(t)\mu_a \qquad 3.17$$

However, I adopt the finite element method (FEM) numerical resolution to equation 3.15 provided by (Stujenske, Spellman and Gordon, 2015) in this research as it can easily be adapted to the illumination framework of the L-openSPIM I built. The framework of the green function solution provided by (Picot *et al.*, 2018) and implemented in the MATLAB software is developed for 2-photon pulsed illumination (and not continuous wave illumination which we have on our L-openSPIM). Nonetheless, considering its merits, it will be interesting to examine how results compare to that from a FEM solution and experimental measurements on a continuous wave light sheet platform in a different research. Based on the FEM solution, the heat H generated at a depth Z in a tissue of assumed flat surface when illuminated with a gaussian beam of power P centred at (x_0, y_0) can be further described (Peixoto *et al.*, 2020), as

$$H(x,y,z) = P(1-R)\frac{\mu_a}{\pi\sigma_x\sigma_y}\exp\left[-\left(\frac{(x-x_0)^2}{2\sigma_x^2}\right)+\left(\frac{(y-y_0)^2}{2\sigma_y^2}\right)\right]\exp\left(-\mu_a Z\right) \qquad 3.18$$

R is the reflection coefficient of the tissue. x and y are the new x and y coordinate the beams is scanned to from its initial point (x_0, y_0). σ_x and σ_y are the respective standard deviations. The first and second exponent functions represents the normal distribution of the heat in the x-y plane, and the heat loss with increasing tissue depth Z, respectively.

Stored energy (from metabolism) in tissues is increased from its initial state by the laser radiation (Aravanis *et al.*, 2007). Through convective processes (blood perfusion through the vascular network) and radiative processes (such as loss of water vapour) there is a thermal diffusion away from the irradiated area depending on the existing temperature gradient in the tissue (Welch and Van Gemert, 2011; Picot *et al.*, 2018; Peixoto *et al.*, 2020). Convection effects in heat transfer can be challenging to estimate, depending on the tissue type, vascular network present, geometry, and shape of the boundary at which convective heat transference occurs, and the characteristics of other associated processes that can affect the convective transfer. For simple boundary conditions, the convective heat exchange between the solid and fluid of different temperatures q_c is defined by the Newton's law of cooling (Welch and Van

Gemert, 2011; Peixoto *et al.*, 2020), as

$$q_c = h(T - T_{external}) \quad 3.19$$

h =convective heat transfer coefficient, T = temperature of a body, $T_{external}$ =Temperature of the environment external to the body

However, Stujenske, Spellman and Gordon, (2015) suggests the convective phenomenon contributes less than conduction in heat dissipation, and that neglecting effects of convection and metabolism do not significantly contribute to temperature rise particularly before steady state. Thus, experimental measurements may be made to investigate heating effects and produce meaningful results not just in-vivo, but in-vitro too. Temperature changes before steady state should largely correlate between in-vivo and in-vitro data (either numerically or experimentally measured).

The specificity of experimental measurements is determined by the resolution of the thermal measuring device. Thermocouples and infrared cameras measure averaged temperature rises over a relatively large area (Arias-Gil *et al.*, 2016; Picot *et al.*, 2018), and may be more suited for measuring heating profiles or patterns that are continuous. Quantum dot nanothermometers (quantum dot thermometry) might give a better resolution spatially, but it is poorer temporally (~ 1 s) (Podgorski and Ranganathan, 2016; Picot *et al.*, 2018).

In a simplified 2D study, I compare experimental data with the finite element solution to the complex or simplified equation 3.15 (temperature change in time), at a distance Z within a tissue with the assumption that its surface (Z = 0) is flat. In this research, though I examine tissue heating on an L-OpenSPIM microscope, the principle is approximately the same for other light sheet platforms. I subsequently examine temperature changes on the gray matter of an excised lamb brain. I investigate energy thresholds that better preserves tissue integrity during blue light investigation on our SPIM by; examining temperature changes in relation to known perturbations in normal physiology already published in literature. Gray matter tissue of the brain was chosen as the numerical simulation framework adopted from optogenetics (to be compared with experimental results) is designed for such i.e., the tissue is assumed homogenous Gray matter.

3.3 Methods - Experimental Setup

The L-OpenSPIM microscope used was equipped with a 488 nm blue light laser (LuxX 480-60) and a 0.13NA illumination objective (Nikon, N4X-PF). A cylindrically shaped lamb brain tissue of height ~ 4 mm freshly excised was made to protrude from a 1 ml syringe (Fisher Scientific 14955456) mounted on a 4D stage and translated in the z-direction for a very small distance of 130 µm across the light sheet for 60 seconds, to simulate incidence on a flat tissue surface and the usual acquisition protocol on a light sheet microscope. A lamb brain was chosen to represent living samples imaged on a light sheet microscope that would absorb the most laser energy. Heat maps were simultaneously recorded at intervals of 10 s with a thermal camera (FLIR ONE Pro LT) placed directly below the brain tissue. The protocol was done for 10 mW, 20 mW, 30 mW, 40 mW, 50 mW and 60 mW laser power, each time using a freshly prepared sample positioned at a predefined spatial coordinate that ensures the same area of exposure to the laser light. Each sample was brought to the same baseline temperature of ~ 16 ^{o}C before heating, as maintaining the sample at the normal physiological value of 37 ^{o}C was not practically feasible.

FLIR Tools software (version 5.13) was used to analyse the recorded heat maps for maximum temperature changes over a region of interest closest to the light source. The data was normalised with room temperature, and then each recorded peak value was baseline temperature corrected by first multiplying with the factor [(37 – 16) ^{o}C / 37 ^{o}C] and adding to the uncorrected peak value.

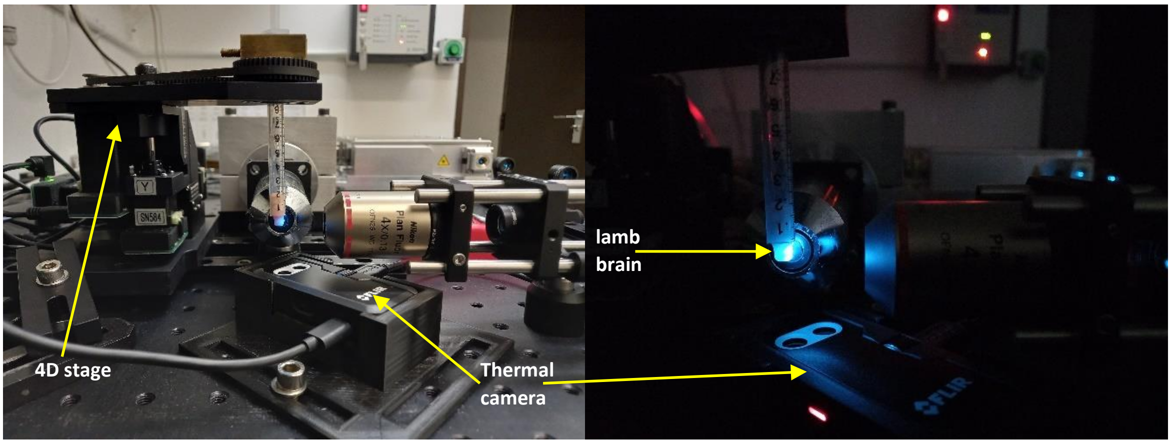

Figure 3.1: Experimental set up for testing temperature changes on a lamb brain suspended from a syringe in the path of a blue light sheet at different power levels and time. The same set up shown in figure 2.0 is used, except that the glass cuvette and metal slab are removed and replaced with the thermal camera. Heat maps are recorded with the aid of a FLIR ONE Pro LT thermal camera.

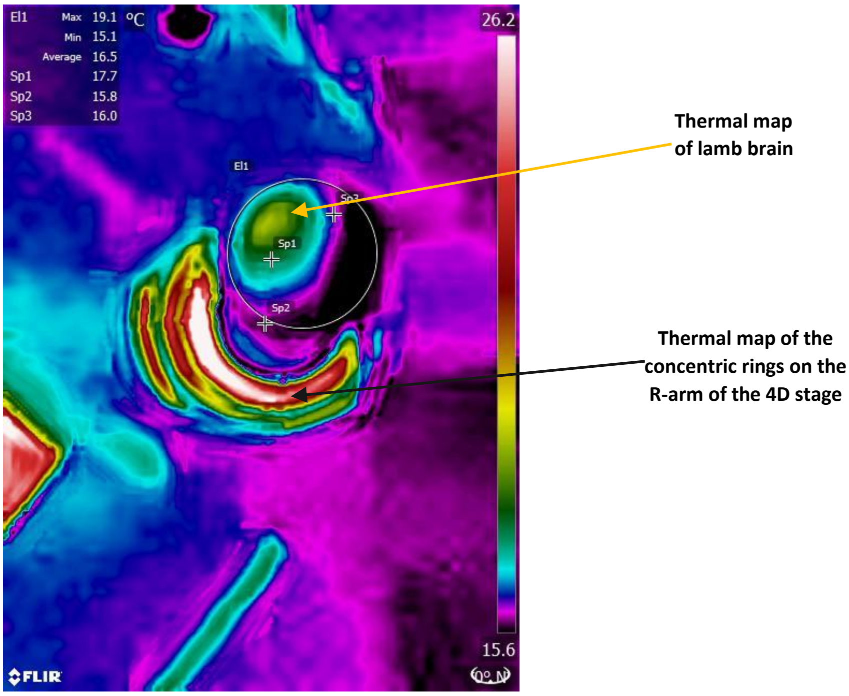

Figure 3.2: Sample heat map showing temperature gradients. Local hotspots can be observed with spot meters (sp1, sp2, and sp3) and the circular meter E11 reports the maximum, minimum and average temperature changes for the region of interest within the circle. Thermal gradient of the lamb brain can be seen within E11.

3.4 Methods - Numerical simulation

The Monte-Carlo light propagation and Pennes bioheat transfer models (equation 3.15) implemented in MATLAB by Stujenske, Spellman and Gordon, (2015) was used but with slight modifications to suit light sheet illumination. To tailor the simulation to our experimental setup, parameters representing perfusion were removed, and those of the surrounding blood were replaced by that of air. An optical fibre beam radius of 51.9 µm corresponding to the 488 nm rectangular light sheet waist area of 8463 μm^2 was adopted (i.e., 4.03 µm light sheet thickness from an underfilled illumination NA multiplied by the height of the light sheet 2.1 mm (using the full NA of the illumination will correspond to 3948 μm^2 area and an optical fibre beam radius of 34.4 µm). 10^7 photon packets were implemented to limit noise. Brain constants adopted from Elwassif *et al.*, (2006) and Janssen, Van Leeuwen and Van Steenhoven, (2005) include density = 1.04 x 10^{-6} Kg/mm^3, specific heat = 3.65 x 10^{-}

^{6} mJ/(kg·°C), and whole brain thermal diffusivity constant = 0.527 mW/(m·°C). Temperature changes from a baseline of 37 °C were recorded at 2.5 s and 5 s interval to ensure proper sampling before steady state, and then 10 s at steady state.

3.5 Results

Figure 3.3 is a graphical representation of the numerical and experimental data. The numerical simulation shows peak values of (0.5±0.1) °C, (0.9±0.1) °C, (1.4±0.2) °C, (1.8±0.3) °C, (2.3±0.3) °C, and (2.7±0.4) °C within the first 20 s of heating at 10 mW, 20 mW, 30 mW, 40 mW, 50 mW, and 60 mW respectively. Steady state was observed after 15 s to 20 s. Experimental peaks recorded within the same timeframe were approximately (0.1±0.1) °C, (0.8±0.2) °C, (1.8±0.2) °C, (1.4±0.2) °C, (2.2±0.3) °C, and (3.2±0.2) °C. Corresponding baseline corrected values were roughly (0.2±0.3) °C, (1.3±0.4) °C, (2.8±0.3) °C, (2.1±0.3) °C, (3.4±0.4) °C, and (5.0±0.4) °C. Generally, the numerical and uncorrected experimental data show greater similarity especially within the exposure time for a temperature rise of ~ ≤1^{0}C. Interestingly these similarities occur before steady state.

The least recorded time of exposure to elicit a response of ~ ≥ 1 °C temperature rise for the numerical setup were observed to be about >>>10 s (did not heat up to 1 °C), 10 s, 8 s, 6 s, 4.5 s, 4 s for 10 mW, 20 mW, 30 mW, 40 mW, 50 mW, and 60 mW power respectively. Corresponding values recorded for the experimental design were approximately 32 s, 22 s, 8 s, 7 s, 7 s, and 4 s respectively. Baseline corrected values were 26 s, 10 s, 5 s, 4 s, 4 s, 3 s. The intensities (power per unit area) applied by the light sheet of waist area 8463 μm^2 to tissue of same area for 10 mW, 20 mW, 30 mW, 40 mW, 50 mW, and 60 mW are approximately 1182 mW/mm^2, 2363 mW/mm^2, 3545 mW/mm^2, 4726 mW/mm^2, 5908 mW/mm^2, 7090 mW/mm^2

respectively. This implies such intensity values should not be applied for more than the exposure times earlier stated, to ensure temperature rise is ~ $\leq$ 1 ^{o}C. As the corrected experimental values appear to be more conservative, I define it as threshold values for the L-openSPIM platform I built.

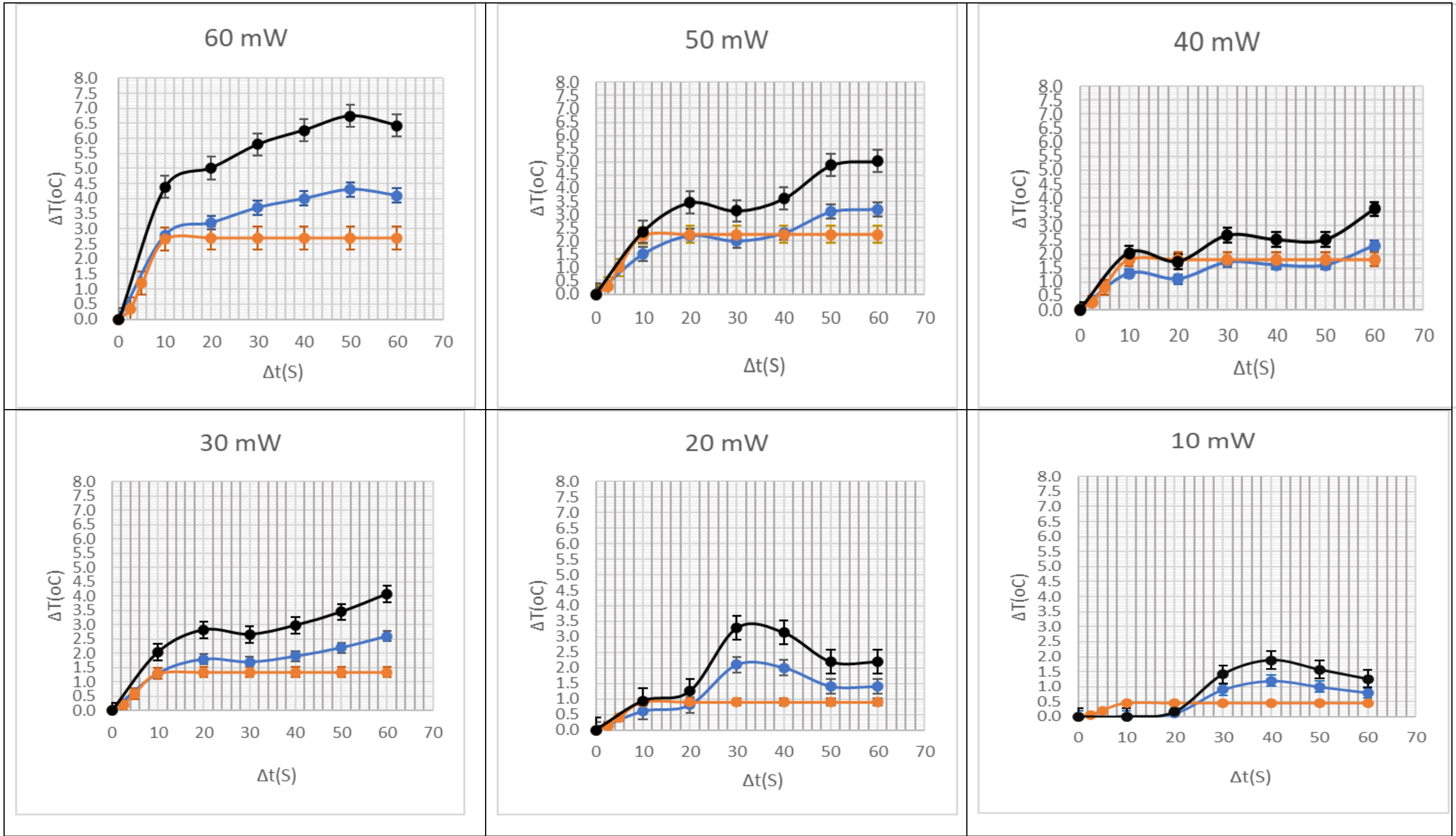

Figure 3.3: Maximum temperature changes observed from illuminating a 130 µm gray matter of a lamb brain with blue light at 10 mW, 20 mW, 30 mW, 40 mW, 50 mW, and 60 mW. As opposed to a baseline temperature of 16 °C set for the experimental protocol, 37 °C was implemented in the numerical simulation to represent the actual temperature of a live mouse. Standard error of the mean measurements are included in the plots rather than the systematic error of the thermal camera that applies only to the experimental data.

3.6 Discussion

In this study, I have tested a lamb brain as a possible worst case of tissue heating among samples that are imaged in-vivo on a blue light L-OpenSPIM microscope over one minute. I have examined temperature changes for different energy-time exposure values for experimental and numerical designs. Specifically, I have suggested intensity threshold values that should limit tissue temperature rise to ~ <1 ^{o}C beyond which can cause systemic alterations to neuronal activities in-vivo (Elwassif *et al.*, 2006; Stujenske, Spellman and Gordon, 2015; Peixoto *et al.*, 2020), and cell damage.

Differences in measurements between the experimental and numerical setups are noted especially for the period starting from 10 s and 20 s. This can be due to tissue inhomogeneity in the experimental setup. The brain samples I used in this study were not entirely made of Gray matter. Some blood was still embedded in the tissue (which is a good absorbers of visible light). Also, tissue property constants used in the numerical simulation were gotten from publications which might not be exactly accurate or differ. The absorption coefficient used for in-vivo studies are usually greater than those for in-vitro studies possibly to incorporate light absorption in blood and melanin in in-vivo studies (Zhang *et al.*, 2015; Peixoto *et al.*, 2020).

The elimination of perfusion and replacement of surrounding blood with air in the numerical simulation, and for practical reasons the use of different baseline temperatures is a potential contributing factor to the temperature differences observed between the datasets. The temperature gradients within a biological tissue can be influenced by several factors, including the thermal properties of the tissue, the mechanisms of heat transfer, the initial temperature distribution, and the characteristics of the heat source. As a result, when heating the same tissue with the same power and for the same duration but starting from different baseline temperatures, variations in temperature gradients within the tissue can occur.

However, results obtained show that there is not much disparity between the numerical and uncorrected experimental results before steady state of the numerical data (i.e., region below 20 s) despite having different baseline temperatures. Experimental temperature changes that are baseline corrected for the experimental setup are generally higher (Figure 3.3). This might suggest that the difference in baseline temperature potentially might not be an issue when performing similar investigation for a temperature rise to $\leq 1^0$C. This also possibly supports the assertion by Stujenske, Spellman and Gordon, (2015) that temperature changes before steady state are majorly due to conduction. Moreso, beyond 20 s (the onset of steady state in the numerical data), the experimental data (especially the corrected values) appear to show significant higher peaks than its initial values up to 20 s, and still do not appear to have reached steady state at 60 seconds. This could be due to blood (good heat absorber) that is still present and not perfused within the lamb brain sample. Though for the 10 mW and 20 mW data the peak values beyond 20 s appear to be exaggerated possibly due to experimental errors.

The Kubelka Munk and Monte Carlo codes possibly due to a large degree of assumptions do not capture the extent of the lateral light distribution mechanism beyond the radius of interest (Senova *et al.*, 2017). This is ignored in our study since I record maximum rather than average temperature changes. Also, for this reason, scanning of the sample through the light sheet is not implemented in the numerical simulation. The use of thermocouple to record temperature changes in our study is desired. However, thermocouples are not area specific enough. Our L-OpenSPIM and the numerical heating affect a relatively small area and the sample overall will reach thermal equilibrium with the surroundings. On the other hand, a thermal camera will focus directly on the site of illumination to find these local hotspots. Numerical simulations were conducted over a small area, and it was noted outside this area that the tissue remained in thermal equilibrium with the surroundings.

3.6.1 In-vivo effects of laser induced heat on neural activity.

There are obvious thermal effects associated with linear absorption of light, and photochemical damage (including photobleaching and phototoxicity) from non-linear absorption (Picot *et al.*, 2018). Importantly, these become significant in light sheet microscopy when there is a repetitive scanning of small volumes to capture different views that aid 3D reconstruction. Commonly imaged samples on light sheet microscopes for calcium dynamics are Drosophila (Rebollo *et al.*, 2014; Lemon *et al.*, 2015; M B Bouchard *et al.*, 2015; Simpson and Looger, 2018; Yoon *et al.*, 2019; Chen *et al.*, 2021; Han *et al.*, 2021; Liang, Holy and Taghert, 2022; Mitchell *et al.*, 2022), and Zebrafish (Zhao *et al.*, 2021; Silic *et al.*, 2022; Turrini *et al.*, 2022; Zarei *et al.*, 2022; Zhang and Kindt, 2022). Their embryonic developmental processes are equally known to be affected by temperature shifts (HATA *et al.*, 1994; Lucchetta, Munson and Ismagilov, 2006; Kuntz and Eisen, 2014; Jalal, Andersen and Hessen, 2015; Chong, Amourda and Saunders, 2018; Christou *et al.*, 2018; Dimitriadi *et al.*, 2018; Urushibata *et al.*, 2021; Wang *et al.*, 2023). Arguably, the largest and most physiologically complex of biological tissues imaged in-vivo till date on a light sheet microscope is the mouse brain, a mammal.

Brain functions are particularly sensitive to temperature changes, depending on the brain regions and properties (Picot *et al.*, 2018; Eguchi *et al.*, 2020; Wu *et al.*, 2022). Membrane properties including voltage gated channel kinetics, and the regulation of accumulated neurotransmitters and ions in the neuronal environment can change significantly. This has been suggested to alter the spiking rate and firing thresholds of neurons for as little as 1 ^{0}C change (Elwassif *et al.*, 2006). Also, heat generated from the direct stimulation of light-driven ions channels and pumps such as in optogenetic studies can alter the size and shape of action potentials, and increase the frequency of spontaneous firing of single neurons (Peixoto *et al.*, 2020). The time required for the synchrony of interneural networks could further be affected. Stujenske, Spellman and Gordon, (2015) reported that for a power of 5 - 10 mW on a 532 nm experimental set up, firing rates could be altered by up to 42.9 $\pm$ 17.4 % after 30 s of illumination, which corresponds to a $\geq$ 1 ^{0}C temperature change. Furthermore, a 2.2 ^{0}C average temperature rise was observed for a numerically simulated 10 mW – 532 nm continuous wavelength illumination of the same spot, at tissue depths within a few hundred microns (~400 µm) of a circular area of radius 250 µm, and a 4.1 ^{0}C maximum temperature rise within a single voxel in 60 s. At steady state temperature (taken after 60 s), less than 5 percent additional increase in a further 60 s was observed and an average temperature rise of $\geq$1 ^{0}C rise within 1 mm^3 volume.

3.6.2 Effects of illumination framework

The dynamics of illumination may also influence observed temperature changes. First is the beam area. Optic fibres with smaller apertures and thinner light sheets may produce greater temperature peaks as there is a reduced area of exposure to the same energy. Also in light sheet microscopy, the use of more than one illumination arm is adopted and powered sequentially to aid a deeper and more uniform imaging, but it may increase the heat deposited within tissues.

Pulsed illuminations are known to pose photobleaching and phototoxicity problems, and the build-up of heat within tissues is equivalent to that by continuous wavelengths if the power levels are low ($\leq$10 mW). High illumination power (100 mW/mm^2 – 600 mW/mm^2) may be required to image deep tissue areas (~3mm), and blue light at 476 nm which is widely used in neuroscience research may not penetrate beyond 500 µm within a power range that will pose a non-thermal damage. As illumination of longer wavelengths would penetrate deeper in tissues, they produce smaller temperature changes as they are less absorbed (Stujenske, Spellman and Gordon, 2015). The Red (and where possible infrared) wavelength may be more promising as it relatively exhibits minimal scattering, low absorption and could still reach a depth of about 3.1 mm at 5 mW/mm^2. Even at high irradiance of 600 mW/mm^2 – 40 Hz, temperature rise from such can be below 2.5 ^{0}C and still shows no significant cell damage nor obvious phototoxic effect, though may elicit physiological changes (Senova *et al.*, 2017). However, this is beneficial only for absorbers (fluorophores) that are red-shifted or naturally within the red-light range. Importantly, light entering a region with a different refractive index can experience dispersion leading to changes in its wavelength. When modelling light propagation, it is important to consider the possible wavelength shifts along the different regions once the shift is significant enough to alter known tissue response (Zhang *et al.*, 2015; Peixoto *et al.*, 2020).

3.7 Conclusion

I have investigated tissue temperature changes ex-vivo on a blue light sheet L-OpenSPIM suggesting maximum changes that should occur in a corresponding in-vivo setup. Moreso, the effect of heat is of greater concern in in-vivo procedures as solvent clearing of fixed samples to ensure optical transparency is likely to greatly reduce the absorption of excitation light, while keeping biological structures of interest intact. In summary, to ensure tissue preservation and experimental accuracy in in-vivo light sheet microscopy procedures, energy-time thresholds should be investigated as it is platform specific, and should limit temperature rise to ~ $\leq 1^0$C. Specifically, for the L-openSPIM I built, 10 mW, 20 mW, 30 mW, 40 mW, 50 mW, and 60 mW corresponding to intensity values of 1182 mW/mm^2, 2363 mW/mm^2, 3545 mW/mm^2, 4726 mW/mm^2, 5908 mW/mm^2, and 7090 mW/mm^2 should not be applied to 1 mm^2 of mammal tissue for more than 26 s, 10 s, 5 s, 4 s, 4 s, and 3 s, respectively. Heating effects should also be modelled into studies where feasible (Song, 2019). The use of fluorophores excited with less absorbed (longer) wavelengths is also strongly encouraged (Elwassif *et al.*, 2006; Dong *et al.*, 2018).

The protocol I have described can be applied to other microscopes and at different wavelengths. Also, though phantoms can be easily prepared whenever needed and developed with specific absorption properties to mimic tissues of interest, it could be challenging to achieve baseline temperatures of ~ 37 ^{o}C. A more accurate setup will involve the use of a light sheet in exciting the cortex of a living mammal (such as a mouse) while measuring temperature changes simultaneously at a resolution as high as possible. This will produce results that can be more accurately compared with the numerical data.

Chapter 4 Conclusion

4.0 Application of our In-Air optics SPIM in Biological Tissue Studies.

Over the last two decades, there have been rapid advances in fluorescence microscopy techniques that have revolutionised biomedical research, cutting across several fields such as neurophysiology and drug delivery, genetic manipulation, and embryonic development. Generally, these range from single molecule techniques (STED, SIM, PALM) to those convenient for fast long term whole organ or organism imaging (light sheet fluorescence microscopy, SPIM), and then to hybrid systems that combine these features.

The 'holy grail' of microscopy as described by Whitehead *et al.*, (2017) is to image biological systems at a very high spatial and temporal resolution without introducing external disturbances sufficient to alter the structure or dynamics being studied. By inference, an ideal microscope should have the capacity to produce 3D volumes of different tissue sizes (cells to whole organisms) at a very fast speed with no significant effect from laser induced heat nor photobleaching. In addition, it should support physiological conditions and refractive index matching for in-vivo and in-vitro imaging for a wide range of samples. Finally, it should be an automated platform that perform deep learning on image data and apply feedback to adjust hardware and software imaging parameters before exporting a refined data for analysis. The fact that no microscope with such capabilities exist (nor can exist?) is obvious. This strongly suggests that scientist should learn the art of building and optimising DIY microscopes that would continue to suit research needs, starting from very basic designs. Even in cases where an optimised DIY platform may cost more than commercial systems, there are advantages to it than buying platforms off the shelf every time there is a change in research focus.

SPIM is particularly good for timelapse (3D + time) imaging i.e., supports sample physiology during extended imaging periods such as required to study embryogenesis. It is also a preferred platform as it offers a good balance between being able to image very large sample sizes (~ cm) such as an intact mouse brain and achieving high image resolution. Though openSPIM DIY versions arguably have the most detailed published and widely accepted build instructions, they are more tailored towards in-vivo imaging and are sample specific (only samples that fit within the field of view). In my research, I have further expanded on the openSPIM design in a way that has not previously been done. I have documented stepwise instructions and built a L-openSPIM platform using in-air optics that are more suited to a wider range of samples in-vivo and in-vitro. I have also provided more practical insights into finer light sheet alignment, the choice of image acquisition software, and efficient data acquisition and storage format.

Furthermore, I have shown that the axial and lateral resolution estimates of our microscope experimentally are 4.32 µm and 2.88 µm in contrast to theoretical values 4.07 µm and 0.58 µm, respectively. Though with limited capabilities, I have demonstrated its performance in 3D imaging of a millimetre sized optically opaque *Varroa destructor,* and to distinctively reveal cells of the optically transparent head of a *Hydractinia symbiolongicarpus*. Technically, this should mean our platform can as-is conveniently image up to millimetre sized samples at cellular resolution if the sample is optically transparent (or made to be through solvent clearing) as much as required. Zebrafish *and Drosophila melanogasta* are often imaged as model organisms in their early stages of development in light sheet morphology and functional studies, and their corresponding sizes at such timepoints are within the current range of suitable sample sizes for our SPIM platform.

Hydractinia which is a highly motile animal has also been studied as a model organism in light sheet microscopy for volumetric calcium dynamics, hydrodynamics, neural circuits, and for cellular processes that drive morphogenesis and regeneration (Dupre and Yuste, 2017; B Migliori *et al.*, 2018; Iachetta *et al.*, 2018; Crombez *et al.*, 2022; Hedde *et al.*, 2023). Details needed to extend the microscope capacity to centimetre sized samples at a high isotropic raw image resolution have also been described. With useful upgrades, I can repeat the same studies on our SPIM platform. Indeed, centimetre sized samples (such as an intact adult mouse brains) can be imaged on our platform as shown in Stefaniuk *et al.*, (2016), but at a much better image quality when upgrades to suit research interest are applied (Royer *et al.*, 2016, 2018; Voigt *et al.*, 2020). It is key to mention here that light sheet microscopy due to its high resolution can be included as part of multimodal imaging studies in revealing tissue cytoarchitecture and function with greater specificity (Aswendt *et al.*, 2017; Li *et al.*, 2018, 2019; Dejea *et al.*, 2020; Kapsokalyvas and van Zandvoort, 2020; Hahn *et al.*, 2022; Kyere *et al.*, 2022; Perens *et al.*, 2023).

Several studies on biological tissue have been done using immersion and air optics (objectives), and in both cases have produced phenomenal results (Bianca Migliori *et al.*, 2018; Girkin and Carvalho, 2018; Zagato *et al.*, 2018; Ueda *et al.*, 2020; Voigt *et al.*, 2020; Kim *et al.*, 2021). Immersion objectives collect more fluorescence photon emissions and limit spherical aberrations that might stem from obstacles in the light path (such as the wall of the imaging cuvette). But again, for solvent cleared tissues they are significantly more expensive and buffer (imaging media) specific. Considering that new tissue clearing solvents and clearing techniques are regularly being developed to ensure better optical transparency while preserving tissue structures, compatibility with immersion objectives will always be a technical challenge and an expensive option.

On the other hand, air objectives can be applied to any imaging media and to almost any study to produce reasonable results, especially when there is a need to image several very large samples at cellular resolution. This comes with the addition of axially scanned (for greater interest in spatial resolution) or static light sheet (for greater interest in temporal resolution) in the illumination, and an appropriate zoom lens in the detection, all mounted on translation stages. Though one may argue the cost effectiveness of such setups and degraded image quality versus the use of immersion objectives. For cleared tissue (in-vitro imaging), irrespective of the size, the need to keep changing the immersion objectives when newly developed clearing techniques are used remains. Clearing media used for R.I matching can damage objective lens not specifically designed for it. My goal is not to entirely debunk the usefulness of immersion objectives. For scientists new to the technique, I strongly advise in-vivo imaging of small samples (< 1mm) should be done with high NA water objectives (which are the cheapest and readily available off the shelf) and are mostly employed for such. However, when it comes to imaging larger samples (living or cleared) and sticking to a basic single setup that can be applied across different research and sample sizes, as an initial trial, the use of air optics appears to still be a cost-effective choice to produce reasonable results. Results from such initially basic platform can inform what immersion objective (if needed and commercially available), hardware, and software modules to financially invest in for useful upgrades. Near future direction of light sheet fluorescence microscopy on newer methods for defining the light sheet geometry also suggest the use of air objectives (Kim *et al.*, 2021; Feng and Yin, 2022b, 2022a; Gao, 2022).

Finally, I have also described a protocol for investigating thresholds that limit laser induced heating effects and ensure tissue bio-fidelity. There is a need to consider the effect of laser induced heat which is currently being ignored especially in LSFM drug delivery, embryogenesis, and neurophysiological studies. The protocol I have described in chapter 3 to investigate this for blue light on our microscope can be applied to all laser microscopes to determine maximum exposure levels that ensure tissue bio-fidelity. The general idea is to limit tissue exposure to the barest minimum for a time as little as possible, adopt the use of longer wavelength where possible, and better still model the effect(s) of heat into quantitative studies to further ensure accurate and reproducible results. Experimental results show that for the current L-openSPIM platform I have built, where possible, 10 mW, 20 mW, 30 mW, 40 mW, 50 mW, and 60 mW of laser power should not be applied for more than 26 s, 10 s, 5 s, 4 s, 4 s, and 3 s, to 1 mm^2 of mammal tissue, respectively, to limit temperature rise to ~ $\leq 1^0$C.

References

Aakhte, M., Akhlaghi, E.A. and Müller, H.A.J. (2018) 'SSPIM: A beam shaping toolbox for structured selective plane illumination microscopy', *Scientific Reports*, 8(1), pp. 1–12. Available at: https://doi.org/10.1038/s41598-018-28389-8.

Aravanis, A.M. *et al.* (2007) 'An optical neural interface: in vivo control of rodent motor cortex with integrated fiberoptic and optogenetic technology.', *Journal of neural engineering*, 4(3). Available at: https://doi.org/10.1088/1741-2560/4/3/S02.

Arias-Gil, G. *et al.* (2016) 'Measurement, modeling, and prediction of temperature rise due to optogenetic brain stimulation', *Neurophotonics*, 3(4), p. 045007. Available at: https://doi.org/10.1117/1.nph.3.4.045007.

Aswendt, M. *et al.* (2017) 'Whole-Brain Microscopy Meets In Vivo Neuroimaging: Techniques, Benefits, and Limitations', *Molecular Imaging and Biology*, 19(1), pp. 1–9. Available at: https://doi.org/10.1007/s11307-016-0988-z.

Bassi, A., Schmid, B. and Huisken, J. (2015) 'Optical tomography complements light sheet microscopy for in toto imaging of zebrafish development', *Development*, 142(5), pp. 1016–1020. Available at: https://doi.org/10.1242/dev.116970.

Beicker, K. *et al.* (2018) 'Vertical Light Sheet Enhanced Side-View Imaging for AFM Cell Mechanics Studies', *Scientific Reports*, 8(1), pp. 1–12. Available at: https://doi.org/10.1038/s41598-018-19791-3.

Betzig, E. *et al.* (2006) 'Imaging Intracellular Fluorescent Proteins at Nanometer Resolution.', *Science (Washington, DC, United States)*, 313(5793), pp. 1642–1645. Available at: https://doi.org/10.1126/science.1127344.

Bishop, K., Glaser, A. and Liu, J. (2020) ‘Performance tradeoffs for single- and designs : a simulation-based analysis’, 11(8), pp. 4627–4650.

Bouchard, Matthew B. *et al.* (2015) ‘Swept confocally-aligned planar excitation (SCAPE) microscopy for high-speed volumetric imaging of behaving organisms’, *Nature Photonics*, 9(2), pp. 113–119. Available at: https://doi.org/10.1038/nphoton.2014.323.

Bouchard, M B *et al.* (2015) ‘Swept confocally-aligned planar excitation (SCAPE) microscopy for high-speed volumetric imaging of behaving organisms’, *Nature Photonics*, 9(2), pp. 113–119. Available at: https://doi.org/10.1038/NPHOTON.2014.323.

Brandes, A.R. *et al.* (2014) ‘Modeling the tight focusing of beams in absorbing media with Monte Carlo simulations’, *Journal of Biomedical Optics*, 19(11), p. 115003. Available at: https://doi.org/10.1117/1.JBO.19.11.115003.

Buytaert, J.A.N. and Dirckx, J.J.J. (2007) ‘Design and quantitative resolution measurements of an optical virtual sectioning three-dimensional imaging technique for biomedical specimens, featuring two-micrometer slicing resolution’, *Journal of Biomedical Optics*, 12(1), p. 014039. Available at: https://doi.org/10.1117/1.2671712.

Chakraborty, T. *et al.* (2019) ‘Light-sheet microscopy of cleared tissues with isotropic, subcellular resolution’, *Nature Methods*, 16(11), pp. 1109–1113. Available at: https://doi.org/10.1038/s41592-019-0615-4.

Chen, C.Y. *et al.* (2019) ‘The Applications of Lattice Light-Sheet Microscopy for Functional Volumetric Imaging of Hippocampal Neurons in a Three-Dimensional Culture System’, *Micromachines*, 10(9). Available at: https://doi.org/10.3390/mi10090599 WE - Science Citation Index Expanded (SCI-EXPANDED).

Chen, X. *et al.* (2021) 'Deep-learning on-chip light-sheet microscopy enabling video-rate volumetric imaging of dynamic biological specimens', *Lab on a Chip*, 21(18), pp. 3420–3428. Available at: https://doi.org/10.1039/d1lc00475a.

Chhetri, R.K. *et al.* (2015) 'Whole-animal functional and developmental imaging with isotropic spatial resolution', *Nature Methods*, 12(12), pp. 1171–1178. Available at: https://doi.org/10.1038/nmeth.3632.

Chhetri, R.K. *et al.* (2016) 'Whole-animal imaging with high spatio-temporal resolution', in Tsia, KK and Goda, K (ed.) *High-Speed Biomedical Imaging and Spectroscopy: Toward Big Data Instrumentation and Management*. 1000 20TH ST, PO BOX 10, BELLINGHAM, WA 98227-0010 USA: SPIE-Int Soc Optical Engineering (Proceedings of SPIE). Available at: https://doi.org/10.1117/12.2212564.

Chong, J., Amourda, C. and Saunders, T.E. (2018) 'Temporal development of Drosophila embryos is highly robust across a wide temperature range', *Journal of the Royal Society Interface*, 15(144). Available at: https://doi.org/10.1098/rsif.2018.0304 WE - Science Citation Index Expanded (SCI-EXPANDED).

Christie, I.N. *et al.* (2013) 'FMRI response to blue light delivery in the naïve brain: Implications for combined optogenetic fMRI studies', *NeuroImage*, 66, pp. 634–641. Available at: https://doi.org/10.1016/j.neuroimage.2012.10.074.

Christou, M. *et al.* (2018) 'Segmentation pattern of zebrafish caudal fin is affected by developmental temperature and defined by multiple fusions between segments', *Journal of Experimental Zoology Part B-Molecular and Developmental Evolution*, 330(6–7), pp. 330–340. Available at: https://doi.org/10.1002/jez.b.22825.

Corsetti, S., Gunn-Moore, F. and Dholakia, K. (2019) ‘Light sheet fluorescence microscopy for neuroscience’, *Journal of Neuroscience Methods*, 319(SI), pp. 16–27. Available at: https://doi.org/10.1016/j.jneumeth.2018.07.011.

Crombez, S. *et al.* (2022) ‘Computational hyperspectral light-sheet microscopy’, *Optics Express*, 30(4), pp. 4856–4866. Available at: https://doi.org/10.1364/OE.442043.

Davidson, M.W. (2009) ‘Fluorescence Spectroscopy’, *Labmedicine*, 40(11). Available at: https://doi.org/10.1309/LMYH007ZKFVXFFRC.

Dé Ric Bevilacqua, F. *et al.* (1999) *In vivo local determination of tissue optical properties: applications to human brain*.

Dean, K.M. *et al.* (2021) ‘Isotropic Imaging Across Spatial Scales with Axially Swept Light-Sheet Microscopy’. Available at: https://doi.org/10.5281/ZENODO.5639726.

Dejea, H. *et al.* (2020) ‘Cardiac multi-scale investigation of the right and left ventricle ex vivo: a review’, *Cardiovascular Diagnosis and Therapy*, 10(5), pp. 1701–1717. Available at: https://doi.org/10.21037/cdt-20-269.

Denk, W., Strickler, J. and Webb, W. (1990) ‘Two-photon laser scanning fluorescence microscopy’, *Science*, 248(4951), pp. 73–76. Available at: https://doi.org/10.1126/science.2321027.

Dimitriadi, A. *et al.* (2018) ‘Developmental temperature has persistent, sexually dimorphic effects on zebrafish cardiac anatomy’, *Scientific Reports*, 8. Available at: https://doi.org/10.1038/s41598-018-25991-8.

Djenoune, L. *et al.* (2023) ‘Cilia function as calcium-mediated mechanosensors that instruct left-right asymmetry’, *Science*, 379(6627), pp. 71–77. Available at:

https://doi.org/10.1126/science.abq7317.

Dodt, H.U. *et al.* (2007) ‘Ultramicroscopy: Three-dimensional visualization of neuronal networks in the whole mouse brain’, *Nature Methods*, 4(4), pp. 331–336. Available at: https://doi.org/10.1038/nmeth1036.

Dong, N. *et al.* (2018) ‘Opto-electro-thermal optimization of photonic probes for optogenetic neural stimulation’, *Journal of Biophotonics*, 11(10), pp. 1–17. Available at: https://doi.org/10.1002/jbio.201700358.

Dupre, C. and Yuste, R. (2017) ‘Non-overlapping Neural Networks in Hydra vulgaris’, *Current Biology*, 27(8), pp. 1085–1097. Available at: https://doi.org/10.1016/j.cub.2017.02.049.

Eguchi, K. *et al.* (2020) ‘Advantages of Acute Brain Slices Prepared at Physiological Temperature in the Characterization of Synaptic Functions’, *Frontiers in Cellular Neuroscience*, 14. Available at: https://doi.org/10.3389/fncel.2020.00063.

Elwassif, M.M. *et al.* (2006) ‘Bio-heat transfer model of deep brain stimulation-induced temperature changes’, *Journal of Neural Engineering*, 3(4). Available at: https://doi.org/10.1088/1741-2560/3/4/008.

Engelbrecht, C.J. and Stelzer, E.H.K. (2006) ‘Resolution enhancement in a light-sheet-based microscope (SPIM)’, *Optics Letters*, 31(10), pp. 1477–1479. Available at: https://doi.org/10.1364/OL.31.001477.

Engelbrecht, C.J., Voigt, F. and Helmchen, F. (2010) ‘Miniaturized selective plane illumination microscopy for high-contrast in vivo fluorescence imaging’, *Optics Letters*, 35(9), pp. 1413–1415. Available at: https://doi.org/10.1364/OL.35.001413.

Fahrbach, F.O. and Rohrbach, A. (2010) ‘A line scanned light-sheet microscope with phase shaped self-reconstructing beams’, *Optics Express*, 18(23), pp. 2608–2610. Available at: https://doi.org/10.1038/nphoton.2010.204.J.

Feng, Y. and Yin, M. (2022a) ‘High-resolution tiled light-sheet microscope has triangular prism system that can split light beam into left and right light beams, and left and right light beams that can respectively enter left light-emitting system and right light-emitting system in on’.

Feng, Y. and Yin, M. (2022b) ‘Table-type flat tile fluorescent microscope for fast and high resolution three-dimensional fluorescence imaging of transparent large tissue, in which fluorescence generated by left and right beams irradiating sample reaches camera through objective lens’,.

Fiala, J.C. and Harris, K.M. (1999) *Dendrite structure*. Oxford University Press. Available at: https://synapseweb.clm.utexas.edu/sites/default/files/synapseweb/files/1999_dendrites_fiala_harris_dendrite_structure.pdf (Accessed: 18 May 2022).

Flood, P.. *et al.* (2013) ‘White Paper: Sample Preparation for Light Sheet Microscope’, *Protocols and Guidelines for ZEISS Lightsheet Z.1*, pp. 1–34. Available at: http://microscopy.zeiss.com/microscopy/en_de/products/imaging-systems/lightsheet-z-1.html#Introduction.

Follain, G. *et al.* (2017) ‘Seeing is believing - multi-scale spatio-temporal imaging towards invivo cell biology’, *Journal of Cell Science*, 130(1, SI), pp. 23–38. Available at: https://doi.org/10.1242/jcs.189001.

Gagliano, G. *et al.* (2021) ‘Light Sheet Illumination for 3D Single-Molecule Super-

Resolution Imaging of Neuronal Synapses', *Frontiers in Synaptic Neuroscience*, 13(November), pp. 1–21. Available at: https://doi.org/10.3389/fnsyn.2021.761530.

Galland, R. *et al.* (2015) '3D high- and super-resolution imaging using single-objective SPIM', *Nature Methods*, 12(7), p. 641+. Available at: https://doi.org/10.1038/NMETH.3402.

Gao, L. *et al.* (2014) '3D live fluorescence imaging of cellular dynamics using Bessel beam plane illumination microscopy', *Nature Protocols*, 9(5), pp. 1083–1101. Available at: https://doi.org/10.1038/nprot.2014.087.

Gao, L. (2022) 'Tiled light sheet microscope, has vibration mirror for guiding illumination light onto illumination path on side of imaging chamber by deflecting galvanometer angle, and excitation objective spaced from imaging'.

Garini, Y., Vermolen, B.J. and Young, I.T. (2005) 'From micro to nano: recent advances in high-resolution microscopy', *Current Opinion in Biotechnology*, 16(1), pp. 3–12. Available at: https://doi.org/https://doi.org/10.1016/j.copbio.2005.01.003.

Gebhardt, J.C.M. *et al.* (2013) 'Single-molecule imaging of transcription factor binding to DNA in live mammalian cells', *Nature Methods*, 10(5), pp. 421–426. Available at: https://doi.org/10.1038/nmeth.2411.

Girkin, J.M. and Carvalho, M.T. (2018) 'The light-sheet microscopy revolution', *JOURNAL OF OPTICS*, 20(5). Available at: https://doi.org/10.1088/2040-8986/aab58a.

Girstmair, J. *et al.* (2016) 'Light-sheet microscopy for everyone? Experience of building an OpenSPIM to study flatworm development', *BMC Developmental Biology*, 16. Available at: https://doi.org/10.1186/s12861-016-0122-0.

Girstmair, J. *et al.* (2022a) 'OpenSPIM - alignment guide'. Available at:

https://openspim.org/xopenspim/alignment_welcome.

Girstmair, J. *et al.* (2022b) ‘Time to Upgrade: A New OpenSPIM Guide to Build and Operate Advanced OpenSPIM Configurations’, *Advanced Biology*, 6(4), p. 2101182. Available at: https://doi.org/10.1002/ADBI.202101182.

Glaser, A. *et al.* (2017) ‘Light-sheet microscopy for slide-free non-destructive pathology of large clinical specimens’, *Nature Biomedical Engineering*, 1, p. 0084. Available at: https://doi.org/https://doi.org/10.1038/s41551-017-0084.

Glaser, A.K. *et al.* (2019) ‘Multi-immersion open-top light-sheet microscope for high-throughput imaging of cleared tissues’, *Nature Communications*, 10(1), pp. 1–8. Available at: https://doi.org/10.1038/s41467-019-10534-0.

Goodwin, P.C. (2014) ‘Quantitative deconvolution microscopy’, *Methods in Cell Biology*, 123, pp. 177–192. Available at: https://doi.org/10.1016/B978-0-12-420138-5.00010-0.

Greger, K., Swoger, J. and Stelzer, E.H.K. (2007) ‘Basic building units and properties of a fluorescence single plane illumination microscope’, *Review of Scientific Instruments*, 78(2), pp. 0237051–0237057. Available at: https://doi.org/10.1063/1.2428277.

Gualda, E.J. *et al.* (2013) ‘OpenSpinMicroscopy: an open-source integrated microscopy platform’, *Nature Methods*, 10(7), pp. 599–600. Available at: https://doi.org/10.1038/nmeth.2508.

Gustafsson, M.G.L. *et al.* (2008) ‘Three-Dimensional Resolution Doubling in Wide-Field Fluorescence Microscopy by Structured Illumination’, *Biophysical Journal*, 94(12), pp. 4957–4970. Available at: https://doi.org/10.1529/BIOPHYSJ.107.120345.

Gustavsson, A.-K., Petrov, P.N. and Moerner, W.E. (2018) ‘Light sheet approaches for improved precision in 3D localization-based super-resolution imaging in mammalian cells [Invited]', *Optics Express*, 26(10), p. 13122. Available at: https://doi.org/10.1364/oe.26.013122.

Hahn, A. *et al.* (2022) 'Brain tumor classification of virtual NMR voxels based on realistic blood vessel-induced spin dephasing using support vector machines', *NMR IN Biomedicine*, 35(4). Available at: https://doi.org/10.1002/nbm.4307.

Han, X. *et al.* (2021) 'A polymer index-matched to water enables diverse applications in fluorescence microscopy', *LAB ON A CHIP*, 21(8), pp. 1549–1562. Available at: https://doi.org/10.1039/d0lc01233e.

HATA, M. *et al.* (1994) 'Multiple Functions Of RAF Protooncogene During Development From Analysis of a Temperature-Sensitive Mutation of Drosophila', *International Journal Of Developmental Biology*, 38(2), pp. 329-335 WE-Science Citation Index Expanded (SCI.

Hedde, P.N. *et al.* (2023) 'SPIM-Flow: An Integrated Light Sheet and Microfluidics Platform for Hydrodynamic Studies of Hydra', *Biology-Basel*, 12(1). Available at: https://doi.org/10.3390/biology12010116.

Heilemann, M. *et al.* (2005) 'Carbocyanine Dyes as Efficient Reversible Single-Molecule Optical Switch', *Journal of American Chemical Society*, 127(11), pp. 3801–3806. Available at: https://doi.org/10.1021/ja044686x.

Heilemann, M. *et al.* (2008) 'Subdiffraction-Resolution Fluorescence Imaging with Conventional Fluorescent Probes', *Angewandte Chemie International Edition*, 47(33), pp. 6172–6176. Available at: https://doi.org/10.1002/anie.200802376.

Helmchen, F. and Denk, W. (2005a) 'Deep tissue two-photon microscopy', *Nature Methods*, 2(12), pp. 932–940. Available at: https://doi.org/10.1038/nmeth818.

Helmchen, F. and Denk, W. (2005b) ‘Deep tissue two-photon microscopy’, *Nature Methods*, 2(12), pp. 932–940. Available at: https://doi.org/10.1038/nmeth818.

Hess, S.T., Girirajan, T.P.K. and Mason, M.D. (2006a) ‘Ultra-high resolution imaging by fluorescence photoactivation localization microscopy’, *Biophysical Journal*, 91(11), pp. 4258–4272. Available at: https://doi.org/10.1529/biophysj.106.091116.

Hess, S.T., Girirajan, T.P.K. and Mason, M.D. (2006b) ‘Ultra-High Resolution Imaging by Fluorescence Photoactivation Localization Microscopy’, *Biophysical Journal*, 91(11), pp. 4258–4272. Available at: https://doi.org/10.1529/BIOPHYSJ.106.091116.

Holekamp, T.F., Turaga, D. and Holy, T.E. (2008) ‘Fast Three-Dimensional Fluorescence Imaging of Activity in Neural Populations by Objective-Coupled Planar Illumination Microscopy’, *Neuron*, 57(5), pp. 661–672. Available at: https://doi.org/10.1016/J.NEURON.2008.01.011.

Hörl, D. *et al.* (2018) ‘BigStitcher: Reconstructing high-resolution image datasets of cleared and expanded samples’, *bioRxiv*, pp. 1–12. Available at: https://doi.org/10.1101/343954.

Hu, Y.S. *et al.* (2013) ‘Light-sheet Bayesian microscopy enables deepcell super-resolution imaging of heterochromatin in live human embryonic stem cells’, *Optical Nanoscopy*, 2(1), pp. 1–12. Available at: https://doi.org/10.1186/2192-2853-2-7.

Hu, Y.S. *et al.* (2014) ‘Single-Molecule Super-Resolution Light-Sheet Microscopy’, *Chemphyschem*, 15(4, SI), pp. 577–586. Available at: https://doi.org/10.1002/cphc.201300732.

Huisken, J. *et al.* (2004) ‘Optical sectioning deep inside live embryos by selective plane illumination microscopy', *Science*, 305(5686), pp. 1007–1009. Available at: https://doi.org/10.1126/science.1100035.

Huisken, J. (2012) 'Slicing embryos gently with laser light sheets', *BioEssays*, 34(5), pp. 406–411. Available at: https://doi.org/10.1002/bies.201100120.

Huisken, J. and Stainier, D.Y.R. (2007) 'Even fluorescence excitation by multidirectional selective plane illumination microscopy (mSPIM)', *Optics Letters*, 32(17), pp. 2608–2610. Available at: https://doi.org/10.1364/OL.32.002608.

Huisken, J. and Stainier, Didier Y R (2009) 'Selective plane illumination microscopy techniques in developmental biology', *Development*, 136(12), pp. 1963–1975. Available at: https://doi.org/10.1242/dev.022426.

Huisken, J. and Stainier, Didier Y.R. (2009) 'Selective plane illumination microscopy techniques in developmental biology', *Development*, pp. 1963–1975. Available at: https://doi.org/10.1242/dev.022426.

Iachetta, R. *et al.* (2018) 'Real time dynamics of beta-catenin expression during Hydra development, regeneration and Wnt signalling activation', *International Journal of Developmental Biology*, 62(4–5), pp. 311–318. Available at: https://doi.org/10.1387/ijdb.180092ct.

Icha, J. *et al.* (2016) 'Using Light Sheet Fluorescence Microscopy to Image Zebrafish Eye Development', *Jove-Journal of Visualized Experiments* [Preprint], (110). Available at: https://doi.org/10.3791/53966.

Jalal, M., Andersen, T. and Hessen, D.O. (2015) 'Temperature and developmental responses of body and cell size in Drosophila; effects of polyploidy and genome configuration', *Journal* *of Thermal Biology*, 51, pp. 1–14. Available at: https://doi.org/10.1016/j.jtherbio.2015.02.011 WE - Science Citation Index Expanded (SCI-EXPANDED).

Janesick, J.R. (2007) *Photon Transfer*. Bellingham, WA: SPIE Press. Available at: https://books.google.ie/books?hl=en&lr=&id=4IuH7FtVz90C&oi=fnd&pg=PR11&dq=Janesick,+J.+R.+(2007).+&ots=AGGmxwyxTV&sig=009cDzp3tkzt89eecu5nj2RXWsg&redir_esc=y#v=onepage&q&f=false (Accessed: 4 June 2021).

Janssen, F.E.M., Van Leeuwen, G.M.J. and Van Steenhoven, A.A. (2005) 'Modelling of temperature and perfusion during scalp cooling', *Physics in Medicine and Biology*, 50(17), pp. 4065–4073. Available at: https://doi.org/10.1088/0031-9155/50/17/010.

Kapsokalyvas, D. and van Zandvoort, M.A.M.J. (2020) 'Molecular Imaging in Oncology: Advanced Microscopy Techniques.', *Recent results in cancer research. Fortschritte der Krebsforschung. Progres dans les recherches sur le cancer*, 216, pp. 533–561. Available at: https://doi.org/10.1007/978-3-030-42618-7_16.

Karadas, M. *et al.* (2021) 'In-vitro Recordings of Neural Magnetic Activity From the Auditory Brainstem Using Color Centers in Diamond: A Simulation Study', *Frontiers in Neuroscience*, 15(May), pp. 1–17. Available at: https://doi.org/10.3389/fnins.2021.643614.

Kaufmann, A. *et al.* (2012) 'Multilayer mounting enables long-term imaging of zebrafish development in a light sheet microscope', *Development*, 139(17), pp. 3242–3247. Available at: https://doi.org/10.1242/dev.082586.

Keller, P.J. *et al.* (2008) 'Reconstruction of Zebrafish Early Embryonic Development by Scanned Light Sheet Microscopy', *Science (New York, N.Y.)*, 322(November), pp. 1065–1069. Available at: https://doi.org/10.1126/science.1162493.

Keller, P.J. *et al.* (2010) 'Fast, high-contrast imaging of animal development with scanned light sheet–based structured-illumination microscopy', *Nature Methods*, 7(8), pp. 637–642. Available at: https://doi.org/10.1038/nmeth.1476.

Keller, P.J. *et al.* (2011) 'Digital scanned laser light-sheet fluorescence microscopy (DSLM) of zebrafish and drosophila embryonic development', *Cold Spring Harbor Protocols*, 6(10), pp. 1235–1243. Available at: https://doi.org/10.1101/pdb.prot065839.

Keller, P.J. and Stelzer, E.H.K. (2008) 'Quantitative in vivo imaging of entire embryos with Digital Scanned Laser Light Sheet Fluorescence Microscopy', *Current Opinion in Neurobiology*, 18(6), pp. 624–632. Available at: https://doi.org/https://doi.org/10.1016/j.conb.2009.03.008.

Kim, B. *et al.* (2021) 'Open-top axially swept light-sheet microscopy', *Biomedical Optics Express*, 12(4), pp. 2328–2338. Available at: https://doi.org/10.1364/BOE.419030.

Klar, T.A. *et al.* (2000) 'Fluorescence microscopy with diffraction resolution barrier broken by stimulated emission.', *Proceedings of the National Academy of Sciences of the United States of America*, 97(15), pp. 8206–10. Available at: https://doi.org/10.1073/PNAS.97.15.8206.

Kobat, D., Horton, N.G. and Xu, C. (2011) 'In vivo two-photon microscopy to 1.6-mm depth in mouse cortex', *Journal of Biomedical Optics*, 16(10), p. 106014. Available at: https://doi.org/10.1117/1.3646209.

Kumar, S. *et al.* (2011) 'Optically Sectioned Imaging by Oblique Plane Microscopy', in Conchello, JA and Cogswell, CJ and Wilson, T and Brown, TG (ed.) *Three-Dimensional and Multidimensional Microscopy: Image Acquisition and Processing XVIII*. 1000 20TH ST, PO

Box 10, Bellingham, WA 98227-0010 USA: SPIE-Int Soc Optical Engineering (Proceedings of SPIE). Available at: https://doi.org/10.1117/12.873471.

Kuntz, S.G. and Eisen, M.B. (2014) ‘Drosophila Embryogenesis Scales Uniformly across Temperature in Developmentally Diverse Species’, *Plos Genetics*, 10(4). Available at: https://doi.org/10.1371/journal.pgen.1004293 WE - Science Citation Index Expanded (SCI-EXPANDED).

Kyere, F.A. *et al.* (2022) ‘Whole-Brain Single-Cell Imaging and Analysis of Intact Neonatal Mouse Brains Using MRI, Tissue Clearing, and Light-Sheet Microscopy’, *Jove-Journal Of Visualized Experiments* [Preprint], (186). Available at: https://doi.org/10.3791/64096.

Lakowicz, J.R. (2006) *Principles of Fluorescence Spectroscopy*. 3rd edn. New York: Springer Science+Business. Available at: https://www.academia.edu/34533342/Principles_of_Fluorescence_Spectroscopy_Third_Edition (Accessed: 10 May 2021).

Lambert, T.J. and Waters, J.C. (2014) ‘Assessing camera performance for quantitative microscopy’, *Methods in Cell Biology*, 123, pp. 35–53. Available at: https://doi.org/10.1016/B978-0-12-420138-5.00003-3.

Lemon, W.C. *et al.* (2015) ‘Whole-central nervous system functional imaging in larval Drosophila’, *Nature Communications*, 6. Available at: https://doi.org/10.1038/ncomms8924.

Lemon, W.C. and McDole, K. (2020) ‘Live-cell imaging in the era of too many microscopes’, *Current Opinion in Cell Biology*, 66, pp. 34–42. Available at: https://doi.org/10.1016/j.ceb.2020.04.008.

Li, T. *et al.* (2018) ‘Hybrid of two-photon microscopy and optical multimodality imaging for multi-scale imaging of small animals', *Three-Dimensional and Multidimensional Microscopy: Image Acquisition and Processing XXV*. Edited by T.G. Brown, C.J. Cogswell, and T. Wilson. Available at: https://doi.org/10.1117/12.2291293.

Li, T. *et al.* (2019) 'Multiscale imaging of colitis in mice using confocal laser endomicroscopy, light-sheet fluorescence microscopy, and magnetic resonance imaging', *Journal of Biomedical Optics*, 24(1). Available at: https://doi.org/10.1117/1.JBO.24.1.016003.

Liang, X., Holy, T.E. and Taghert, P.H. (2022) 'Circadian pacemaker neurons display cophasic rhythms in basal calcium level and in fast calcium fluctuations', *Proceedings of the National Academy of Sciences of The United States Of America*, 119(17). Available at: https://doi.org/10.1073/pnas.2109969119.

Lichtman, J.W. and Conchello, J.-A. (2005) 'Fluorescence microscopy', *Nature Methods*, 2(12), pp. 910–919. Available at: https://doi.org/10.1038/NMETH817.

Lin, H.-C.A. *et al.* (2015) 'Selective plane illumination optical and optoacoustic microscopy for postembryonic imaging', *Laser & Photonics Reviews*, 9(5), pp. L29–L34. Available at: https://doi.org/10.1002/lpor.201500120.

Lorenzo, C. *et al.* (2011) 'Live cell division dynamics monitoring in 3D large spheroid tumor models using light sheet microscopy', *Cell Division*, 6. Available at: https://doi.org/10.1186/1747-1028-6-22.

Lorenzo, C. (2012) *Build Your Own Spim - DIY*. Available at: http://www.ip3d.fr/IP3D/SPIM/Entrees/2012/4/20_Do_It_Yourself_-_Build_your_own_SPIM_!.html (Accessed: 12 April 2018).

Lucchetta, E.M., Munson, M.S. and Ismagilov, R.F. (2006) ‘Characterization of the local temperature in space and time around a developing Drosophila embryo in a microfluidic device’, *Lab on a Chip*, 6(2), pp. 185–190. Available at: https://doi.org/10.1039/b516119c WE - Science Citation Index Expanded (SCI-EXPANDED).

Marx, V. (2016) ‘Microscopy: OpenSPIM 2.0’, *Nature Methods*, 13(12), pp. 979–982. Available at: https://doi.org/10.1038/nmeth.4070.

Mayer, J. *et al.* (2014) ‘OPTiSPIM: integrating optical projection tomography in light sheet microscopy extends specimen characterization to nonfluorescent contrasts’, *Optics Letters*, 39(4), pp. 1053–1056. Available at: https://doi.org/10.1364/OL.39.001053.

McGlynn, E. *et al.* (2021) ‘The Future of Neuroscience: Flexible and Wireless Implantable Neural Electronics’, *Advanced Science*, 8(10), pp. 1–33. Available at: https://doi.org/10.1002/advs.202002693.

McGorty, R. *et al.* (2015) ‘Open-top selective plane illumination microscope for conventionally mounted specimens’, *Optics Express*, 23(12), pp. 16142–16153. Available at: https://doi.org/10.1364/OE.23.016142.

Micro-Manager (2021) ‘Micro-Manager’. Available at: https://micro-manager.org/Download_Micro-Manager_Latest_Release.

Micro-Manager, U.G. (2012) ‘Micro-Manager User’s Guide’. Available at: https://micro-manager.org/Micro-Manager_User’s_Guide.

Migliori, Bianca *et al.* (2018) ‘Light sheet theta microscopy for rapid high-resolution imaging of large biological samples’, *BMC Biology*, 16(1), pp. 1–20. Available at: https://doi.org/10.1186/s12915-018-0521-8.

Migliori, B *et al.* (2018) ‘Light sheet theta microscopy for rapid high-resolution imaging of large biological samples’, *BMC Biology,* 16. Available at: https://doi.org/10.1186/s12915-018-0521-8.

Mitchell, N.P. *et al.* (2022) ‘Visceral organ morphogenesis via calcium-patterned muscle constrictions’, *Elife,* 11. Available at: https://doi.org/10.7554/eLife.77355.

National Tsing Hua University (no date) ‘Resolution is the ability to discern fine details’. Available at: https://webmail.life.nthu.edu.tw/~g874215/confocall/NA.htm.

Owens, B. (2017) ‘The microscope makers’, *Nature News,* 551, pp. 659–662. Available at: https://doi.org/10.1038/d41586-017-07528-7.

Parra-Damas, A. and Saura, C.A. (2020) ‘Tissue Clearing and Expansion Methods for Imaging Brain Pathology in Neurodegeneration: From Circuits to Synapses and Beyond’, *Frontiers in Neuroscience,* 14(October). Available at: https://doi.org/10.3389/fnins.2020.00914.

Pawley, J.B. (2006) *More than you ever wanted to know about epistemic*. Third, *Handbook of Biological Confocal Microscopy*. Third. Springer.

Peixoto, H.M. *et al.* (2020) ‘Modeling the Effect of Temperature on Membrane Response of Light Stimulation in Optogenetically-Targeted Neurons’, *Frontiers in Computational Neuroscience*, 14(February), pp. 1–14. Available at: https://doi.org/10.3389/fncom.2020.00005.

Perens, J. *et al.* (2023) ‘Multimodal 3D Mouse Brain Atlas Framework with the Skull-Derived Coordinate System’, *Neuroinformatics* [Preprint]. Available at: https://doi.org/10.1007/s12021-023-09623-9.

Picot, A. *et al.* (2018) ‘Temperature Rise under Two-Photon Optogenetic Brain Stimulation’, *Cell Reports*, 24(5), pp. 1243-1253.e5. Available at: https://doi.org/10.1016/j.celrep.2018.06.119.

Pietzsch, T. *et al.* (2015) ‘BigDataViewer: Visualization and processing for large image data sets’, *Nature Methods*, 12(6), pp. 481–483. Available at: https://doi.org/10.1038/nmeth.3392.

Pitrone, P.G. *et al.* (2013a) ‘OpenSPIM: an open-access light-sheet microscopy platform’, *Nature Methods*, 10(7), pp. 598–599. Available at: https://doi.org/10.1038/nmeth.2507.

Pitrone, P.G. *et al.* (2013b) ‘OpenSPIM’. Available at: https://openspim.org/.

Pitrone, P.G. *et al.* (2013c) ‘OpenSPIM - Assemble Purchased Components’. Available at: https://openspim.org/Assemble_purchased_components.

Pitrone, P.G. *et al.* (2013d) ‘OpenSPIM - Basic requirements for OpenSPIM image processing’. Available at: https://openspim.org/Pre-requisites.

Pitrone, P.G. *et al.* (2013e) ‘OpenSPIM - Configuring µManager for µOpenSPIM’. Available at: https://openspim.org/micro-openspim_micromanager-configuration.

Pitrone, P.G. *et al.* (2013f) ‘OpenSPIM - Installing assembled ThorLabs components on rail carriers’. Available at: https://openspim.org/Install_assembled_ThorLabs_components_on_rail_carriers.

Pitrone, P.G. *et al.* (2013g) ‘OpenSPIM - Installing detection axis on the optical breadboard’. Available at: https://openspim.org/Install_detection_axis_on_the_optical_breadboard#Assembly_of_detection_axis.

Pitrone, P.G. *et al.* (2013h) ‘OpenSPIM - Installing illumination axis’. Available at: https://openspim.org/Install_illumination_axis_on_the_optical_breadboard_-_Part_2#Install_the_cylindrical_lens_in_it’s_proper_place.

Pitrone, P.G. *et al.* (2013i) ‘OpenSPIM - Light Sheet Calibration’. Available at: https://openspim.org/Light-sheet_Calibration.

Pitrone, P.G. *et al.* (2013j) ‘OpenSPIM - Light Sheet Characterization’. Available at: https://openspim.org/Light_sheet_characterization.

Pitrone, P.G. *et al.* (2013k) ‘OpenSPIM - Microscope Operation’. Available at: https://openspim.org/Operation.

Pitrone, P.G. *et al.* (2013l) ‘OpenSPIM - SPIM Optics 101’. Available at: https://openspim.org/SPIM_Optics_101.

Pitrone, P.G. *et al.* (2013m) ‘OpenSPIM - SPIM Optics 101 Practical Hints’. Available at: https://openspim.org/SPIM_Optics_101_Practical_Hints.

Planchon, T.A. *et al.* (2011) ‘Bessel beam plane illumination’, *Nature Methods*, 8(5), pp. 417–423. Available at: https://doi.org/10.1038/nmeth.1586.Rapid.

Podgorski, K. and Ranganathan, G. (2016) ‘Brain heating induced by near-infrared lasers during multiphoton microscopy’, *Journal of Neurophysiology*, 116(3), pp. 1012–1023. Available at: https://doi.org/10.1152/jn.00275.2016.

Ponjavic, A. *et al.* (2018) ‘Single-Molecule Light-Sheet Imaging of Suspended T Cells’, *Biophysical Journal*, 114(9), pp. 2200–2211. Available at: https://doi.org/10.1016/j.bpj.2018.02.044.

Preibisch, Stephan *et al.* (2008) 'Mosaicing of single plane illumination microscopy images using groupwise registration and fast content-based image fusion', in Reinhardt, JM and Pluim, JPW (ed.) *Medical Imaging 2008: Image Processing, PTS 1-3*. 1000 20TH ST, PO BOX 10, Bellingham, WA 98227-0010 USA: SPIE-Int Soc Optical Engineering (Proceedings of SPIE). Available at: https://doi.org/10.1117/12.770893.

Preibisch, S *et al.* (2008) 'Towards digital representation of drosophila embryogenesis', in *2008 IEEE International Symposium on Biomedical Imaging: From Nano to Macro, Vols 1-4*. 345 E 47TH ST, New York, NY 10017 USA: IEEE (IEEE International Symposium on Biomedical Imaging), p. 324+. Available at: https://doi.org/10.1109/ISBI.2008.4540998.

Preibisch, S. *et al.* (2010) 'Software for bead-based registration of selective plane illumination microscopy data', *Nature Methods*, 7(6), pp. 418–419. Available at: https://doi.org/10.1038/nmeth0610-418.

Preibisch, S. *et al.* (2014) 'Efficient bayesian-based multiview deconvolution', *Nature Methods*, 11(6), pp. 645–648. Available at: https://doi.org/10.1038/nmeth.2929.

Preibisch, S. (2015a) 'GitHub - Fourier Convolution CUDA Library'. Available at: https://github.com/StephanPreibisch/FourierConvolutionCUDALib.

Preibisch, S. (2015b) 'GitHub - Separable Convolution CUDA Library'. Available at: https://github.com/StephanPreibisch/SeparableConvolutionCUDALib.

Rasnik, I. *et al.* (2007) 'Electronic Cameras for Low-Light Microscopy', *Methods in Cell Biology*, 81(06), pp. 219–249. Available at: https://doi.org/10.1016/S0091-679X(06)81012-5.

Rebollo, E. *et al.* (2014) 'Live imaging in Drosophila: The optical and genetic toolkits', *Methods*, 68(1), pp. 48–59. Available at:

https://doi.org/https://doi.org/10.1016/j.ymeth.2014.04.021.

Rego, E.H. *et al.* (2012) ‘Nonlinear structured-illumination microscopy with a photoswitchable protein reveals cellular structures at 50-nm resolution.’, *Proceedings of the National Academy of Sciences of the United States of America*, 109(3), pp. E135-43. Available at: https://doi.org/10.1073/pnas.1107547108.

Reynaud, E.G. *et al.* (2008) ‘Light sheet-based fluorescence microscopy: more dimensions, more photons, and less photodamage’, *HFSP Journal*, 2(5), pp. 266–275. Available at: https://doi.org/10.2976/1.2974980.

Royer, L.A. *et al.* (2016) ‘Adaptive light-sheet microscopy for long-term, high-resolution imaging in living organisms’, *Nature Biotechnology*, 34(12), pp. 1267–1278. Available at: https://doi.org/10.1038/nbt.3708.

Royer, L.A. *et al.* (2018) ‘A practical guide to adaptive light-sheet microscopy’, *Nature Protocols*, 13(11), pp. 2462–2500. Available at: https://doi.org/10.1038/s41596-018-0043-4.

Rust, M.J., Bates, M. and Zhuang, X. (2006) ‘Sub-diffraction-limit imaging by stochastic optical reconstruction microscopy (STORM)’, *Nature Methods*, 3(10), pp. 793–796. Available at: https://doi.org/10.1038/nmeth929.

Saliani, A. *et al.* (2017) ‘Axon and Myelin Morphology in Animal and Human Spinal Cord’, *Frontiers in Neuroanatomy*, 11, p. 129. Available at: https://doi.org/10.3389/FNANA.2017.00129.

Schaefer, L.H., Schuster, D. and Schaffer, J. (2004) ‘Structured illumination microscopy: artefact analysis and reduction utilizing a parameter optimization approach’, *Journal of Microscopy*, 216(2), pp. 165–174. Available at: https://doi.org/10.1111/j.0022-

2720.2004.01411.x.

Schermelleh, L. *et al.* (2008) ‘Subdiffraction Multicolor Imaging of the Nuclear Periphery with 3D Structured Illumination Microscopy’, *Science*, 320, pp. 1332–1336. Available at: https://doi.org/10.1126/science.1156947.

Scherz, P.J. *et al.* (2008) ‘High-speed imaging of developing heart valves reveals interplay of morphogenesis and function’, *Development*, 135(6), pp. 1179–1187. Available at: https://doi.org/10.1242/dev.010694.

Schmid, B. and Huisken, J. (2015) ‘Real-time multi-view deconvolution’, *Bioinformatics*, 31(20), pp. 3398–3400. Available at: https://doi.org/10.1093/bioinformatics/btv387.

Schneider, J. *et al.* (2015) ‘Ultrafast, temporally stochastic STED nanoscopy of millisecond dynamics’, *Nature Methods*, 12(9), pp. 827–830. Available at: https://doi.org/10.1038/nmeth.3481.

Senova, S. *et al.* (2017) ‘Experimental assessment of the safety and potential efficacy of high irradiance photostimulation of brain tissues’, *Scientific reports*, 7(February), p. 43997. Available at: https://doi.org/10.1038/srep43997.

Shah, G., Weber, M. and Huisken, J. (2017) *Light Sheet Microscopy*. John Wiley & Sons.

Sheppard, C.J.R. *et al.* (2006) ‘Signal-to-noise ratio in confocal microscopes’, *Handbook of Biological Confocal Microscopy: Third Edition*, pp. 442–452. Available at: https://doi.org/10.1007/978-0-387-45524-2_22.

Shin, Y. *et al.* (2016) ‘Characterization of fiber-optic light delivery and light-induced temperature changes in a rodent brain for precise optogenetic neuromodulation’, *Biomedical Optics Express*, 7(11), p. 4450. Available at: https://doi.org/10.1364/boe.7.004450.

Siedentopf, H. and Zsigmondy, R. (1902) 'Annalen der phyxik.', *Annalen der Physik*, 315(1), pp. 1–39.

Silic, M.R. *et al.* (2022) 'Zebrafish Embryos Display Characteristic Bioelectric Signals during Early Development', *Cells*, 11(22). Available at: https://doi.org/10.3390/cells11223586.

Simpson, J.H. and Looger, L.L. (2018) 'Functional Imaging and Optogenetics in Drosophila', *Genetics*, 208(4), pp. 1291–1309. Available at: https://doi.org/10.1534/genetics.117.300228.

Song, A. (2019) 'Large-scale volumetric in vivo two photon calcium imaging', (September).

Stefaniuk, M. *et al.* (2016) 'Light-sheet microscopy imaging of a whole cleared rat brain with Thy1-GFP transgene', *Scientific Reports*, 6, pp. 1–9. Available at: https://doi.org/10.1038/srep28209.

Stelzer, E.H.K. *et al.* (2021) 'Light sheet fluorescence microscopy', *Nature Reviews Methods Primers 2021 1:1*, 1(1), pp. 1–25. Available at: https://doi.org/10.1038/s43586-021-00069-4.

Stujenske, J.M., Spellman, T. and Gordon, J.A. (2015) 'Modeling the Spatiotemporal Dynamics of Light and Heat Propagation for InVivo Optogenetics', *Cell Reports*, 12(3), pp. 525–534. Available at: https://doi.org/10.1016/j.celrep.2015.06.036.

Swoger, J., Huisken, J. and Stelzer, E.H.K. (2003) 'Multiple imaging axis microscopy improves resolution for thick-sample applications', *Optics Letters*, 28(18), p. 1654. Available at: https://doi.org/10.1364/OL.28.001654.

Takanezawa, S., Saitou, T. and Imamura, T. (2021) 'Wide field light-sheet microscopy with lens-axicon controlled two-photon Bessel beam illumination', *Nature Communications*, 12(1). Available at: https://doi.org/10.1038/s41467-021-23249-y.

Theer, P., Hasan, M.T. and Denk, W. (2003) ‘Two-photon imaging to a depth of 1000 µm in living brains by use of a Ti:Al_2O_3 regenerative amplifier’, *Optics Letters*, 28(12), p. 1022. Available at: https://doi.org/10.1364/OL.28.001022.

ThermoFisher Scientific (2018) ‘Fluorescence SpectraViewer’. Available at: https://www.thermofisher.com/ie/en/home/life-science/cell-analysis/labeling-chemistry/fluorescence-spectraviewer.html (Accessed: 3 April 2018).

Thorlabs (2022) *Shearing Interferometer*. Available at: https://www.thorlabs.com/newgrouppage9.cfm?objectgroup_id=2970.

Tokunaga, M. *et al.* (1997) ‘Single molecule imaging of fluorophores and enzymatic reactions achieved by objective-type total internal reflection fluorescence microscopy’, *Biochemical and Biophysical Research Communications*, 235(1), pp. 47–53. Available at: https://doi.org/10.1006/bbrc.1997.6732.

Tokunaga, M., Imamoto, N. and Sakata-Sogawa, K. (2008) ‘Highly inclined thin illumination enables clear single-molecule imaging in cells’, *Nature Methods*, 5(2), pp. 159–161. Available at: https://doi.org/10.1038/nmeth1171.

Tomer, R. *et al.* (2012) ‘Quantitative high-speed imaging of entire developing embryos with simultaneous multiview light-sheet microscopy’, *Nature Methods*, 9(7), pp. 755–763. Available at: https://doi.org/10.1038/nmeth.2062.

Turrini, L. *et al.* (2022) ‘Multimodal Characterization of Seizures in Zebrafish Larvae’, *Biomedicines*, 10(5). Available at: https://doi.org/10.3390/biomedicines10050951.

Ueda, H.R. *et al.* (2020) ‘Whole-Brain Profiling of Cells and Circuits in Mammals by Tissue Clearing and Light-Sheet Microscopy’, *Neuron*, 106(3), pp. 369–387. Available at:

https://doi.org/10.1016/j.neuron.2020.03.004.

Urushibata, H. *et al.* (2021) 'Control of Developmental Speed in Zebrafish Embryos Using Different Incubation Temperatures', *Zebrafish*, 18(5), pp. 316–325. Available at: https://doi.org/10.1089/zeb.2021.0022.

Valeur, B. and Berberan-Santos, M.N. (2012) *Molecular Fluorescence : Principles and Applications*. 2nd edn. Weinheim, Germany: Wiley-VCH. Available at: https://ebookcentral.proquest.com/lib/nuig/detail.action?docID=1161964 (Accessed: 16 April 2021).

Verveer, P.J. *et al.* (2007) 'High-resolution three-dimensional imaging of large specimens with light sheet-based microscopy', *Nature Methods*, 4(4), pp. 311–313. Available at: https://doi.org/10.1038/nmeth1017.

Vettenburg, T. *et al.* (2014) 'Light-sheet microscopy using an Airy beam', *Nature Methods*, 11(5), pp. 541–544. Available at: https://doi.org/10.1038/nmeth.2922.

Vicidomini, G. *et al.* (2011) 'Sharper low-power STED nanoscopy by time gating', *Nature Methods*, 8(7), pp. 571–573. Available at: https://doi.org/10.1038/nmeth.1624.

Vladimirov, N., Voigt, F.F. and Campbell, R. (2023) *mesoSPIM-hardware-documentation*. Available at: https://github.com/mesoSPIM/mesoSPIM-hardware-documentation.

Vo-Dinh, T. (2014) *Biomedical Photonics Handbook Second Edition Therapeutics and Advanced Biophotonics Volume III*. Available at: https://doi.org/https://doi.org/10.1201/b17288.

Voie, A.H., Burns, D.H. and Spelman, F.A. (1993) 'Orthogonal-plane fluorescence optical sectioning: Three-dimensional imaging of macroscopic biological specimens', *Journal of*

Microscopy, 170(3), pp. 229–236. Available at: https://doi.org/10.1111/j.1365-2818.1993.tb03346.x.

Voigt, F.F. *et al.* (2020) 'Europe PMC Funders Group The mesoSPIM initiative – open-source light-sheet microscopes for imaging cleared tissue', 16(11), pp. 1105–1108. Available at: https://doi.org/10.1038/s41592-019-0554-0.The.

Wang, L., Jacques, S.L. and Zheng, L. (1995) 'MCML—Monte Carlo modeling of light transport in multi-layered tissues', *Computer Methods and Programs in Biomedicine*, 47(2), pp. 131–146. Available at: https://doi.org/10.1016/0169-2607(95)01640-F.

Wang, Y.Y.L. *et al.* (2023) 'Temperature-dependent effects of neonicotinoids on the embryonic development of zebrafish (Danio rerio)', *Frontiers in Marine Science*, 9. Available at: https://doi.org/10.3389/fmars.2022.1101737.

Waters, J.C. (2009) 'Accuracy and precision in quantitative fluorescence microscopy', *Journal of Cell Biology*, 185(7), pp. 1135–1148. Available at: https://doi.org/10.1083/jcb.200903097.

Weber, M. and Huisken, J. (2011) 'Light sheet microscopy for real-time developmental biology', *Current Opinion in Genetics and Development*, 21(5), pp. 566–572. Available at: https://doi.org/10.1016/j.gde.2011.09.009.

Weber, M., Mickoleit, M. and Huisken, J. (2014) 'Chapter 11 - Light sheet microscopy', in J.C. Waters and T. Wittman (eds) *Quantitative Imaging in Cell Biology*. Academic Press (Methods in Cell Biology), pp. 193–215. Available at: https://doi.org/https://doi.org/10.1016/B978-0-12-420138-5.00011-2.

Welch, A.J. and Van Gemert, M.J.C. (2011) 'Optical-thermal response of laser-irradiated tissue', *Optical-Thermal Response of Laser-Irradiated Tissue*, pp. 1–958. Available at: https://doi.org/10.1007/978-90-481-8831-4.

Westphal, V. *et al.* (2008) 'Video-rate far-field optical nanoscopy dissects synaptic vesicle movement.', *Science (New York, N.Y.)*, 320(5873), pp. 246–9. Available at: https://doi.org/10.1126/science.1154228.

Whitehead, L.W. *et al.* (2017) 'The reinvention of twentieth century microscopy for three-dimensional imaging', *Immunology and Cell Biology*, 95(6), pp. 520–524. Available at: https://doi.org/10.1038/icb.2017.36.

Willig, K.I. *et al.* (2007) 'STED microscopy with continuous wave beams', *Nature Methods*, 4(11), pp. 915–918. Available at: https://doi.org/10.1038/nmeth1108.

Wu, L. *et al.* (2022) 'Temperature dependent terahertz spectroscopy and imaging of orthotopic brain gliomas in mouse models', *Biomedical Optics Express*, 13(1), pp. 93–104. Available at: https://doi.org/10.1364/BOE.445597.

Wu, Y. *et al.* (2011) 'Inverted selective plane illumination microscopy (iSPIM) enables coupled cell identity lineaging and neurodevelopmental imaging in Caenorhabditis elegans', *Proceedings of the National Academy of Sciences of the United States of America*, 108(43), pp. 17708–17713. Available at: https://doi.org/10.1073/pnas.1108494108.

Wu, Y. *et al.* (2013) 'Spatially isotropic four-dimensional imaging with dual-view plane illumination microscopy', *Nature Biotechnology*, 31(11), pp. 1032–1038. Available at: https://doi.org/10.1038/nbt.2713.

Wu, Y. *et al.* (2016) 'Simultaneous multiview capture and fusion improves spatial resolution in wide-field and light-sheet microscopy', *Optica*, 3(8), p. 897. Available at:

https://doi.org/10.1364/optica.3.000897.

Yang, Z. *et al.* (2014) 'A compact Airy beam light sheet microscope with a tilted cylindrical lens', *Biomedical Optics Express*, 5(10), pp. 3434–3442. Available at: https://doi.org/10.1364/BOE.5.003434.

Yariv, A. and Albert, P.Y. (2003) *Optical waves in crystals : propagation and control of laser radiation (Book, 2003) [WorldCat.org]*. Hoboken (N. J.): J. Wiley & sons.

Yaroslavsky, A.N. *et al.* (2002) *Optical properties of selected native and coagulated human brain tissues in vitro in the visible and near infrared spectral range, Medicine and Biology Phys. Med. Biol*.

Yoon, Y. *et al.* (2019) 'System level analysis of motor-related neural activities in larval Drosophila', *Journal of Neurogenetics*, 33(3), pp. 179–189. Available at: https://doi.org/10.1080/01677063.2019.1605365.

York, A.G. *et al.* (2012) 'Resolution doubling in live, multicellular organisms via multifocal structured illumination microscopy', *Nature Methods*, 9(7), pp. 749–754. Available at: https://doi.org/10.1038/nmeth.2025.

Zagato, E. *et al.* (2017) 'Microfabricated devices for single objective single plane illumination microscopy (SoSPIM)', *Optics Express*, 25(3), pp. 1732–1745. Available at: https://doi.org/10.1364/OE.25.001732.

Zagato, E. *et al.* (2018) 'Technical implementations of light sheet microscopy', *Microscopy Research and Technique*, 81(9), pp. 941–958. Available at: https://doi.org/10.1002/jemt.22981.

Zarei, M. *et al.* (2022) 'High activity and high functional connectivity are mutually exclusive in resting state zebrafish and human brains’, *BMC Biology*, 20(1). Available at: https://doi.org/10.1186/s12915-022-01286-3.

Zhang, F. *et al.* (2015) ‘Optogenetics in freely moving mammals: Dopamine and reward’, *Cold Spring Harbor Protocols*, 2015(8), pp. 715–724. Available at: https://doi.org/10.1101/pdb.top086330.

Zhang, Q. and Kindt, K.S. (2022) ‘Using Light-Sheet Microscopy to Study Spontaneous Activity in the Developing Lateral-Line System’, *Frontiers in Cell and Developmental Biology*, 10. Available at: https://doi.org/10.3389/fcell.2022.819612.

Zhao, J. *et al.* (2021) ‘In vivo Imaging of Calcium Activities from Pancreatic beta-cells in Zebrafish Embryos Using Spinning-disc Confocal and Two-photon Light-sheet Microscopy’, *Bio-Protocol*, 11(23). Available at: https://doi.org/10.21769/BioProtoc.4245.

Appendices

Additional Figures

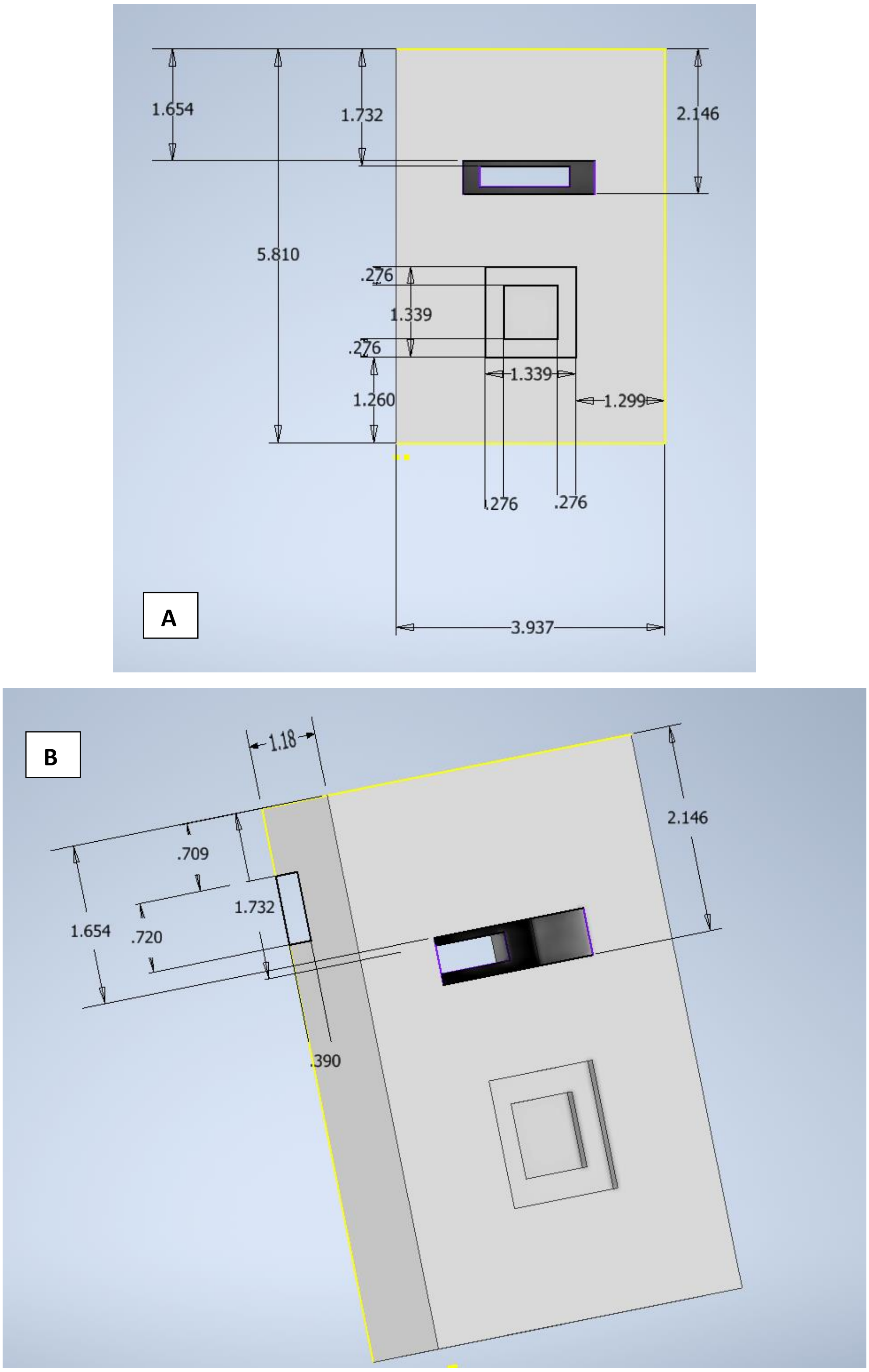

Figure A. 1: The top (A) and side (B) dimensions (inches) of metal slab made of aluminium

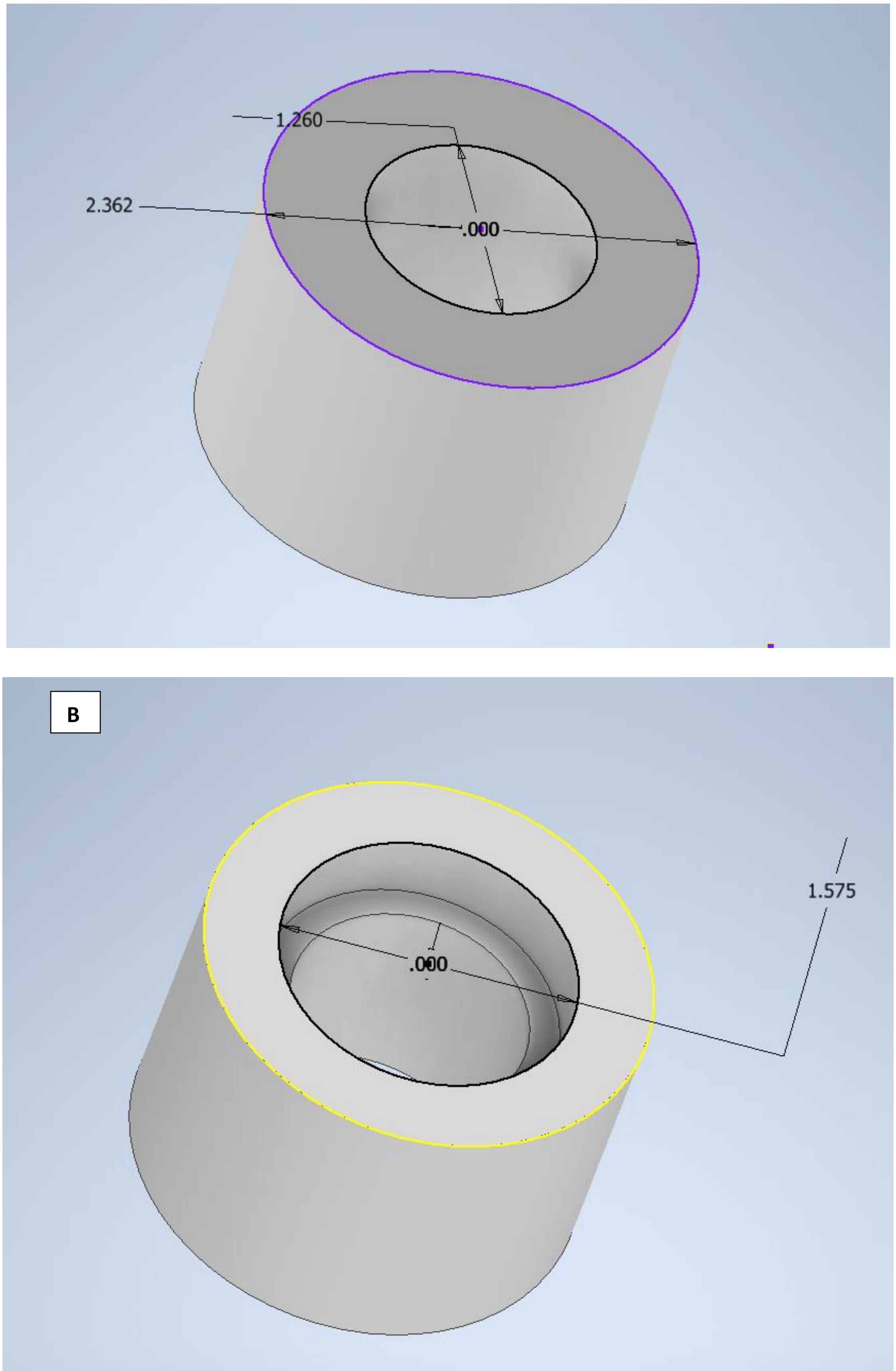

Figure A. 2: Front (A) and rear (B) dimensions (inches) of the SM1S10/U-TLU aluminium adapter.

Additional Tables

Table A. 1 – Table of Parts

ILLUMINATION AXIS				
Photonlines				
S/N	**Ref**	**Part**	**Quantity**	**Cost (EUR)**
1	LuxX 488-60	CW - diode laser	1	4995
2	LightHUB-4	Compact Laser Combiner without fibre coupler	1	4995
Thorlabs				
S/N	**Ref**	**Part**	**Quantity**	**Cost (EUR)**
1	RLA075/M	Dovetail Optical Rail, 75 mm, Metric	1	3025.57
2	RC1	RC1 - Dovetail Rail Carrier, 1" x 1"	4	
3	SD1	1/4" (M6) Counterbore Adapter Ring pack for RC1	1	
4	VA100/M	Adjustable Mechanical Slit Metric	1	
5	LMR05/M	Lens Mount with Retaining Ring for Ø1/2" Optics	6	
6	RSP1X15/M	Rotation Mount for Ø1" (Ø25.4 mm) Optics	1	
7	POLARIS-K1 - Polaris	Ø1" Mirror Mount, 3 Adjusters	1	
8	POLARIS-K1-H - Polaris	Ø1" Mirror Mount, 3 Low-Profile Hex Adjusters	2	
9	BB1-E02	Ø1" Broadband Dielectric Mirror, 400 - 750 nm	3	
10	AC127-050-A-ML	f=50 mm, Ø1/2" Achromatic Doublet, SM05-Threaded Mount, ARC: 400-700 nm	2	
11	AC127-025-A-ML	f=25 mm, Ø1/2" Achromatic Doublet, SM05-Threaded Mount, ARC: 400-700 nm	1	
12	ACY254-050-A	f = 50 mm, Ø1" Cylindrical Achromat, AR Coating: 350 - 700 nm	1	
13	CL3/M	Breadboard clamp	2	
14	CL2/M	Breadboard clamp	2	
15	HW-KIT1/M	M4 Cap Screw and Hardware Kit	1	
16	HW-KIT2/M	M6 Cap Screw and Hardware Kit	1	
17	SPW602	SM1 Spanner Wrench	1	

18	SPW606	SM1 Spanner Wrench	1	
19	DG05-1500-H1-MD	Ø1/2" SM05-Mounted Frosted Glass Alignment Disk	2	
20	MB7575/M	Optical bread board (M6 tapped 25 mm spacing)	1	
21	SH6MS12	M6 x 1.0 Stainless Steel Cap Screw, 12 mng, Pack of 25	1	
22	RLA300/M	Dovetail Optical Rail, 300 mm, Metric	1	
23	SH3M8	M3 X 0.5 Stainless Steel Socket Head Cap Screw Pack of (50)	1	
Physics Workshop - NUI, Galway				
S/N	**Ref**	**Part**	**Quantity**	**Cost (EUR)**
1	Lens Stilt	To mount the 1/2 inch lens for the beam expander 1, and the vertcal slit on the RC1. dimensions on OpenSPIM.org	2	N/A
2	Modified Corner Mirror stilt	Polaris-K1 RC1 mount - reduced height to 5.55mm height.	1	N/A
ALTERNATIVES/EXTENSIONS				
Thorlabs				
S/N	**Ref**	**Part**	**Quantity**	**Cost (EUR)**
1	N4X-PF	CFI 4x Plan Fluorite, 17.2 mm WD, 0.13NA	1	467.49
2	TR20/M-P5	Ø12.7 mm Optical Post, SS, M4 Setscrew, M6 Tap, L = 20 mm, 5 Pack	1	19.4
3	MC-5	25 Sheets per Booklet, 5 Booklets	1	10
4	CA4-EU	European Union Compliant Duster w/ Integrated Nozzle, 250 mL	1	21
5	MC10-M	Medium Powder-Free Nitrile Gloves, Qty. 100 Gloves	1	18.53
6	AC127-075-A-ML	f=75 mm, Ø1/2" Achromatic Doublet, SM05-Threaded Mount, ARC: 400-700 nm	1	76
7	ER8-P4	Cage Assembly Rod, 8" Long, Ø6 mm, 4 Pack	1	41
8	CP09/M	30 mm Removable Segment Cage Plate, 0.35" Thick, Metric	1	24
9	CP11/M	SM05-Threaded 30 mm Cage Plate, 0.35" Thick, Two Retaining	2	62

		Rings, M4 Tap		
10	PH20/M-P5	Ø12.7 mm Post Holder, Spring-Loaded Hex-Locking Thumbscrew, L=20 mm, 5 Pack	1	32
11	SM1A12	Adapter with External SM1 Threads and Internal M25 x 0.75 Threads	1	38
12	CP02B	30 mm Cage Mounting Bracket	2	104
13	SI050	Shearing interferometer with a Shear-Plate 2.5-5mm Beam	1	393.46
14	PSX501	Mini Light with Flexible Arm, Mounting Clip, and Magnetic Base	1	42.3
15	58-607	Edmond optics multi-Grid standard stage micrometer	1	340
Laser 2000 (UK) Ltd				
S/N	**Ref**	**Part**	**Quantity**	**Cost (EUR)**
1	F22.P1E01.1001	Laser safety glasses	1	224
Physics Workshop - NUI, Galway				
S/N	**Ref**	**Part**	**Quantity**	**Cost (EUR)**
1	Heat Sink	31 mm X 25 mm X 16 mm	1	N/A
DETECTION AXIS				
Photonlines				
S/N	**Ref**	**Part**	**Quantity**	**Cost (EUR)**
1	Pco Panda 4.2	Sensor customized scientific CMOS (sCMOS) camera	1	4995
Laser 2000 (UK) Ltd				
S/N	**Ref**	**Part**	**Quantity**	**Cost (EUR)**
1	BLP01-488R-25	~Ø1" 488 nm EdgeBasic best-value long-pass edge filter	1	660
2	FF03-525/50-25	~Ø1" 525/50 nm BrightLine single-band bandpass filter	1	
Masontec				
S/N	**Ref**	**Part**	**Quantity**	**Cost (EUR)**
1	U-TLU	Tube lens for detection objective	1	1670.34
2	U-TV1x	1x magnifying camera mount	1	
3	U-TV0.5XC-3	0.5x magnifying camera mount	1	
ALTERNATIVES/EXTENSIONS				

Thorlabs				
S/N	**Ref**	**Part**	**Quantity**	**Cost (EUR)**
1	SM1V15	Ø1" Adjustable Lens Tube, 1.31" Travel Range	1	32.5
2	SM1L05	SM1 Lens Tube, 0.50" Thread Depth, One Retaining Ring Included	1	11.44
3	SM1S10	SM1 Lens Tube Spacer, 1" Long	1	12
4	SM1A12	Adapter with External SM1 Threads and Internal M25 x 0.75 Threads	1	38
5	ER4-P4	Cage Assembly Rod, 4" Long, Ø6 mm, 4 Pack	1	25
6	CP02B	30 mm Cage Mounting Bracket	2	104
7	CP09/M	30 mm Removable Segment Cage Plate, 0.35" Thick, Metric	2	48
8	RC1	RC1 - Dovetail Rail Carrier, 1" x 1"	4	100
9	RLA150/M	Dovetail Optical Rail, 150 mm, Metric	2	41.56
ebay.com				
S/N	**Ref**	**Part**	**Quantity**	**Cost (EUR)**
1	Nikon MRD00105	CFI Plan Apo Lambda 10x, 0.45NA, 4 mm WD	1	350
Physics Workshop - NUI, Galway				
S/N	**Ref**	**Part**	**Quantity**	**Cost (EUR)**
1	Vertical Stilts	Cylinder shaped. M4 tap inner diameter. Outer diameter and height made to bring the centre of the mounted optics to 50 mm height above the breadboard	2	N/A
2	Detection axis holder	same design as on OpenSPIM. Modified to be mounted on two RC1 rail carriers	1	N/A
SHARED COMPONENTS ON BOTH AXES				
Thorlabs				
S/N	**Ref**	**Part**	**Quantity**	**Cost (EUR)**
1	RLA300/M	Dovetail Optical Rail, 300 mm, Metric	1	68
Piccard Industries				
S/N	**Ref**	**Part**	**Quantity**	**Cost (EUR)**

1	USB 4D Stage	USB 4D Stage	1	4882.26
PC Specialist (UK)				
S/N	**Ref**	**Part**	**Quantity**	**Cost (EUR)**
1	Acquisition and data processing computer	2 X Intel Xeon Gold 6230 20-Core (2.1GHz, 3.9GHz Turbo, 27.5M L3 Cache), 24GB NVIDIA TITAN RTX, 384GB Kingston DDR4 2666MHz, 1TB 2.5" SSD SATA 6 Gb, 16TB SEAGATE IRONWOLF PRO 3.5", windows 10 64bit, 2 x 10/100/1000 GIGABIT LAN PORTS	1	11275 * (potentially less than 6000 EUR)
ebay.ie				
S/N	**Ref**	**Part**	**Quantity**	**Cost (EUR)**
1	USB led lamp	for brightfield illumination of the sample during set-up	1	10
2	3.5 ml 10 mm Path JGS1 Quartz Cuvette Cell	12.5x12.5x45 mm, 10 mm path length, 3.5 ml volume, 200-2500 nm spectral range	1	26
Physics Workshop - NUI, Galway				
S/N	**Ref**	**Part**	**Quantity**	**Cost (EUR)**
1	Metal Slab	To elevate sample chamber/imaging cuvette to the required height		N/A
Total (VAT inclusive) =				**39,276.76**

*A PC less than 6000 EUR but with capable hardware may also suffice but will be more time consuming (Pitrone *et al.*, 2013d). Reconstruction can also be done on a high-performance computing (HPC) cluster at no financial cost where available. Jobs submitted to such facilities are usually queued, and to avoid queuing the same job repeatedly, there might be the need to run a down-sampled data on a local PC (with a decent hardware specification) to investigate optimal reconstruction parameters before submitting the job to the HPC cluster.

Table A. 2 – CPU and GPU hours for 3D reconstruction of two (2) views for 20 iterations

S/N	Sample	Step Size	Size per view	CPU Hours	GPU Hours
1	***Varroa destructor***	6 µm	2.8 GB	78	36